Electronic Structure and Prediction of Materials

UNIVERSITY OF LIVERPOOL

Thesis submitted in accordance with the requirements of
the University of Liverpool for the degree of
Doctor of Philosophy

by

Paul William Gardner

Surface Science Research Centre
Department of Chemistry
University of Liverpool

September 2011

Electronic Structure and Prediction of Materials

Paul William Gardner

Abstract

In this thesis the electronic structure and prediction of materials will be investigated. In the first two results chapters we will look at the use of Density Functional Theory primarily to investigate the Electronic Structure of materials, but also as a basic prediction tool.

Ruddelesden-Popper layered structures of the form $A_{n+1}B_nO_{3n+1}$ (A=Ca, B=Mn) are investigated with emphasis placed on the geometry and reasons behind the formation methods required. GGA and GGA+U functionals are used to describe the $n = 1 - 6$ and $n = \infty$ phases individually and to determine any trends in the size of the lattice, binding energies and geometries. There are energetic similarities as we increase n highlighting the need for alternative formation methods (Pulsed Laser Deposition) to conventional methods to prevent mixed phase structures as has been observed. The effect of doping or of restricting the size of a lattice with a substrate helps to reduce distortion in perovskite layers, enabling the formation of higher n-layered calcium manganese based Ruddlesden-Popper structures.

M(L-cysteinate) structures can be formed (M=Cd,Zn), which feature one-dimensional substructures that can be viewed as fragments of bulk structures of CdS (rocksalt high pressure phase) and ZnS (würtzite). Considering the structural similarities with bulk materials, the optical properties of M(L-cysteinate) were studied and indicate blue shifts of the band gap with respect to the bulk MS structures, due to the low dimensionality of the metal-sulphur arrangement. Density of states calculations show strong electronic structure similarities with the bulk phases and rationalize the band gap changes. A comparison of Hybrid (HSE03) functionals and DFT (GGA) is made when evaluating the density of states.

A Darwinian based evolutionary process called Genetic Algorithms is used to predict the ground state energy of clusters containing two model ion types of size N=4-20,30 with further insight for N=40,50. More primitive approaches to the selection and mating of clusters is used to simplify the GA process with successful comparison of results to previous work. A dependence on the number of clusters in the population evaluated is observed as we increase the number of ions in a cluster.

Acknowledgements

First and foremost I want to express my thanks to my superviser George. He has offered me great support and advice over the past four years and not just academically. I am truly grateful to have been able to do my PhD with him.

The community of the Surface Science Research Centre have not only provided great academic support and insight, but also an enjoyable experience during my time here. There are too many people to thank individually here from the SSRC, but below are people who deserve a special mention. To Arron, for helping show me the ropes at the start of my PhD and to his partner in crime, Mark, for making the Zoo even more enjoyable. With his great help over any problems with my calculations particularly with great insight and help with the Ruddlesden-Popper structures much thanks is due to Matthew Dyer. Finally, for all the long dinners and constant help with anything here at the University I want to thank Renee, Theresa, Natalia and Alejandro.

Outside of University my friends have always been there for me keeping my mind fresh to maintain a good work / life balance. I have been lucky to have friends like Mike, Andy, Danny and Simon. Also, having a friend like Mike Heaton to have someone to share the PhD process with and all its ups and downs was a great help. Over the last year particularly I owe a tonne of gratitude to Sam, Jay and Graham for the support they have given me and keeping me busy with 'Spirit Of Shankly'.

Last, but not least I want to thank my family. To my Mum and Dad, for always being there for me, always believing in me and never stopping pushing me to reach my full potential. My sister Nicola and her husband Andrew for their constant lifts to University amongst other things. Also, Doreen and Stephen have always been fantastic to me and their support over the past ten years has been invaluable.

Despite everything that has happened, I owe the biggest thanks to Cat. Giving me the best moments in my life and helping shape the person I am today.
"No matter the distance, I want you to know, that deep down inside of me..."

Paul,

September 2011.

Contents

List of Figures

List of Tables

List of Publications

Chiral II-VI Semiconductor Nanostructure Superlattices Based on an Amino Acid Ligand; Jean-Noël Rebilly, Paul W. Gardner, George R. Darling, John Bacsa, and Matthew J. Rosseinsky; Inorg. Chem. 2008, 47, 9390-9399

Chapter 1

Introduction

"One of the continuing scandals in the physical sciences is that it remains in general impossible to predict the structure of even the simplest cyrstalline solids from a knowledge of their chemical composition." John Maddox [1]

1.1 Search for New Materials

John Maddox in 1988 highlighted a problem that is still prevalent today. That of being able to predict the structure of a crystalline solid from first principles. It is this problem and the search for new materials that if solved can revolutionise materials science. Since 1988, advances have been made in pursuing different methods to be able to predict new structures, but the problem of computational limitations always exists restricting what is and is not possible at that time.

Maddox focuses on attempts to develop the ability to predict structures from knowledge of their chemical composition alone. With this proposition it brings into the debate what truly is prediction. What is the limit of information provided for the solution to still be classified as a forecast of what can be made rather than simply restricting anything else to be formed? In this sense of the problem as illustrated by an example used by Maddox of the work done by Tsuneyuki, Tsukada and Aoki, the tools of Molecular Dynamics and Density Functional Theory in their simplest forms, with input by experiment or chemical intuition, provide a more basic form of prediction. They allow us to address the properties and the

electronic structure of the specific crystalline geometry and stoichiometry helping us to influence experimental production or to verify it. However, we are restricted by the starting point of such calculations and ultimately will be unable to determine from one set of calculations alone if the output we witness is that of a true global minimum (GM) state. Depending on what we want to achieve with the structure determines on whether the GM state is actually the one we wish to find and develop.

1.1.1 Motivation

The primary focus of this thesis is to work on minimising the energy of a structure or cluster and using this information to gather more information about this structure. Although as mentioned above the solution we achieve when minimising the energy depends on our starting position and / or the computational method we are using.

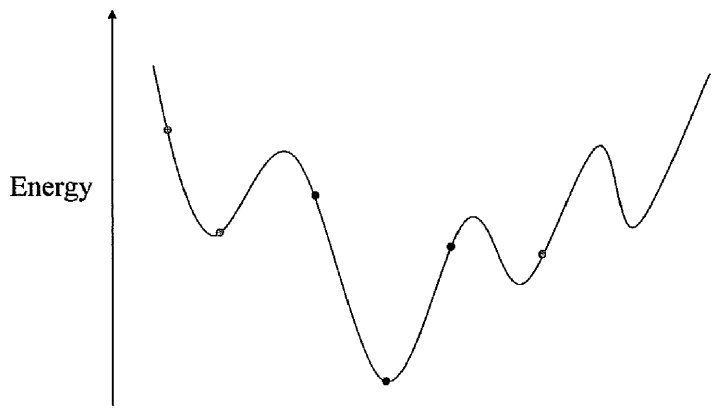

Figure 1.1: Potential Energy Surface

Figure 1.1 shows a schematic potential energy surface (PES) for a structure highlighting the existence of local and global minima. The blue dot indicates the GM and is usually deemed as the 'best' answer. Across the PES we have a number of basin of attractions that will determine the path to any solution we want to achieve. The orange dots lie in basins of attraction in proximity to a local mini-

mum whereas the black dots exist in the basin of attraction in proximity to the GM.

Essentially there are two types of minimiser, local and global. A local minimiser will find its best answer within their starting basin of attraction i.e. in figure 1.1 the orange dots would not find the 'best' structure, but the black dots would. A global minimiser helps find the GM structure regardless of the starting basin allowing potential barriers to be overcome. Local minimisers can be very useful in finding metastable states, but also GM states if we have experimental information such as the space group or lattice parameters, or we can use 'chemical intuition' to develop a starting point. A global minimiser helps to predict structures in it's truest form. The ultimate motivation would be to be able to predict the GM state free of any experimental data or 'chemical intuition'.

It is important in the pursuit of ground state energy states that we do not consider metastable states also. To be able to consider the effects of what is the GM state at a finite temperature and pressure. Also considering many other minima where multiple states co-exist together, to study phase transitions and any defects. After all, real materials are rarely single phase and defect free.

Any true *ab initio* approach should be free of prior knowledge and essentially the ultimate goal is to be able to predict new structures *ex nihilo*.

1.2 Review of Approaches

Here a review of approaches that have previously been studied is shown including approaches which require a knowledge input and others which attempt to achieve an *ex nihilo* approach.

1.2.1 Density Functional Theory and Molecular Dynamics

Density Functional Theory (DFT), Molecular Dynamics (MD) and other approaches such as Hartree-Fock theory will be addressed as one here since they are covered in more detail in chapter two. These methods are the most developed

approaches used and are primarily used to provide extra information on known structures. Although, with chemical intuition or a basic knowledge they can be used as a local minimiser to predict metastable states or potentially the GM state. However, whilst these approaches can create knowledge of the electronic properties on the output achieved they do not indicate as a sole calculation the nature of minima. The shortcomings of MD are that errors can be compounded and that is currently suitable for a short time span.

1.2.2 Simulated Annealing

Simulated Annealing (SA) is one of the oldest global optimisation methods and was described by Kirkpatrick, Gelatt and Vecchi [2]. It is based on the annealing process which is an experimental technique involving heating and controlled cooling of a material to increase the size of its crystals and reduce the number of defects. An initial temperature is chosen along with an initial structure. The structure is perturbed at each step of the SA algorithm with a Metropolis Monte Carlo algorithm also being used in evaluating the energy of the new structure and applying criteria to accept or reject this new structure. The Monte Carlo methods are a class of computational algorithms that rely on repeated random sampling to compute their results. The Metropolis algorithm follows the Monte Carlo method with adding a weighted average to the process [3]. The temperature is reduced according to a cooling schedule to a designated final temperature. In this process, the energy tends to go downhill, but it can go uphill if at a sufficiently high temperature therefore demonstrating the ability to escape a local minimum in pursuit of the GM. The success of this method is dependent on the cooling rate used, too fast and we may only find a local minimum, too slow and the algorithm becomes too computationally expensive to be deemed useful.

1.2.3 Basin Hopping

A method called Basin Hopping [4] was invented by Wales and was used to generate the Cambridge Cluster Database. It transforms the PES into a collection of intepenetrating 'staircases' where each plateau corresponds to a local minimum. The Monte Carlo method at a constant temperature is used with local

minimisation to be able to associate any point in configuration space with its local minimum. This uses geometry optimisation to start from a point in configuration space to find its associated local minimum. This transformation does not change the position of the GM or the relative energies of any local minima. The problem with this method is that if the wrong temperature is set we may miss the GM and the process is inefficient when returning to previously visited minima. The latter point can be addressed to some extent by manipulating the potential with a basin of attraction, however we need to know the basin boundaries to be able to do this. This method was used by Wales to determine the lowest known structures for all Lennard-Jones clusters up to 110 atoms.

1.2.4 MetaDynamics

Metadynamics attempts to build on Molecular Dynamics and Monte Carlo Simulation methods to be able to explore the properties of the free energy surface. The motivation behind this method by Laio and Parrinello [5] was to address the present-day computational limitations that reduce the scope of applications. During the simulation the location of the system in geometry space is determined and a positive Gaussian potential is added to the real energy landscape of the system. This effectively starts to fill in the basin of attraction the system currently sits in so that it will be discouraged from returning to the previous point. This process is repeated so that more and more Gaussian functions are added until the full energy landscape has been explored. At this point the energy landscape can be recovered. The opposite to the sum of the Gaussians will provide us with the free energy. The size of the Gaussian functions used and the time intervals at which they are added help shape the accuracy of the method and the computational time required. Problems can arise with a high dimensional PES and also if the dimensions of the Gaussian potential functions are not chosen adequately any transition basins between multiple minima could be flooded and subsequently making it impossible to pass through the new cumulative potential and cutting off part of the free energy surface. Laio and Parrinello demonstrated the usefulness of this approach in the case of the dissocation of a NaCl molecule in water.

1.2.5 Minima Hopping

Goedecker in 2004 [6] introduced the concept of Minima Hopping which is a non-thermodynamic approach seeking to replace the basin hopping method explained earlier. It is based on the principle of exploring the configurational space as fast as possible and reducing the rate of return to already visited minima. The algorithm uses Molecular Dynamics with local minimisation with an initial kinetic energy chosen. The MD algorithm is then run to quench towards a local minimum. If this minimum is new then it will be added to a history list and the kinetic energy will be reduced otherwise the kinetic energy will be increased. The MD algorithm is then performed again. The efficiency of the method depends strongly on the type of moves that are used to hop into new local minima. Moves that find low-barrier escape paths out of the present minimum generally lead into low energy minima. More recent work by Schönborn, Goedecker, Roy and Oganov [7], on test systems of Lennard-Jones, Silicon and Gold clusters, has sought to make improvements to this method enhancing the feedback given to the scaling and direction of the kinetic energy when a local minimum is found.

1.2.6 Random Structure Searches

Pickard and Needs introduced a random structure search method whilst evaluating high pressure phases of silane [8]. They do not use the previously used Monte Carlo or Molecular Dynamics here, but instead use first-principles electronic structure methods. A number of atoms is chosen and a random unit cell and position of atoms assigned. Local minimisation is performed and the entire process is repeated again to find more local minima. This is a very simple algorithm with minimal tuning parameters, but as expected for a large number of atoms the computational expense becomes very large and potentially inaccessible with present day technology.

1.2.7 Genetic Algorithms

The Genetic Algorithm (GA) approach is an evolutionary based algorithm to attempt to predict new structures and using a 'real-world' approach. The method

used in this thesis will be described further in chapter five develops more primitive operators to help towards generating a more efficient GA.

1.2.8 Future Possibilities

As illustrated above there are currently many different approaches, and it is too early to say if any approach is universally best. Some features are common to several methods, some are based on Molecular Dynamics or Monte Carlo methods, some use thermodynamics or some are unique like Genetic Algorithms. Some of the approaches like Simulated Annealing are largely superseded [9], but many approaches are being actively developed.

There may be another approach used in a different walk of life that may prove to be the best approach, or a combination of existing methods may prove fruitful, but it is important that studies are done to investigate the nature and success of tuning parameters and operators to help work towards developing an optimal method.

1.3 Outline of Thesis

Over the course of this thesis two of the above approaches have been employed. In chapter two we address the existing theory behind Molecular Dynamics, Density Functional Theory, Hartree-Fock Theory and Hybrid Functionals which will be used in the following chapters in helping provide extra information and verification to experimentally produced structures.

Chapter three looks at Ruddlesden-Popper type layered materials. Using DFT with GGA and GGA+U functionals to analyse the geometry of such structures, their energetics and to try and address the nature of formation as we increase the number of layers present.

Chiral II-VI semiconductor nanostructure superlattices based on an amino acid ligand are investigated in Chapter four namely for Cadmium and Zinc based structures. The nature and preference of the geometry of the L-cysteinate is compared to that of the relevant sulphide rock-salt and würtzite phases. Also,

the electronic structure, including properties such as the band gap, is studied and compared to experimental results.

The previous two results chapters use local minimisation based methods with the experimental knowledge to find the metastable state. Chapter five looks at the Genetic Algorithm approach with the application of new operators to attempt to predict the global minima for small ionic clusters.

The final chapter adds a brief conclusion commenting on future work and developments that could be pursued with respect to the previous chapters.

Chapter 2

Theory

2.1 Dynamical simulation and total energy computation

When investigating the properties of materials we need to evaluate the total energy of the system. The quantum mechanical behaviour of electrons in a solid needs to be understood and requires the calculation of the many-electron wavefunction for the system. The movement of electrons can be decoupled from the ions since the mass of ions is three to four orders of magnitude higher than the mass of electrons, it is therefore justified to neglect this term with only small changes in the total energy of the system [10], i.e. the difference in velocity allows the electron to 'see' the ionic cores as static (and so move in a static external field), and thus adjust the location instantaneously in reaction to a change in ion position [11]. This is known as the Born-Oppenheimer Approximation.

The many-electron wavefunction can be obtained in principle from the time-independent Schrödinger 2.1.

$$\varepsilon\psi(\mathbf{r_i}) = \left[\sum_i -\frac{\hbar^2}{2m}\nabla^2_{\mathbf{r_i}} + V_{ext}(\mathbf{R_i}) + V_{e-e}(\mathbf{r_i})\right]\psi(\mathbf{r_i}) \tag{2.1}$$

Where ε is the energy, $\mathbf{r_i}$ are the electronic coordinates, $\psi(\mathbf{r_i})$ the wavefunction, $V_{ext}(\mathbf{R_i})$ the external potential energy imposed by the nuclear configuration and $V_{e-e}(\mathbf{r_i})$ is the electron-electron interaction given by the Hartree term $\sum_{j>i}\frac{e^2}{|r_i-r_j|}$.

As written the potential is just Coulomb repulsion between electrons and Coulomb attraction between electrons and the nuclei.

However, the potential experienced by one electron, is influenced by the behaviour of all other electrons in the solid. The interaction between electrons is electrostatic in nature so is therefore dependent on the distance between the two electrons. This is all irrelevant though as to solve the Schrödinger equation directly would involve solving a system of 10^{23} simultaneous differential equations which is beyond the capabilities of present day computers, and is likely to remain so for the foreseeable future [12].

2.2 Hartree and Hartree-Fock Theory

Hartree was one of the first to try and solve the many-electron problem. A many-electron wavefunction was used and an assumption was made that this was simply the product of a set of single electron wavefunctions. Through the development of this method we obtain equations similar to the time-independent Schrödinger, however the potential (the Hartree potential) was no longer coupled to the individual motions of all the other electrons. This allows each electron to be treated as a single-particle obeying equation 2.2.

$$\varepsilon_i^\sigma \psi_i^\sigma(\mathbf{r}) = \left[-\frac{\hbar^2}{2m_e}\nabla^2 + V_{eff}^\sigma(\mathbf{r}) \right] \psi_i^\sigma(\mathbf{r}) \tag{2.2}$$

where $V_{eff}^\sigma(\mathbf{r})$ is an effective potential that acts on each electron of spin σ at point $\mathbf{r}$.

However, this approach does not match experimental evidence. The Hartree approach does not take into consideration the effect of the exchange interaction which is highlighted in the Pauli exclusion principle.

The Hartree-Fock theory tries to improve on the previous approach by introducing an exchange potential which takes into account the antisymmetric effects when exchanging two fermions (electrons) under the conditions of the Pauli exclusion principle. We can write the Hartree-Fock approximation equation in a

form analogous to the Hartree aproximation equation 2.2 except that the effective hamiltonian is an operator that depends upon the state.

$$\varepsilon_i^\sigma \psi_i^\sigma(\mathbf{r}) = \left[-\frac{\hbar^2}{2m_e}\nabla^2 + \hat{V}_{eff}^{i,\sigma}(\mathbf{r}) \right] \psi_i^\sigma(\mathbf{r}) \tag{2.3}$$

with

$$\hat{V}_{eff}^{i,\sigma}(\mathbf{r}) = V_{ext}(\mathbf{r}) + V_{Hartree}(r) + \hat{V}_x^{i,\sigma}(\mathbf{r}) \tag{2.4}$$

and the exchange term operator $\hat{V}_x$ is given by a sum over orbitals of the same spin σ

$$\hat{V}_x^{i,\sigma}(\mathbf{r}) = -\sum_{j \neq i} \int d\mathbf{r}' \psi_j^{\sigma *}(\mathbf{r}') \psi_i^\sigma(\mathbf{r}') \frac{1}{|\mathbf{r} - \mathbf{r}'|} \frac{\psi_j^\sigma(\mathbf{r})}{\psi_i^\sigma(\mathbf{r})} \tag{2.5}$$

However, another problem was discovered. As with the Hartree approach the potential did not include a correlation term. Neither method solved the many-body problem of electrons but identified key concepts (exchange and correlation terms). This allowed the framework for the breakthrough of Density Functional Theory in 1964.

2.3 Density Functional Theory

Density Functional Theory (DFT) as formalised by Hohenberg and Kohn in 1964 [13] took a different approach. DFT bases the system representation around the electronic distribution (or charge density), hence the system is reduced to three spatial dimensions irrespective of N [11]. It provided an exact theory for interacting electrons [13] and a practical method for calculating in terms of single electron equations [14]. The importance of this work was shown by the award of the Nobel prize for chemistry to Walter Kohn in 1998 [15]. Density functional theory is based upon two theorems established by Hohenberg and Kohn [16]:

- **Theorem I:** For any system of interacting particles in an external potential $V_{ext}(\mathbf{r})$, the potential $V_{ext}(\mathbf{r})$ is determined uniquely, except for a constant, by the ground state particle density $n_0(\mathbf{r})$.
- **Theorem II:** The universal functional E[n] in terms of the density $n(\mathbf{r})$ can be defined, valid for any external potential $V_{ext}(\mathbf{r})$. For any particular $V_{ext}(\mathbf{r})$, the exact ground state energy of the system is the global minimum value of this functional, and the density $n(\mathbf{r})$ that minimises the functional is the exact ground state density $n_0(\mathbf{r})$.

Since the energy is a functional of this potential we can write the first principle as : *The total energy of a system of electrons and nuclei is a unique functional of the electron density* [17].

DFT despite remaining completely general it is a simple theory. The energy can be written as:

$$E = E[\rho(r)] = \int dr(V_{ext}(\mathbf{r})\rho(\mathbf{r})) + F[\rho(\mathbf{r})] \tag{2.6}$$

where $\rho(\mathbf{r})$ is the electron density.

Both right hand terms in equation 2.6 are functionals. This is a key point in the Hohenberg-Kohn Theorems as they do not tell you how to compute anything. Kohn and Sham tried to address this by representing the second term as an amended term $F[\rho(\mathbf{r})]$ which is a summation of the interactive potential components within the electron gas:

$$F[\rho(\mathbf{r})] = E_K[\rho(\mathbf{r})] + E_H[\rho(\mathbf{r})] + E_{xc}[\rho(\mathbf{r})] \tag{2.7}$$

where, E_H is the Hartree Coulomb term, E_K is the electron kinetic energy and is defined as the kinetic energy of a system of non-interacting electrons which give rise to the electron density $\rho(\mathbf{r})$, and E_{xc} is the exchange-correlation function. E_{xc} is the correction to the Hartree theory (see section 2.2) and therefore is not included in the other two terms and allows the functional $F[\rho(\mathbf{r})]$ to be exact, but at the price that E_{xc} is not explicitly known. We need to attempt to solve the Kohn-Sham equations for DFT to work.

2.3.1 Exchange Correlation (XC) Functionals

Since the exact form of the exchange-correlation term is not explicitly known, there have been various XC Functionals developed to try and address this problem and consequently improve the accuracy of electronic structure calculations.

Local Density Approximation (LDA)

Early calculations employed the local density approximation (LDA) [14; 18; 19]. In the LDA we assume the exchange and correlation potentials depend on the value of the charge density at a specific point of the system [10]. The exchange and correlation at that point is then replaced by the exchange and correlation calculated for a homogeneous electron gas. We can express the exchange-correlation energy for spin-unpolarised systems as

$$E_{xc}^{LDA}[\rho(\mathbf{r})] = \int d\mathbf{r}\rho(\mathbf{r})\epsilon_{xc}(\rho(\mathbf{r})) \tag{2.8}$$

Where ρ is the electron denstiy and ϵ_{xc} is the exchange correlation density for a homogeneous electron gas of density $\rho(r)$.

The total XC-Energy can be split into the exchange and correlation components:

$$E_{xc} = E_x + E_c \tag{2.9}$$

The LDA exchange energy is given by:

$$E_x^{LDA} = -\frac{3}{4}\left(\frac{3}{\pi}\right)^{\frac{1}{3}} \int \rho(\mathbf{r})^{\frac{4}{3}} d\mathbf{r} \tag{2.10}$$

and the LDA correlation energy is given by:

$$E_c^{LDA} = \int d\mathbf{r}\rho(\mathbf{r})\epsilon_c(r_s(\mathbf{r})) \tag{2.11}$$

Where $\epsilon_c(r_s)$ is the correlation energy per electron of the homogeneous gas and r_s is the Wigner-Seitz radius which is related to the density as:

$$\frac{4}{3}\pi r_s^3 = \frac{1}{\rho} \tag{2.12}$$

$\epsilon_c(r_s)$ cannot be determined analytically except for high and low density limits therefore interpolation functions are used.

Local Spin Density Approximation (LSDA)

The LSDA follows the same idea as the LDA, but is based on a spin-polarised electron gas. The LSDA is of the form

$$E_{xc}^{LSDA} = \int d\mathbf{r}((n_\uparrow(\mathbf{r}) + n_\downarrow(\mathbf{r}))\epsilon_{xc}(n_\uparrow(\mathbf{r}), n_\downarrow(\mathbf{r})) \tag{2.13}$$

The XC-energy of the spin-polarised electron gas was obtained by introducing spin-polarisation by an external magnetic field.

Generalised Gradient Approximation (GGA)

The generalised gradient approximation (GGA) [20; 21] extends the LDA by smoothing the E_{xc} spatially by considering the variation of ρ with r. By including information on the spatial variation in the electron density it can create a functional with greater flexibility to describe real materials. The GGA functional takes into account not only the electron density, but also as the name suggests the gradient of the electron density, i.e.

$$E_{xc}^{GGA} = E_{xc}^{GGA}[\rho(\mathbf{r}), \nabla\rho(\mathbf{r})] \tag{2.14}$$

GGA functionals are used in chapters three and four whilst investigating the material properties and geometries of Ruddlesden-Popper layered materials and Chiral II-VI semiconductor nanostructure superlattices based on an amino acid ligand. There are many flavours of GGA including Perdew-Wang 91 (PW91) [22] and Perdew-Burke-Ernzerhofer (PBE) [23]. GGA still accounts for the bulk of today's simulations.

LDA+U

In the Hartree-Fock method the self interaction in the Hartree potential (equation 2.5) is exactly cancelled out by the contributions to the energy from exchange. Self interaction arises because the electron we are describing in the Kohn-Sham equation is also part of the total electron density so part of the Hartree potential involves a Coulomb interaction between the electron and itself. If the exact Kohn-Sham functionals were known this could also be said of DFT. In any approximate DFT functional a systematic error arises due to the incomplete cancellation of the self-interaction energy. The self interaction error causes the Kohn-Sham orbitals that are highly localised to be improperly destabilised with approximate exchange-correlation functionals. Unpaired electrons tend to delocalise spatially in order to minimise self-interaction. When electronic states with many strongly localised electrons exist, these states are said to be strongly correlated. Examples of such materials include actinides and transition metal oxides.

Since the self-interaction errors are cancelled exactly in the Hartree-Fock calculations, it suggests that a HF type approach for the localised states, with DFT for all other states may be a possible approach for strongly correlated systems. This provided the motivation for the LDA+U method [24]. This method introduces a correction for the self-interaction energy [19] found when using LDA or GGA by introducing a single numerical parameter, $U - J$ where U and J involve different aspects of the self-interaction and are derived from the Hubbard Model to better represent highly localised states [25].

The LDA+U approach obviously requires the U and J parameters to be specified. This can be determined by using another kind of *ab intio* calculation in which the calculations are feasible to estimate $U - J$ or to take a known property of a material and determine which value of $U - J$ gives the closest result to this property for a given functional. The accuracy of this method therefore correlates with the accuracy at which the $U - J$ parameters are used. The LDA+U method, or namely that of GGA+U is used in chapter three in investigating Ruddlesden-Popper layered materials along with GGA functionals.

2.3.2 Hybrid Functionals

DFT is known to underestimate band gaps with errors larger than 1eV being common when comparing with experimental data [26] and hence another suitable method was sought to provide a more accurate answer. Hybrid Hartree-Fock plus Density Functional Theory functionals partially correct the self-interaction error because of their partial use of the exact exchange energy. These functionals add a contribution of Fock exchange to the standard DFT and have been demonstrated to yield improved band-gaps compared to standard DFT and Hartree-Fock [27–29]. Specifically, comparisons between PBE (Perdew-Burke-Ernzerhof) and the hybrid PBE0, B3LYP (Becke, three-parameter, Lee-Yang-Parr) and HSE03 (Heyd, Scuseria, Ernzerhof), showed that PBE0 and HSE03 provide an improved description of the band gaps compared to conventional DFT. HSE03 and PBE0 [28; 30] are implemented in the most recent version of VASP (v5).

Hybrid functionals take the form of:

$$E_{xc} = (1-a)E_{xc}^{DFT} + aE_x^{HF} \tag{2.15}$$

The evaluation of the E_x^{HF} can be very computationally demanding and varies with the decay of the Hartree-Fock exchange interactions with distance. This decay is highly system dependent and can range from a few up to hundreds of Ångstroms. Heyd *et al* [31; 32] proposed to replace the long range part of the Hartree-Fock exchange in the PBE0 Hybrid functional by a corresponding density functional counterpart to avoid the calculation of expensive integrals over slowly decaying exchange interactions. The expression given for the XC-energy (HSE03) is

$$E_{xc}^{HSE} = aE_x^{HF,sr,\mu} + (1-a)E_x^{PBE,sr,\mu} + E_x^{PBE,lr,\mu} + E_c^{PBE} \tag{2.16}$$

where $a = 1/4$ is the HF mixing constant, (sr) and (lr) denote the short and long range parts of the respective exchange interactions. This separation into short and long range parts is accomplished through a decomposition of the Coulomb kernel

$$\frac{1}{r} = S_\mu(r) + L_\mu(r) = \frac{\mathrm{erfc}(\mu r)}{r} + \frac{\mathrm{erf}(\mu r)}{r} \tag{2.17}$$

where $r = |\mathbf{r} - \mathbf{r}'|$; and μ is the parameter that defines the range separation with a typical value of μ=0.4bohr^{-1}.

These functionals are too computationally expensive to be used in standard electronic structure geometry optimization calculations on large systems. When used in the studies in this Thesis to obtain more reasonable estimates of the band gaps, we have used the standard DFT for geometry optimisation, subsequently running VASP v5 [33–36] to obtain the self-consistent electronic structure with the HSE03 functional.

2.3.3 Self consistency

In any numerical implementation a many electron problem has to be solved iteratively. The reason is the inherent non-linearity of the fundamental Kohn-Sham equations. Using an existing density distribution the Kohn-Sham eigenvalues and eigenvectors can be calculated in a single step. However, the summation of the charge density over all eigenstates creates a new potential which in turn gives new eigenvalues and eigenvectors. Hence, the final result cannot be determined from one iteration only.

Below is a rough structure of an electronic self consistent iteration cycle [10]:

1. Initially we need to obtain an effective potential in the single electron Kohn-Sham equations. We can obtain the various components of the potential from the existing distribution of ions and electron density ρ_0: the external potential V_{ext} (summation over ions), the Hartree potential V_H (solving the Poisson equation for the charge distribution), and the exchange-correlation potential V_{xc}. The effective potential is then:

$$v_{eff}(\mathbf{r}) = V_{ext}(\mathbf{r}) + V_H(\mathbf{r}) + V_{xc}(\mathbf{r}) \tag{2.18}$$

2. Solve the corresponding Kohn-Sham equation with $\phi_{KS}(\mathbf{r})$ being the wavefunction:

$$\left(\frac{\hbar^2}{2m}\nabla^2 + v_{eff}(\mathbf{r})\right)\phi_{KS}(\mathbf{r}) = \epsilon_{KS}\phi_{KS}(\mathbf{r}) \tag{2.19}$$

3. Calculate the total energy from the various contributions. The total energy in a system is described by a sum over the eigenvalues of occupied states and some corrections:

$$E_{KS,Step} = \sum_{i}^{occ} \epsilon_{KS,i} - E_H[\rho] + E_{xc}[\rho] - \int V_{xc}(\mathbf{r})\rho(\mathbf{r})d\mathbf{r} \tag{2.20}$$

4. See if this energy is equal to the previous one. If yes, stop the iteration.

$$\text{If} \quad E_{KS,Step} - E_{KS,Step-1} < \delta E \Rightarrow \quad Stop \tag{2.21}$$

Here, δE is a small energy value, usually around 10^{-4}meV.

5. If the condition in equation 2.21 is not met, the density contributions from the occupied states are then summed to create a charge density:

$$\rho_{new}(\mathbf{r}) = \sum_{i}^{occ} |\phi_{KS,i}(\mathbf{r})|^2 \tag{2.22}$$

6. To maintain numerical stability of the simulation a procedure called mixing is used. There are several forms of this process, but it involves mixing part of the new charge density obtained in equation 2.22 with the old charge density ρ_0 to obtain a new charge density ρ_1. $\mathcal{M}$ is the mixing functional:

$$\rho(\mathbf{r}) = \mathcal{M}[\rho_0(\mathbf{r}), \rho_{new}(\mathbf{r})] \tag{2.23}$$

7. With the new density ρ_1 the cycle starts again from step 1.

This self consistent cycle allows the groundstate positions of all ions to be obtained. The forces on the ions can then be calculated, and consequently the ions can then be moved according to the forces acting on them. Depending on the system (number of elements, type of elements i.e. number of electrons), electronic self consistency in today's codes takes about 10-50 iterations and for the first step can be much more. However, if ionic relaxation was required this could increase the

timescale to a few hundred cycles depending on the accuracy of the initial guess of the system.

2.4 Plane Wave Basis Sets

In Density Functional Theory we have to look for solutions to the time independent Schrödinger equation (equation 2.1) to look at solving for the simplified many-body problem of non-interacting electrons experiencing an effective potential $V(\mathbf{r})$.

For periodic systems the potential has the property

$$V(\mathbf{r}+\mathbf{R}) = V(\mathbf{r}) \tag{2.24}$$

where $\mathbf{R}$ is a lattice vector $\mathbf{R} = n_1R_1 + n_2R_2 + n_3R_3$ for any integers n_1, n_2 and n_3; with R_1, R_2 and R_3 being the three unit cell vectors of the system.

If we solve the Schrödinger equation for this periodic system, the solution must satisfy a fundamental property known as Bloch's theorem, which states that a solution can be expressed as a sum of terms with the form

$$\psi_{\mathbf{k}}(\mathbf{r}) = \exp(i\mathbf{k}\cdot\mathbf{r})u_{\mathbf{k}}(\mathbf{r}) \tag{2.25}$$

from which it follows similarly to equation 2.24

$$u_{\mathbf{k}}(\mathbf{r}+\mathbf{R}) = u_{\mathbf{k}}(\mathbf{r}) \tag{2.26}$$

The first term of equation 2.25 is the wavelike part. The second term is the cell periodic part of the wavefunction. This can be expressed by expanding it into a finite number of plane waves whose wave vectors are reciprocal lattice vectors of the crystal.

$$u_{\mathbf{k}}(\mathbf{r}) = \sum_{\mathbf{G}} c_{i,\mathbf{G}}\exp(i\mathbf{G}\cdot\mathbf{r}) \tag{2.27}$$

where $\mathbf{G}$ are the reciprocal lattice vectors which are defined by $\mathbf{G} \cdot \mathbf{R} = 2\pi m$ for all $\mathbf{R}$ where m is an integer. Therefore each electronic wavefunction is written as a sum of plane waves

$$u_{\mathbf{k}}(\mathbf{r}) = \sum_{\mathbf{G}} c_{i,\mathbf{k}+\mathbf{G}} \exp(i(\mathbf{k}+\mathbf{G}) \cdot \mathbf{r}) \tag{2.28}$$

In an infinite system there is an infinite number of $\mathbf{k}$ vectors at each of which solutions for $\psi_{\mathbf{k}}$ exist since the number of electrons is infinite. This can be simplified taking into account that the change in $\psi_{\mathbf{k}}$ with $\mathbf{k}$ becomes negligible for $\mathbf{k}$-points that are close together. Therefore we can calculate at a finite number of $\mathbf{k}$-points. We refer to this as $\mathbf{k}$-point sampling. Although, the set of vectors $\mathbf{G}$ should in principle be infinite, summing over a finite number will yield sufficient accuracy.

A plane-wave basis set has many advantages [17]:

- It is unbiased, so all space is treated the same.
- It is complete.
- In principle, there is a single convergence criterion.
- Plane waves are mathematically simple and their derivatives are products in k-space.
- Plane waves do not depend on atomic positions.

and two important disadvantages:

- The number of plane waves needed is determined by the greatest curvature of the wavefunction.
- Empty space has the same quality of representation and cost as regions of interest.

From the advantages we can see that the adequacy of a calculation is determined by the number of plane waves used. Therefore the quality of the basis set depends on a single parameter, which is usually expressed as the energy of a free electron whose wavefunction has the same wavevector as the largest wavevector in the plane-wave basis

$$E_c = \frac{\hbar^2(\mathbf{G}+\mathbf{k})^2}{2m} \tag{2.29}$$

Using the cut-off energy E_c will mean that all plane waves of energy less than E_c will be used in the expansion.

The convergence is also controlled by the number of k-points included in the calculations. In practice only a few k-points of the first Brillouin zone are included. The actual number required for convergence of the total energy depends on both the size and the type of the system under study. Several methods exist for generating the k-points in the first Brillouin zone, with the most common one being the Monkhorst-Pack scheme [37].

2.4.1 Pseudo-potentials

A problem with plane wave methods is that a good description of the atomic character close to the nuclei requires an enormous amount of plane waves. The motivation of so-called pseudo-potentials is to project out the core wave functions, which hardly overlap and which should not strongly affect the valence electrons and that the potential acting on the valence electrons should be smooth and therefore require a much smaller cut-off.

This is possible because the band structure is mainly determined by the scattering properties of each atom. In particular, the scattering phase shift, which is determined by the value and the slope of the wave function at the radius where the scattering potential vanishes. Therefore it should be possible to find different potentials, which give rise to the same phase shift.

There are two aspects to consider which need balancing:

- Transferability - The pseudo-potentials should be independent of their environment. This requires a small cut-off radius.
- Softness - The pseudo-potentials should lead to fast converging plane wave expansions. This requires a large cut-off radius.

Several different pseudo-potentials exist, for example orthogonalised plane wave (OPW), norm-conserving pseudopotentials (NCPP), ultra-soft pseudopotentials

(USPP) and the projector augmented waves (PAW) method.

It is also worth noting that pseudo-potentials are not just bound to plane wave methods and can be used with many other computational techniques, such as real-space grid methods or local-orbital type methods.

Ultra-soft pseudo-potentials (USPP)

Pseudo-potential based methods are increasingly used to calculate very large systems consisting of a large number of atoms. In such large calculations, the number of plane waves is often the limiting factor. When this is the case, it can actually be cheaper to relax the norm-conservation condition and sacrifice on the transferability in order to construct softer pseudo-potentials which are as smooth as possible. A pseudo-potential is said to be norm-conserving if outside the core the real and pseudo wavefunctions generate the same charge density. Correction terms for the charge potential need to be included along with constructing the pseudo-potentials for the given environment. These extra costs are compensated by the fast convergence of the actual calculation.

Projector Augmented Waves (PAW)

One of the more accurate pseudo-potentials is the projector augmented (PAW) method. It is related to USPP, but in PAW an exact transformation between the all electron and the pseudo wave function is introduced. By doing this all core wavefunctions, calculated inside the cut-off radius, are kept exact allowing the all electron density and other quantities to be recovered if needed. All integrations are split into integrations of the smooth functions in the whole space plus integrations over the rapidly varying functions inside the spheres around the atoms.

2.5 Density of States (DOS)

The density of states (DOS) gives the number of states, n(E), in a small energy interval, dE:

$$dN = n(E)dE \tag{2.30}$$

This can be expressed as a surface integral over constant energy surfaces:

$$n(E) = \frac{2}{(2\pi)^3} \int_{E(k)=const} \frac{dS_E}{\nabla_k E(\mathbf{k})} \tag{2.31}$$

assuming here that this is a non-magnetic system, where two spin channels simply give rise to a factor of 2.

The flat regions of the bands can give rise to the so called van Hove singularities. A more appropriate form of this expression for calculations is:

$$n(E) = \frac{2}{N_k} \sum_{nk} \delta(E - \epsilon_{nk}) \tag{2.32}$$

N_k is the number of k-points in the Brillouin zone with a sum over n dimensions at an arbitrary k, with respect to k.

It can be useful to know which atom is contributing the states and which angular momentum character they have. This can be done with the projected DOS. If we have some local basis $\phi(\mathbf{r})$, we can expand the Bloch wave function in this basis and obtain for the expansion coeficients

$$c^i_{nk} = \langle \phi | \Psi_{nk} \rangle \tag{2.33}$$

The projected DOS is then defined as

$$n_i(E) = \frac{2}{N_k} \sum_{nk} |c^i_{nk}|^2 \delta(E - \epsilon_{nk}) \tag{2.34}$$

2.6 Molecular Dynamics

MD calculations are able to predict equilibrium and non-equilibrium properties of condensed systems. The approach that is taken is usually used for systems such as rare gases as they use empirical interatomic potentials so do not usually

give the required results for covalent and/or metallic systems, and with empirical model force fields. Also, classical MD calculations do not provide us with any information about the electronic properties of the system. We can use MD with DFT, but this is very computationally expensive.

For classical objects we can use Newton's Equations of motion. For example, we can treat a set of nuclei as classical masses with an interaction energy $\mathrm{E}[\{\mathbf{R}_I\}]$ dependent on the positions of the particles $\{\mathbf{R}_I\}$ and can obtain the equations of motion as

$$M_I\ddot{\mathbf{R}}_I = -\frac{\partial E}{\partial \mathbf{R}_I} = \mathbf{F}_I[\{\mathbf{R}_J\}] \tag{2.35}$$

In simple cases these equations can be solved analytically. However, in general the solution is done by numerical simulations using discrete time steps based upon discrete equations such as the Verlet Algorithm [38]. At each time step t the position of each nucleus is advanced to the next time step $t + \Delta t$ depending upon the forces due to the other nuclei at the present time step.

$$\mathbf{R}_I(t + \Delta t) = 2\mathbf{R}_I(t) + \mathbf{R}_I(t - \Delta t) + \frac{(\Delta t)^2}{M_I}\mathbf{F}_I[\{\mathbf{R}_J(t)\}] \tag{2.36}$$

where the first two terms are just the law of inertia. The key property of the Verlet Algorithm is its stability as the errors do not accumulate despite the equations only being approximate for any finite Δt.

When evaluating the forces we have to take into account the forces on the nuclei that are determined by the electrons along with the direct force between the nuclei. Effective potentials have been used in the past to incorporate the effects of the electrons e.g. using the Lennard-Jones potential. In this thesis, MD is used in a simplified Genetic Algorithm approach to materials design in chapter five.

2.7 Software and Hardware

A variety of computational facilities have been used during the duration of my PhD. It is unnecessary to cite every application used, so only the more frequently employed and specialised resources are referenced in this section.

Intensive DFT calculations have been implemented using the VASP v4 and v5 [33–36] DFT programme using a facility of a cluster of 58 dual processor, dual core nodes (140 cores),each with 2.4GHz, 8GB RAM and 50 dual-processor, quad core nodes (400 cores) 2.3GH 32GB RAM; another cluster of 44 dual processor, dual core nodes (176 cores), 2.2GHz, 8GB RAM and 23 dual processor quad core nodes (184 cores), 2.3GHz, 32GB RAM and 37 dual processor quad core nodes (296 cores), 2.3GHz, 16GB RAM; and another cluster of 39 nodes where each node has a 3.06 GHz Intel Xeon processor and 1Gb of memory. The creation and alterations of the structures required is performed through the use of the Cerius 2 [39] front end visualisation programme, while post-calculation analysis and image creation are carried out with the chemistry orientated viewer jmol [40] v11 and v12. Also, Microsoft Excel v11 enabled basic numerical and visual analysis of programme output.

VASP

The Vienna Ab-initio Simulation Package, or VASP [33–36] as it is better known, is a package for performing DFT calculations by solving the Kohn-Sham Hamiltonian with a plane wave basis set and ultra-soft Vanderbilt or PAW pseudopotentials. VASP is a Fortran 90 program that was developed during the 1990's and was based on CASTEP (Cambridge Ab-initio Sequential Total Energy Package). The approach implemented in VASP is based on the finite temperature local density approximation with the free energy as a variational quantity and an exact evaluation of the instantaneous electronic ground state at each geometry optimisation [33].

Chapter 3

Ruddlesden-Popper Layered Materials

3.1 Introduction

Transition metal oxides, in particular perovskite type structures like the Ruddlesden-Popper (RP) phases, exhibit a rich variety of electronic properties such as insulator-metal transitions, superconductivity and charge ordering [41]. Manganese oxides and particularly those with the pervoskite structures have received much attention with members of the manganese oxide Pervoskite Family displaying colossal magnetoresistance (CMR) [42–46].

RP compounds can be represented with the general formula $A_{n+1}B_nO_{3n+1}$, where A and B are elements to be allocated and O is oxygen. They are perovskite-like layered materials whose form can be better visualised by use of the general formula $AO(ABO_3)_n$. As demonstrated by Figure 3.2 (using the specific elements in this investigation, A=Ca, B=Mn there are alternating blocks of n layers of a rock salt and a perovskite structure. Figure 3.1 shows the ABO_3 perovskite structure which consists of BO_6 octahedra. This structure can also be described as the $n = \infty$ RP structure. Note also the O atom labels in figure 3.1 which will be used later for the description of the results.

RP phases can be considered to consist of perovskite blocks of vertex sharing BO_6 octahedra which extend to infinity in the ab plane have a thickness of n in

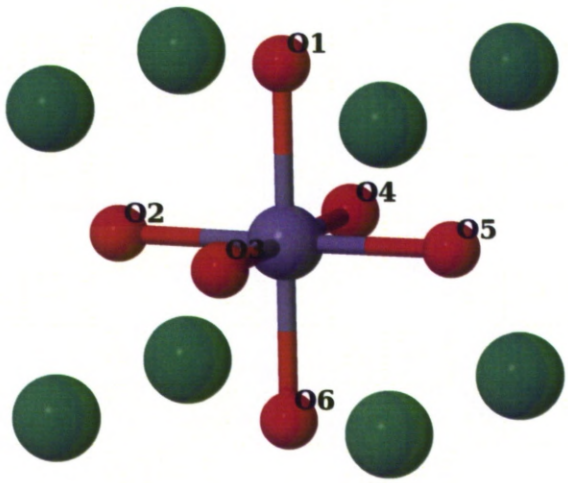

Figure 3.1: Perovskite Structure. Green: A; Purple: B; Red: O

octahedra parallel to the c axis; neighbouring blocks are separated by a rock salt layer such that the overall composition can be described as above [47].

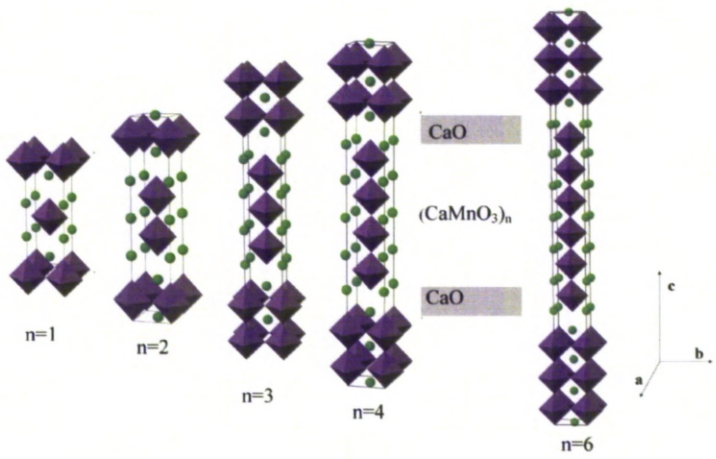

Figure 3.2: The Ruddlesden-Popper $A_{n+1}B_nO_{3n+1}$ series can be viewed as the assembly of AO rock salt and ABO_3 layers.Here the unit cells of the $n = 1 - 6$ members of the $CaO/(CaMnO_3)_n$ RP family are shown. Purple: MnO_6 polyhedra; Green: Ca

3.1.1 Formation

Conventional solid state synthesis methods can be used to obtain complex extended structures which can be classified in terms of structural units. These methods involving a diffusional reaction between powders ground to dimensions in the order of microns often require elevated temperatures in order to permit diffusion of the reacting atoms at a sufficient rate to form the desired structure. This route is used in the production of the RP compound $CaO(CaMnO_3)_n$ with values of n ranging from one to three layers. With the exception of thermodynamically controlled routes such as intercalation into a pre-existing host, this usually leads to the formation of thermodynamically controlled products. In this case the absence of a direct structural relationship between reagents and products hinders the targeted synthesis approach [48]. Other experimental procedures needed to be used to obtain higher values of n: kinetically controlled approaches to materials assembly, involving the pre-assembly of disordered reagents to direct low temperature crystallisation or the atom by atom construction of materials by molecular beam epitaxy (MBE) approach for example. The related process of pulsed laser deposition (PLD) can be exploited to prepare new multilayered materials and is used in the construction of the $n = 4$, 5 and 6 members of the $Ca_{n+1}Mn_nO_{3n+1}$ RP series by assembly of the constituent modules ($CaMnO_3$ perovskite and CaO rock salt blocks) in a unit cell upon unit cell manner on a STO substrate with $in - situ$ monitoring of the growth process using reflection high-energy electron diffraction (RHEED) [48].

3.1.2 Motivation

There have been previous studies, both theory and experimental, of the electronic and magnetic properties of Ruddlesden-Popper manganites for n up to three and $n = \infty$ structures [49–51]. This has shown properties such as antiferromagnetic ordering in a Calcium Managanate RP Structure. However, the motivation for the calculations illustrated in this chapter will focus more on the cystral structure, including the cantering of perovskites, and energetics of the RP phases, particularly looking at effects illustrated by Lei Yan et al. [48] mentioned above with $n > 4$ being grown on a $SrTiO_3$ substrate with PLD. A $SrTiO_3$ substrate was

chosen due to the lattice mismatch of only 4.5% between $SrTiO_3$ (a=3.905Å) and $CaMnO_3$ (a=3.73Å)

3.1.3 Setup of Calculations

A variety of calculations were performed to investigate the characteristics for the RP structures. Structures were optimised using the plane-wave basis set DFT electronic structure program VASP (v4.6.26) [34]. For the calculations reported here the Generalized Gradient Approximation of Perdew and Wang (GGA-PW91) [22] was used for geometry optimisation. All calculations were performed with the system spin polarised with no fixed magnetic moment set and with the spin not constrained i.e. antiferromagnetic.

Initially 1×1×1 unit-cells of the RP phases were optimised. The atom cores were represented by the ultra-soft pseudo-potentials [52]. When optimising the structures I evaluated three different paths to optimisation to determine if any one method was more suitable that the other. These were:

- Let the atom positions relax first keeping the cell constants fixed, then relax both simultaneously.
- Relax the cell constants first, then both atoms and cell simultaneously.
- Relax both the cell constants and atom positions simultaneously.

The three methods resulted in near identical results with no obvious preference shown in the accuracy of the optimised structure or the computational time taken. The total energies of the systems were all -101.317eV further showing no differentiation in the final structures. Figure 3.3 shows the optimised strucutre that is obtained via all three methods for a $n = 1$ layered RP phase.

Table 3.1 shows a selection of the measurements for the $n = 1$ RP phase to illustrate further there is no preferred method in obtaining a theoretically optimised structure. These results were reciprocated over higher values of n for a 1×1×1 unit cell. For the results shown in this chapter and other further calculations the method of relaxing both cell and atoms simultaneously were used. Calculations were performed on the 1×1×1 unit-cells of $CaMnO_3$ tetragonal and orthorombic phases and $n = 1 - 6$ $CaO(CaMnO_3)_n$ RP phases.

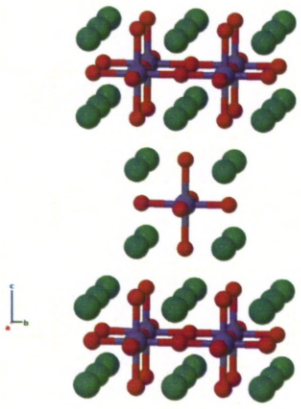

Figure 3.3: $n = 1$ Ruddlesden Popper Structure achieved by all optimisation methods. Purple: Mn; Red: O; Green: Ca

Table 3.1: Measurements for $n = 1$ RP Phase from three methods of optimisation

Measurement	Relax Atoms First	Relax Cell First	Relax Both	Experimental
a	3.733Å	3.732Å	3.733Å	3.730Å
b	3.733Å	3.731Å	3.734Å	3.730Å
c	11.605Å	11.594Å	11.607Å	12.045Å
Mn-O6 Bond	1.92Å	1.92Å	1.92Å	1.89Å
Mn-O1 Bond	1.92Å	1.92Å	1.92Å	2.07Å
Ca-Ca (Layer height)	3.33Å	3.33Å	3.33Å	3.35Å
O1-Mn-O2	89.8°	89.6°	89.7°	87.2°
O1-Mn-O3	89.8°	89.6°	89.7°	87.2°
O1-Mn-O4	89.8°	89.6°	89.7°	87.2°
O1-Mn-O5	89.8°	89.6°	89.7°	87.2°
O6-Mn-O2	90.2°	90.4°	90.3°	92.8°
O6-Mn-O3	90.2°	90.4°	90.3°	92.8°
O6-Mn-O4	90.2°	90.4°	90.3°	92.8°
O6-Mn-O5	90.2°	90.4°	90.3°	92.8°

To further investigate the RP phases with particular attention paid to the development of the perovskite layers the 2x2 unit-cells of $CaMnO_3$ tetragonal and orthorhombic phases and n=1-6 $CaO(CaMnO_3)_n$ RP phases were also studied with Ultra-soft Pseudo-potentials.

Further to this the LDA+U, or in this case GGA+U method, was used with a 2×2×1 unit-cell for the above phases to offer a comparison of methods to the GGA functional. The reason being the GGA+U method can better describe the localised states found in Mn. Yang and Ye [53] used the LSDA+U method for double pervoskites $Sr_2(Mn_{1-x}Fe_x)MoO_6$ with a Couloumb U parameter for Mn ions of 3.0eV and an exchange J parameter of 0.7eV. This was used as a basis for choosing J=1.0eV and U values of U=3.0eV and U=4.0eV for the GGA+U functional in the present study. The GGA+U calculations were ran with PAW pseudo-potentials.

With the original motivation behind these studies involving why PLD is needed to obtain $n > 4$ RP phases 2×2×1 unit-cells of $n = 4$ and $n = 5$ were investigated with the cell lattice parameters fixed and with the a and b values fixed to that of the corresponding values of a $SrTiO_3$ substrate to simulate the effect the $SrTiO_3$ substrate has on the RP phases without the need for a larger supercell with $SrTiO_3$ explicity included in the calculation.

All calculations were run in P1 and a 3×3×3 k-point mesh.

3.2 Results

3.2.1 Ruddlesden - Popper Layered Structures

The results section will look at each individual phase for the different calculation methods with a comparison of measurements to further illustrate any possible trends.

$CaMnO_3$

The main component of the $CaO(CaMnO_3)_n$ RP structures is that of $CaMnO_3$. In the RP phases it adopts a tetragonal structure, however bulk $CaMnO_3$ is known to be orthorhombic [49]. We will look at both the tetragonal and orthorhombic phases here. The orthorhombic structure can be regarded as a distorted cubic perovskite containing four formula units and two different oxygen sites [54].

In Figures 3.4 and 3.5 we can see the polyhedra representation with the MnO_6 octahedra and also the Mn-O bonding within the perovskite structure of the 1×1 and 2×2×1 unit-cells. In the 1×1×1 unit-cell we find the Mn-O1 and Mn-O6 (see figure 3.1 for atom labeling) have bond lengths of 2.18Å and 1.78Å. For the 2×2×1 cell we find average Mn-O bond lengths of 1.88Å for Mn-O1 and 1.92Å for Mn-O6 in the four main 1×1×1 blocks. The tetragonal basis of the structure is maintained for the 1×1×1 case with the a and b lattice parameters being 3.69Å although there is a slight difference in the 2×2×1 case with a=7.45Å and b=7.42Å. In the 1×1×1 we see a greater deviation in the O-Mn-O bonds from 90° in the MnO_6 octahedra in the c-axis direction with an average deviation of 8.55°. Similarly for the 2×2×1 unit-cell we see average deviations of 2.82°. The Ca-Ca distance along the c-axis decreases by 4.3% from the 1×1×1 case (3.97Å) to the 2×2×1 case (3.8Å). In the ab plane the Mn-O bond lengths are 1.87Å for the 1×1×1 cell and vary between 1.85Å and 1.97 for the 2×2×1 unit-cell.

When we look at the Mn-O-Mn bonding angles we can see a less distorted perovskite in the 1×1×1 unit-cell with the bonding angle being 178.1°. However, in the 2×2×1 unit-cell we see similarities to the orthorhombic structure with a four formula unit. Consequently, in the ab plane the Mn-O-Mn angles vary between

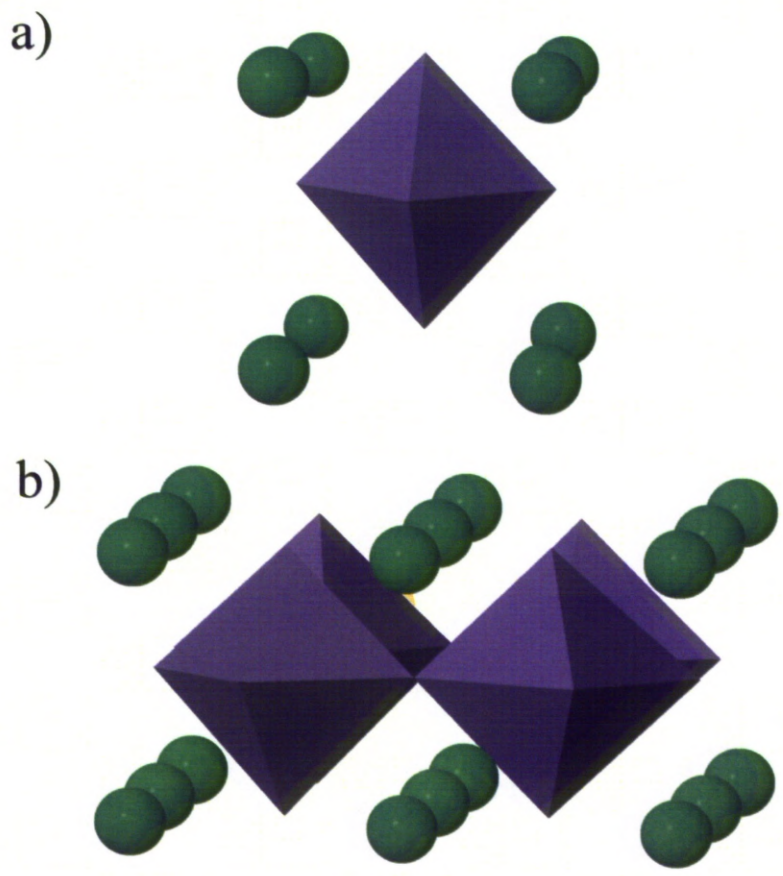

Figure 3.4: $CaMnO_3$ a) 1×1 b) 2×2×1 Polyhedra Comparison. Purple: MnO_6 polyhedra; Green: Ca

154.3° and 157.0°.

The $CaMnO_3$ tetragonal structure GGA+U calculations for U=3 and U=4 in a 2×2×1 unit-cell are similar to that of the 2×2×1 GGA calculations. U=4 gives an enlarged cell when compared with U=3 with a 0.11Å increase in the Mn-O1 and Mn-O6 bond lengths across all 1×1×1 blocks in the 2×2×1 unit-cell. The Mn-O6 bond lengths are 2.1Å and 2.21Å and the Mn-O1 bond lengths are 1.78Å and 1.89Å for U=3 and U=4 respectively. Both U=3 and U=4 maintain the tetragonal nature of the structure with a=b=7.43Å and a=b=7.46Å respectively. For the deviations in the angles from the ideal MnO octahedra the U=3 case matches more with the 1×1×1 unit-cell with average deviations of 6.72° with the U=4 case having deviations of 2.8°.

As the GGA+U calculations are done with a 2×2×1 unit-cell we get a similar

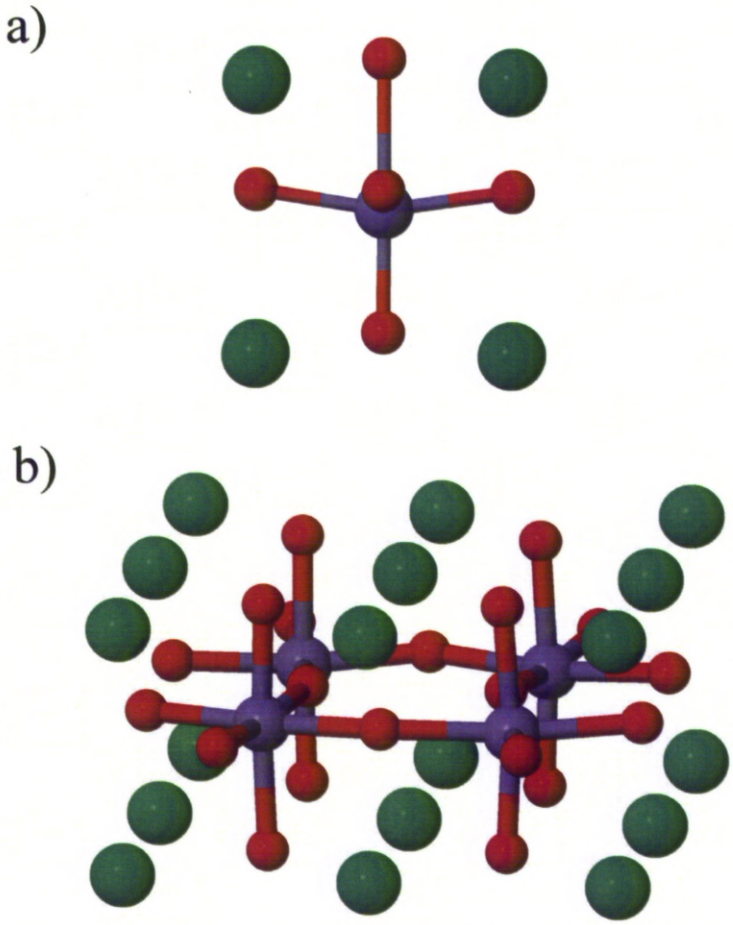

Figure 3.5: $CaMnO_3$ a) 1×1 b) 2×2×1 Comparison. Purple: Mn; Red: O; Green: Ca

outcome to the regular GGA 2×2×1 case with respect to the Mn-O-Mn angles: U=3 gives 166.6° for every Mn-O-Mn in the *ab* plane and we get 174.5° for every Mn-O-Mn angle when U=4.

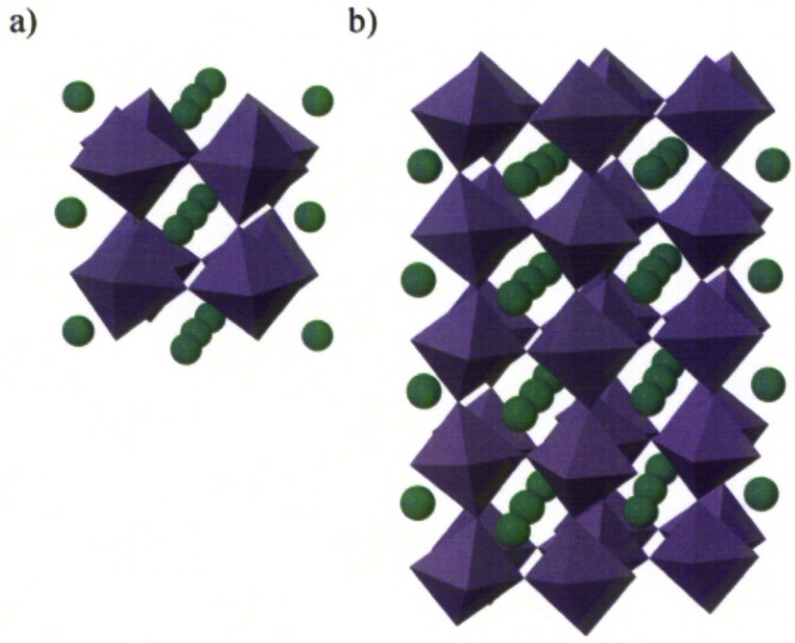

Figure 3.6: Orthorhombic $CaMnO_3$ a) 1×1×1 b) 2×2×1 Polyhedra Comparison. Purple: MnO_6 polyhedra; Green: Ca

With the GGA calculations, in the orthorhombic phase of $CaMnO_3$ the Mn-O1 and Mn-O6 bond lengths are the same in the c direction equalling 1.89Å for 1×1×1 and 2×2×1 unit-cells. The average deviation from 90° is 4.5° and 2.5° for 1×1×1 and 2×2×1 unit-cells respectively. We see a difference compared to the previous tetragonal structure with the Ca-Ca bond lengths in one layer varying from 3.68Å to 3.78Å in the 1×1×1 case and 3.63Å to 3.74Å in the 2×2×1 case.

The Mn-O-Mn angles for the 1×1×1 case are either 159.5° or 152.7°, whereas in the 2×2×1 unit-cell they are 159.4° or 153.0°. These angles can be compared to those found by Fawcett et al [51] with Mn-O-Mn angles of 152(1)° and 159.6°.

In the GGA+U calculations for we find Mn-O-Mn bond angles of 156.1° and 154.4°, all Mn-O bond lengths of 1.91Å and the Ca-Ca distance in the *ac* plane varying from 3.68Å to 3.8Å for U=3. The distortion in an individual octahedron is much smaller than for the GGA calculations with an average deviation from 90° of only 0.2° in the O-Mn-O bond angles for U=3. When U=4 the Mn-O bond lengths alternate between 1.89Å and 1.92Å between connecting octahedra

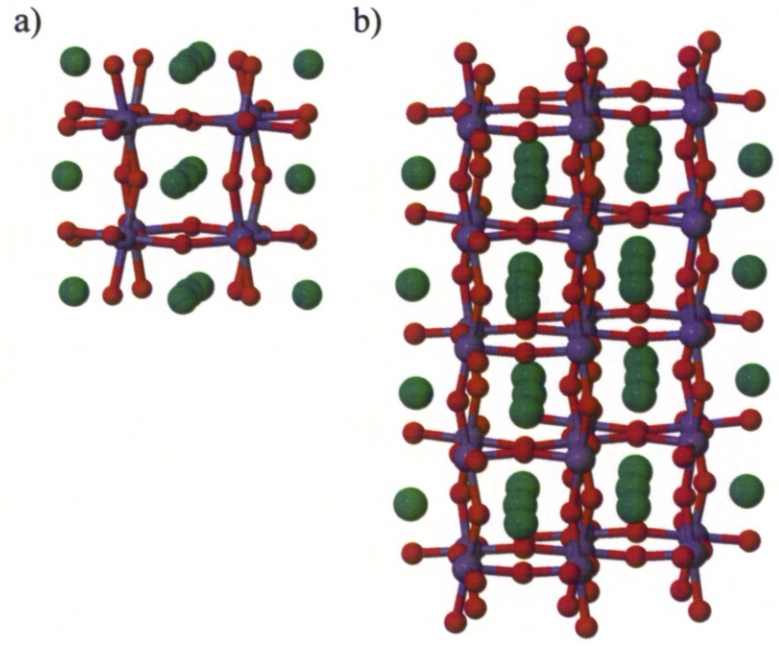

Figure 3.7: Orthorhombic $CaMnO_3$ a) 1×1×1 b) 2×2×1 Comparison. Purple: Mn; Red: O; Green: Ca

in any direction with the Ca-Ca distance in the *ac* plane varying between 3.68Å and 3.78Å. Examination of the angles gives Mn-O-Mn bond angles of 152.7° and 159.5° and an average deviation in the O-Mn-O bond angles of 4.5°.

n=1

In the $n = 1$ phase we have single $CaMnO_3$ perovskite layers separated by a CaO layer. We can see the polyhedra representation of the 1×1×1 and 2×2×1 unit-cells in figure 3.8 with a closer look at the one layer perovskite in figure 3.9. There is not much differentiation between the results of the two calculations, with both giving Mn-O1 and Mn-O6 bond lengths of 1.92Å. The Ca-Ca distance along the c-axis is 0.05Å larger at 3.38Å in the 2×2×1 case. The Ca-Ca distances in the a and b directions in the 2×2×1 unit-cell are 0.02Å smaller at 3.71Å. In both sizes of unit-cell we see an average deviation of 0.3° from 90° in the MnO octahedra. As expected from the larger height of a pervoskite layer (Ca-Ca distance in c direction) this gives the c-axis lattice parameter, c=11.66Å for 2×2×1 compared to 11.6Å for 1×1×1.

Similarly for both cases of the GGA+U calculations we see Mn-O1 and Mn-O6 bond lengths of 1.92Å. Along the c-axis we see only a 0.01Å difference between two Ca atoms in one layer with the lengths being 3.4Å and 3.39Å in the U=3 and U=4 cases respectively. The Ca-Ca distances along the a and b directions are identical for both values of U at 3.79Å. All O-Mn-O angles are 90° when U=3, but have an average deviation of 0.1° when U=4. GGA+U gives a higher value for c than GGA with c=11.75Å. The c-axis lattice paramenter found in calculations can be compared to the experimental value of 12.05Å.

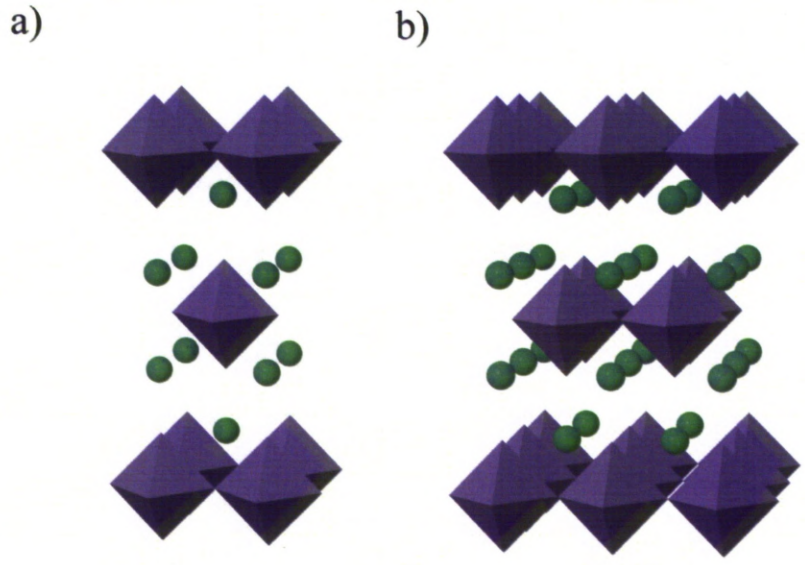

Figure 3.8: $n = 1$ a) 1×1×1 b) 2×2×1 Polyhedra Comparison. Purple: MnO_6 polyhedra; Green: Ca

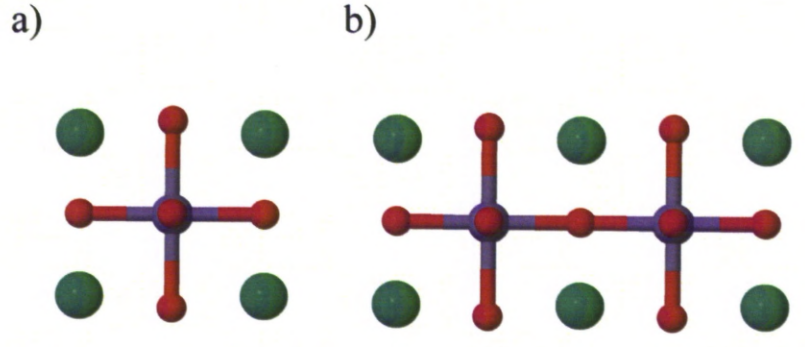

Figure 3.9: $n = 1$ a) 1×1×1 b) 2×2×1 Perovskite Layer Comparison. Purple: Mn; Red: O Green: Ca

n=2

As we start to increase n we begin to see a bigger difference between the 1×1×1 and 2×2×1 case as seen in figures 3.10 and 3.11 for $n = 2$. We see a bigger distortion in the Mn-O-Mn angle between pervoskite layers with this angle being 179.8° for the 1×1×1 case; and 160.5° and 157.1° in the 2×2×1 case. In both unit-cells we see all Mn-O bond lengths closest to the CaO layer being smaller than the connecting inward Mn-O bonds. The variance is bigger in the 1×1×1 case with the Mn-O bond length varying from 1.87Å to 1.92Å compared to the 2×2×1 unit-cell which sees variance from 1.91Å to 1.95Å.

In both $CaMnO_3$ layers of the 1×1×1 case we see the same Ca-Ca distances along the c-axis (3.47Å for both layers) with a Ca-Ca distance of 3.76Å in both a and b directions. For the 2×2×1 case the Ca-Ca distance varies from 3.73Å to 3.54Å between layers in the c-axis across the four 1×1×1 unit-cell blocks, but when averaged across all these blocks we get a Ca-Ca distance of 3.62Å for each corresponding layer. Similarly, in the a and b direction with the distances varying between 3.61Å and 3.81Å, but with an average Ca-Ca distance in a and b directions of 3.71Å.

When looking at the average O-Mn-O angle deviation in the c-axis direction we get average of 1.48° for the 1×1×1 unit-cell; and 1.77° for the 2×2×1 unit-cell.

The GGA+U calculations yield identical results for U=3 and U=4 with little distortion in the MnO octahedra. Both structures show Mn-O-Mn bond angles of 180° with the O-Mn-O bond angles deviating on average 1.55° from 90°. The Ca-Ca distance in the a and b directions are 3.73Å and 3.51Å in the c direction. The Mn-O bond lengths are consistent throughout the 2×2×1 unit-cell here as well with the two inner lying bonds having a length of 1.91Å and the two outerlying Mn-O bonds a length of 1.87Å in the c direction.

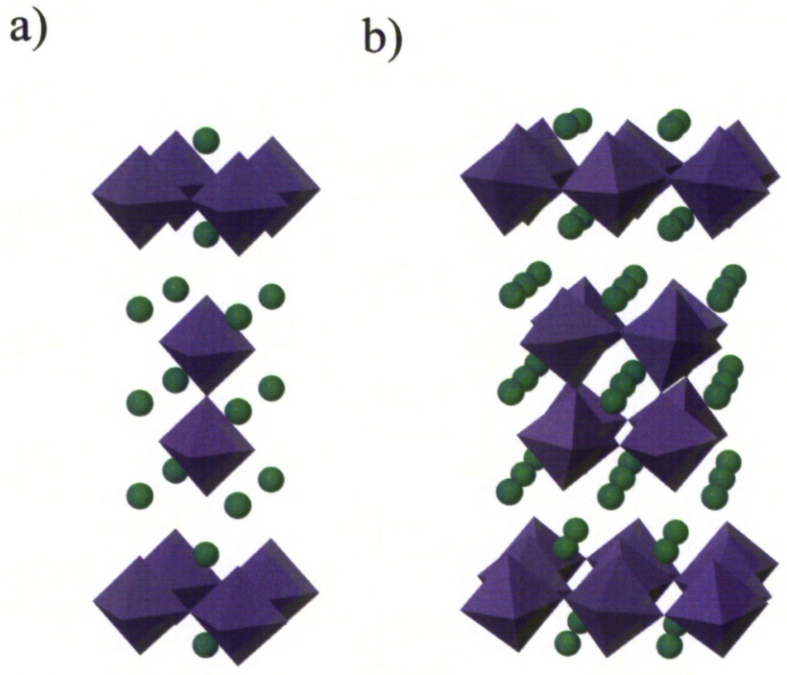

Figure 3.10: $n = 2$ a) 1×1×1 b) 2×2×1 Polyhedra Comparison. Purple: MnO_6 polyhedra; Green: Ca

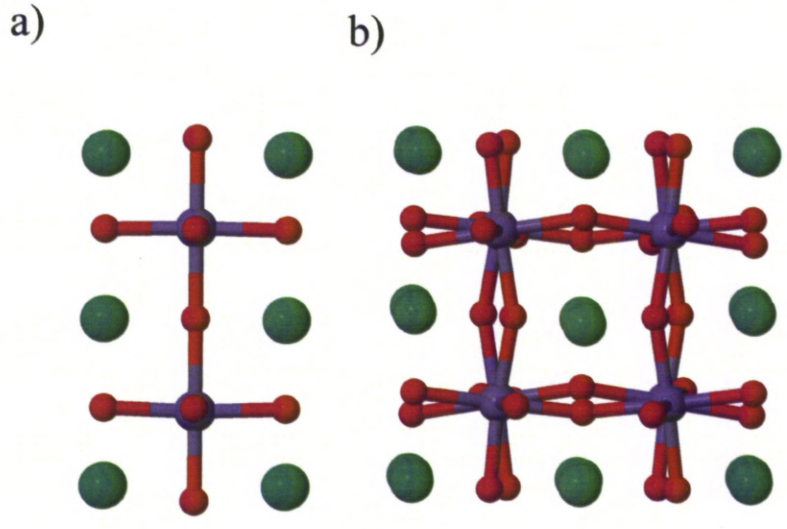

Figure 3.11: $n = 2$ a) 1×1×1 b) 2×2×1 Perovskite Layer Comparison. Purple: Mn; Red: O Green: Ca

n=3

We begin to see greater differentiation in the Mn-O bond lengths for the $n = 3$ 1×1×1 unit-cell (Figures 3.12a and 3.13a). Along the c-axis these range from 1.86Å to 1.94Å. In comparison for the 2×2×1 unit-cell (Figures 3.12b and 3.13b) they take the smaller range of 1.91Å to 1.95Å across all equivalent 1×1×1 blocks. In both unit-cells we see the largest Mn-O bond lengths being 2nd closest to the CaO rocksalt layer at either side of the three layer perovskite. For the 1×1×1 unit-cell we see an enlargement in the height in the middle layer with the Ca-Ca length in the c direction being 3.48Å for the outer lying layers and 3.7Å for the middle layer. For the 2x2 case there is a difference in the equivalent Ca-Ca distance in the a and b directions for all 1×1×1 blocks with a range of 3.46Å to 3.93Å across the 2×2×1 unit-cell. As with the 1×1×1 case though, when we average the corresponding heights of each layer we get heights of 3.61Å for the outer layers and 3.73Å for the middle layer. In the a direction the Ca-Ca distance varies from 3.51Å to 3.82Å, with an average of 3.72Å and in the b direction from 3.68Å to 3.76Å with an average of 3.73Å.

The O-Mn-O angle deviation from 90° continues to increase as n increases for the 1×1×1 unit-cell with the average deviation being 2.40°. In comparison we see an average deviation of 1.62° for the 2×2×1 unit-cell. It is clear from figure 3.13 that there is increased tilting of the octahedra in the 2×2×1 cell compared to the 1×1×1. We see Mn-O-Mn bonding angles of 173.0° and 172.8° for the 1×1×1 cell which creates a larger deviation from being planar than for $n = 1$ and $n = 2$ for the corresponding cell. The Mn-O-Mn angles range from 154.6° to 157.5° in the 2×2×1 cell where the octahedra are more tilted. The Mn-O-Mn angles here are now of a similar range to those in the orthorhombic $CaMnO_3$ structure.

The GGA+U calculations for a 2x2 unit-cell show similar trends to the GGA calculations. When U=3, a=b=7.44Å and when U=4 a=b=7.45Å. As with the GGA case the Mn-O bond lengths have a smaller range when compared to a 1×1×1 unit-cell with a range of 1.89Å to 1.94Å and 1.9Å to 1.94 for U=3 and U=4 respectively. For U=3 and U=4 there is a difference in the Ca-Ca distance in the a and b directions for the 1×1×1 blocks compared to the GGA calculations. For U=3 the 'depth' of the layer, i.e. the Ca-Ca distance in the a direction varies

from 3.59Å to 3.8Å with an average of 3.72Å in the 2×2×1 unit-cell and the width of a layer, i.e. the Ca-Ca distance in the b direction, varies from 3.69Å to 3.76Å with an average of 3.73Å. Similarly for U=4 the depth of a 1×1×1 representative cell changes from 3.58Å to 3.81Å and the width from 3.67Å to 3.77Å, with both averaging 3.73Å.

The angle deviations of the O-Mn-O for GGA+U are smaller than that of GGA with for U=3 the average deviation being 1.28° and 1.31° when U=4. The Mn-O-Mn angles range from 157.1° to 159.1° for U=3 and 156.8° to 159.0° for U=4.

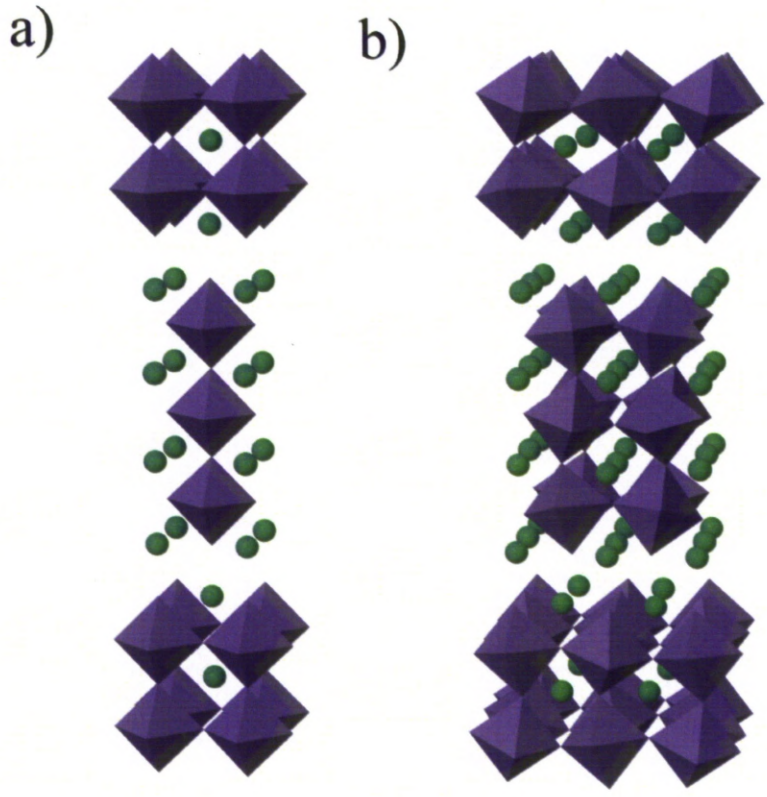

Figure 3.12: $n = 3$ a) 1×1×1 b) 2×2×1 Polyhedra Comparison. Purple: MnO_6 polyhedra; Green: Ca

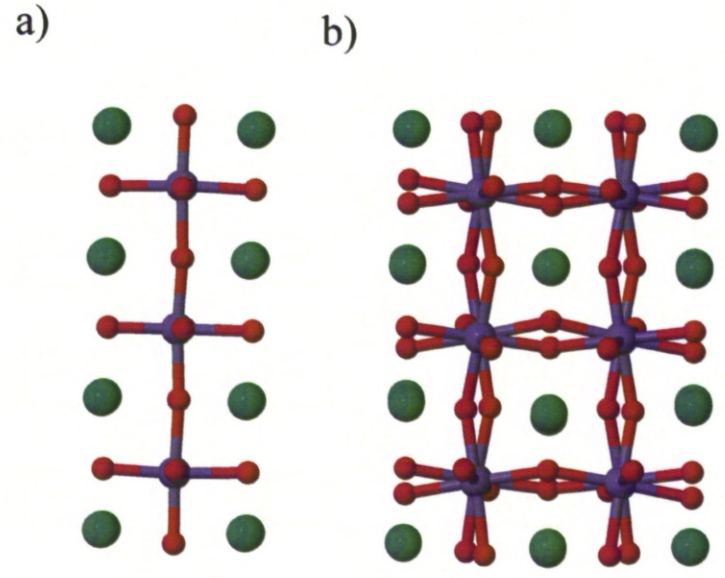

Figure 3.13: $n = 3$ a) 1×1×1 b) 2×2×1 Perovskite Layer Comparison. Purple: Mn; Red: O Green: Ca

n=4

For $n = 4$ the RP structure was formed using PLD on a STO substrate so this compound is not known as a bulk phase. However, the calculations here are assuming they are bulk phases to save computationally expensive large supercell calculations. Figures 3.14 and 3.15 illustrate the difference mainly seen with the greater tilting of the MnO_6 in the 2×2×1 unit-cell. The Mn-O-Mn bonding angle varies from 169.5° to 172.0° in the 1×1×1 unit-cell and 151.6° to 154.7° in the 2×2×1 unit-cell. There starts to be differences in the trends of the average O-Mn-O deviation with the average angle increasing further compared to n=3 for the 1×1×1 cell with a average deviation of 3.0°. For the 2×2×1 cell we see a reduction in the average deviation compared to n=3 with the average deviation from 90° being 1.35°. This causes a frustrated octahedra in the 1×1×1 unit-cell which compensates the inability to tilt within a smaller unit-cell by a bigger deviation within individual octahedron.

The spread of Mn-O bond lengths in the c direction show a slight increase for both 1×1×1 and 2×2×1 cells with distances ranging from 1.85Å to 1.94Å and 1.89Å to 1.96Å respectively. For 1×1×1 a=b=3.77Å maintaining the tetragonal shape with the two edge layers closest to the CaO layer having a smaller Ca-Ca distance (3.48Å and 3.49Å) compared to the height of the middle layers (3.71Å). This shows some compression to re-organise to match with the CaO layer. This is not seen in individual 1×1×1 blocks in the 2×2×1 unit-cell as there are differing measurements for the depth and width of each perovskite layer creating a distorted perovskite. The depth of a 1×1×1 block ranges from 3.53Å to 3.92Å with the width from 3.67Å to 3.77Å. The variance in the height of each perovskite layer is due to the distortion of each layer in each representation in the 2x2 unit-cell. When averaged across the whole unit-cell we obtain an average Ca-Ca distance in the a direction of 3.73Å and 3.72Å in the b direction. When looking at the Ca-Ca distances in the c direction we see a similar trend as with the 1×1×1 case with the two layers closest to the CaO layer both having an average of 3.61Å whilst the middle layers have an average Ca-Ca distance of 3.74Å. For the 2×2×1 unit-cell we see lattice parameters of a=7.45Å and b=7.43Å.

In the GGA+U calculations we see the same range of Mn-O bond lengths in the c

direction as for to n=3 with measurements ranging from 1.89Å to 1.94Å and 1.9 to 1.94Å for U=3 and U=4 respectively. When U=3 we obtain lattice parameters of a=7.45Å and b=7.44Å and for U=4, a=7.46Å and b=7.45Å. Once again the average angle deviation for U=3 and U=4 is less than that of the GGA calculated case, with the deviations of 1.20° when U=3; and 1.21° when U=4. The Mn-O-Mn bonding angles range from 154.5° to 157.8° and 154.4° to 157.5° for U=3 and U=4 respectively.

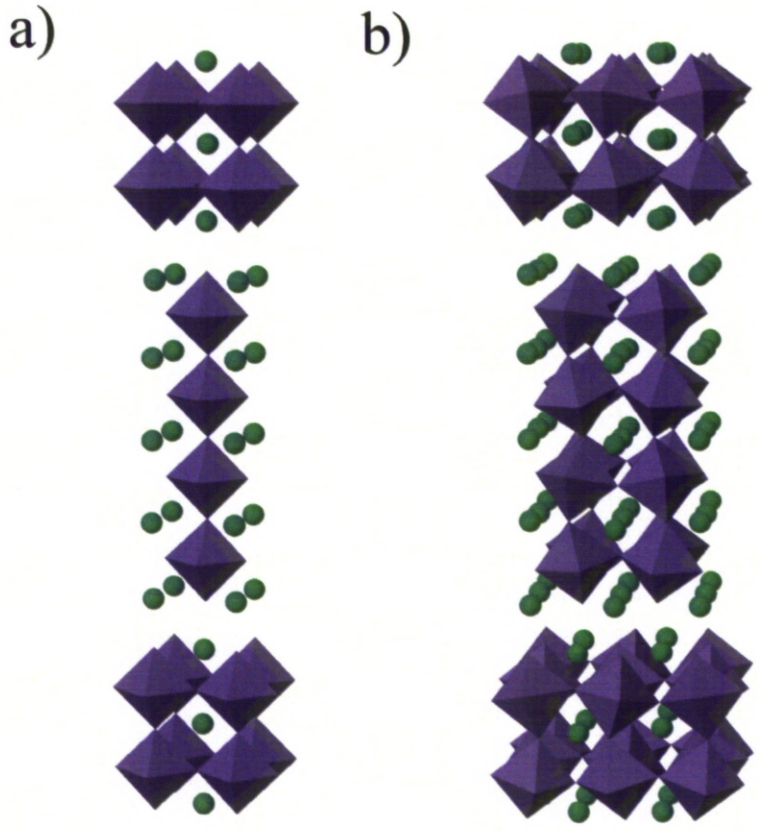

Figure 3.14: $n = 4$ a) 1×1×1 b) 2×2×1 Polyhedra Comparison. Purple: MnO_6 polyhedra; Green: Ca

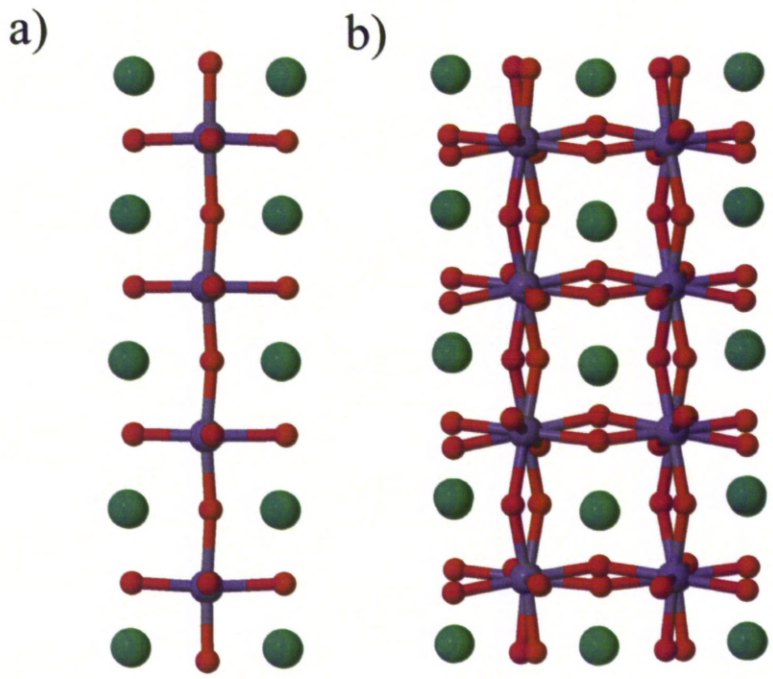

Figure 3.15: $n = 4$ a) 1×1×1 b) 2×2×1 Perovskite Layer Comparison. Purple: Mn; Red: O Green: Ca

Since the $n = 4$ compound is formed using PLD on a $SrTiO_3$ substrate the effect this had on the structure compared to the 'bulk phase' needed to be investigated. A very large supercell could have been created with a $SrTiO_3$ substrate, with this would have been computationally much more expensive particularly when the size of the $SrTiO_3$ used in experiment consisted of 22 layers and the detailed structure at the interface is unknown. To counteract this we performed calculations fixing the lattice parameters to match those of $SrTiO_3$ in the a and b directions, but kept to the original c=34.66Å. Calculations were done with GGA in a 2×2×1 unit-cell looking at any observed distortion in the perovskite, and used the original experimental structures as a starting point for calculation with the new a and b lattice parameters. This provided the results illustrated in figure 3.16.

As can be seen the Mn-O-Mn bonding is 180° in every instance which means there is no tilting of the octahedra. The size and trend of the height of each layer in each block matches with the 1×1×1 case with the Ca-Ca distance being smallest at the outer layers (3.55Å) and largest in the two middle layers (3.78Å). The measurements across all 1×1×1 representations are identical with Mn-O bond lengths ranging from 1.89Å to 1.95Å and the depth and width of each layer being 3.9Å. The averaged angle deviation from 90° for the O-Mn-O bonds is measured as 1.35°.

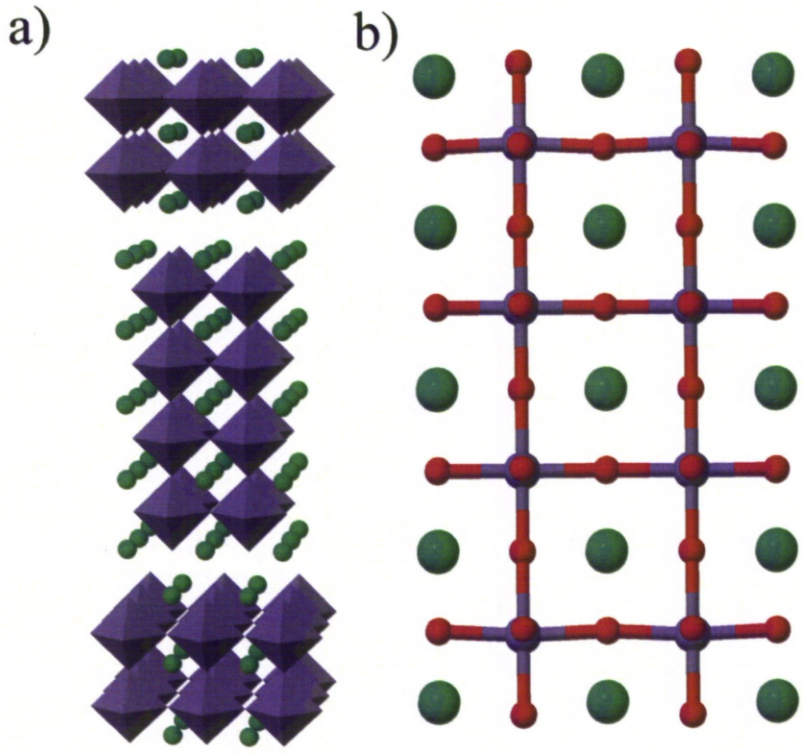

Figure 3.16: $n = 4$ with restricted STO lattice a) Polyhedra representation b) Perovskite layer representation. Purple Polyhedra: MnO_6; Purple: Mn; Red: O Green: Ca

n=5

For $n = 5$ we see the first case where the structure changes from tetragonal to orthorhombic for the 1×1×1 unit-cell (Figures 3.17a and 3.18a) with the calculated lattice parameters being a=3.82Å, b=3.74Å and c=41.29Å. For the 2×2×1 cell (Figures 3.17b and 3.18b) we get a=7.46Å, b=7.44Å and c=41.54Å. Although, the a and b parameters remain similar in the 2×2×1 case as per smaller values of n this is offset with the distorted perovskite layers having a depth ranging from 3.61Å to 3.76Å and a width varying between 3.63Å and 3.82Å. In both the 1×1×1 and 2×2×1 cells the smallest distance between two Ca atoms is for the two outermost layers (3.6Å to 3.62Å for 2×2×1; and 3.48Å and 3.52Å for 1×1×1). The 1×1×1 case once again displays a bigger spread in the Mn-O bond lengths in the c direction (1.85Å to 1.95Å) compared to the 2×2×1 cell (1.89Å to 1.94Å).

The averaged angle deviation from 90° for the O-Mn-O bonds for the 1×1×1 unit-cell is slightly reduced in comparison to $n = 4$ with a value of 2.94°. For the 2×2×1 cell the average deviations are 1.14°. Compared to lower values of n, the 1×1×1 cell for $n = 5$ shows increased perovskite tilting with the Mn-O-Mn bond angles ranging from 167.6° to 174.6°.

In the GGA+U calculations for U=3 and U=4 we see calculated Mn-O distances range from 1.89Å to 1.93Å. The lattice parameters in the a and b directions illustrate tetragonal cells for U=3 (a=b=7.45Å) and U=4 (a=7.47Å b=7.46Å). As with other cases of n, the distorted perovskite creates differing values of the depth and width of a layer despite the matching a and b lattice parameters for the whole 2×2×1 unit-cell. When U=3 the depths range from 3.69Å to 3.81Å and the widths ranging from 3.71Å to 3.75Å, both with an average of 3.73Å across the 2×2×1 cell. Similarly, for U=4 the depths range from 3.63Å to 3.75Å with an average of 3.74Å and the widths from 3.65Å to 3.81Å with an average of 3.73Å. The averaged angle deviations from 90° of the O-Mn-O bonds vary from 1.04° for U=3 and 1.02° for U=4. We can also see a spread in Mn-O-Mn angles in the c direction of 155.6° to 160.2° and 155.4° and 159.7° for U=3 and U=4 respectively.

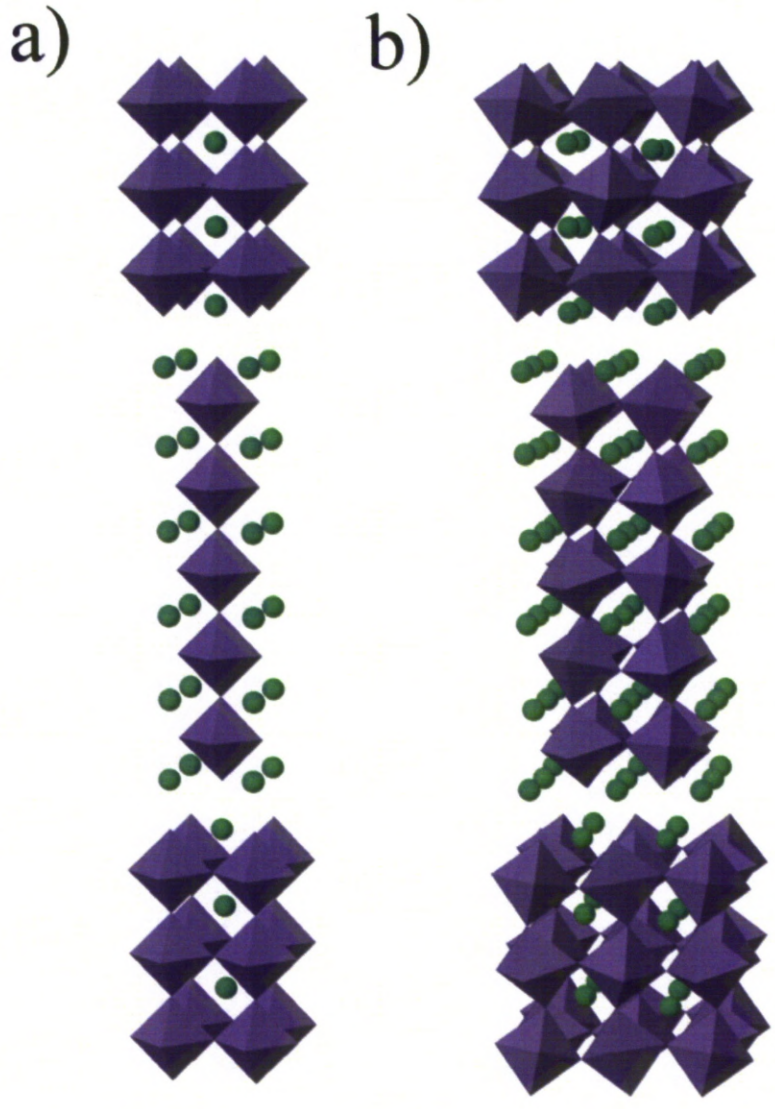

Figure 3.17: $n = 5$ a) 1×1×1 b) 2×2×1 Polyhedra Comparison. Purple: MnO_6 polyhedra; Green: Ca

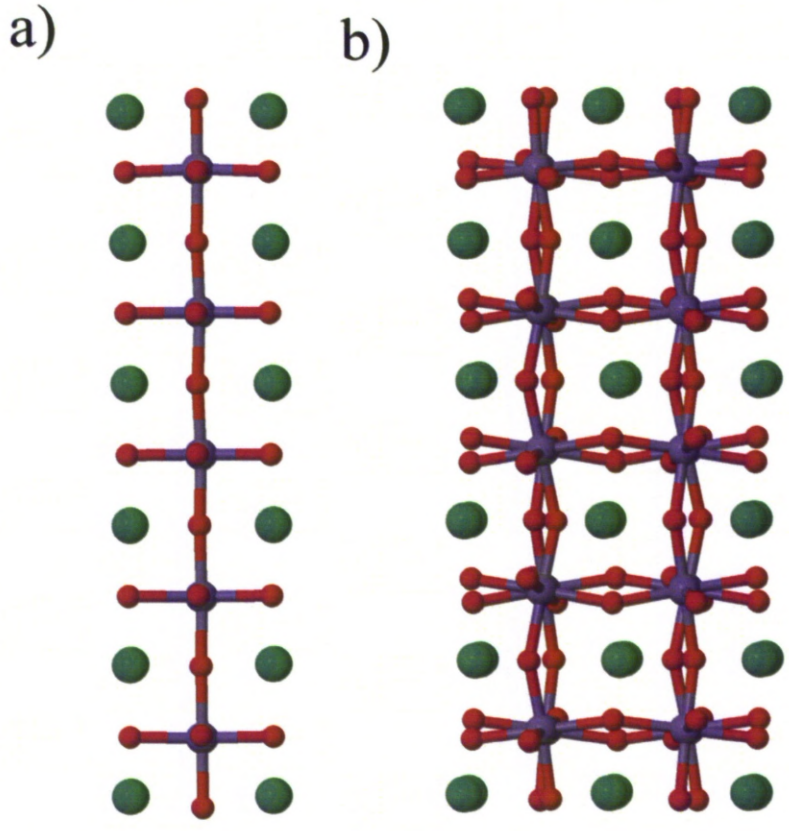

Figure 3.18: $n = 5$ a) 1×1×1 b) 2×2×1 Perovskite Layer Comparison. Purple: Mn; Red: O Green: Ca

Fixing the lattice parameters to those of $SrTiO_3$ in the a and b directions does not reduce perovskite distortion as with the $n = 4$ compound. The Mn-O-Mn angles range from 151.2° to 154.1° along the c direction. The averaged angle deviation is larger than other calculations with a 2×2×1 unit-cell (1.86°). The distortion in the perovskite blocks can be further seen with the depths (3.8Å to 3.97Å) and widths (3.89Å to 3.91Å) varying between formula unit-cells. However, the average of the width and the depth are both 3.90Å.

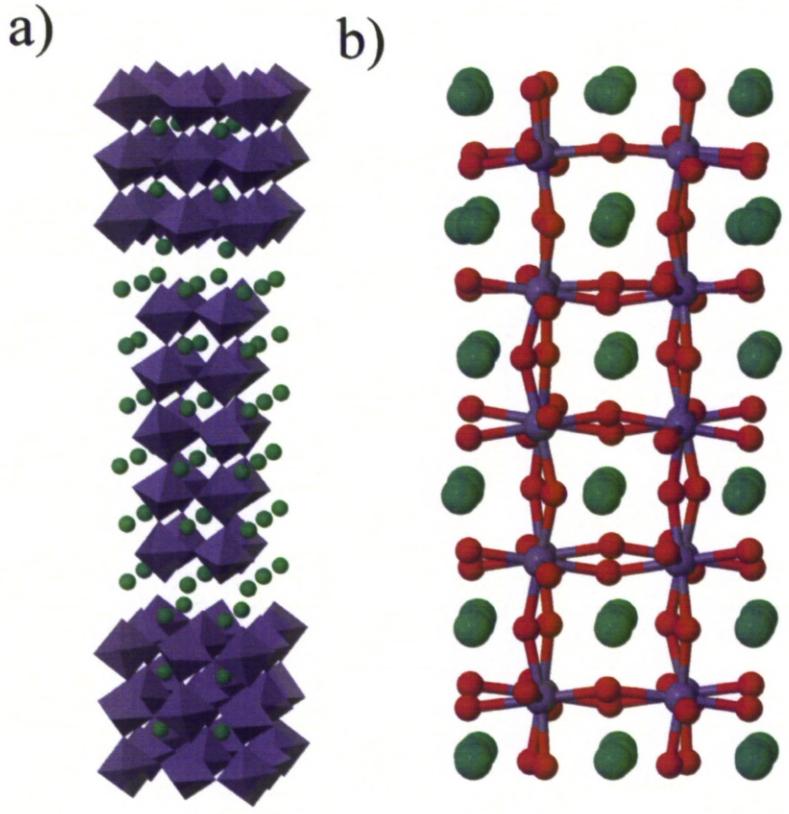

Figure 3.19: $n = 5$ with restricted STO lattice a) Polyhedra representation b) Perovskite layer representation. Purple Polyhedra: MnO_6; Purple: Mn; Red: O Green: Ca

n=6

Due to the number of atoms in a $n = 6$ compound only the 1×1×1 unit-cell was used for calculations. Here we see further characteristics of perovskite distortions with the Mn-O-Mn bonds varying between 166.5° and 169.7°. Here a=3.80Å and b=3.79Å with, in the c direction, the smallest height of a layer (3.46Å) is from the outermost layers that interconnect with the CaO layer. The Mn-O bond lengths along the same direction vary from 1.85Å to 1.94Å and the average angle deviation from 90° for the O-Mn-O bond angles is larger here than for $n = 1 - 5$ with a value of 3.92°.

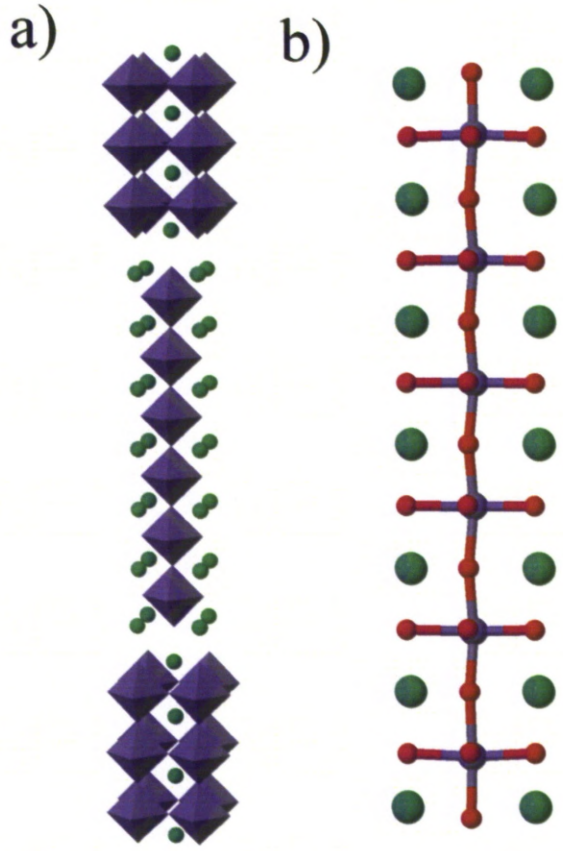

Figure 3.20: $n = 6$ a) Polyhedra representation b) Perovskite Layer Representation. Purple Polyhedra: MnO_6; Purple: Mn; Red: O Green: Ca

LSCMO Structure

The LSCMO structure of the form $La_{1-x}A_xMnO_3$ where in this case A=Ca. This is a $n = 6$ layer RP compound with Lanthanum doping of some Ca sites. A 2×2×1 unit-cell calculation was performed on this structure to further investigate the effects seen in the $n = 4$ compound with a restricted STO a and b lattice parameters to look at the effect a layer of another element has on the perovskites. By looking at the Mn-O-Mn angles we can see that the tilting of the MnO_6 octahedra reduces when they contain the Manganese in the La layer (168.8° to 175.6°) compared to the Mn-O-Mn angles solely in the Calcium layers (152.8° to 161.5°). This further highlights that specific doping or restriction of lattice parameters via any method can result in a reduction of the distortion of the perovskites.

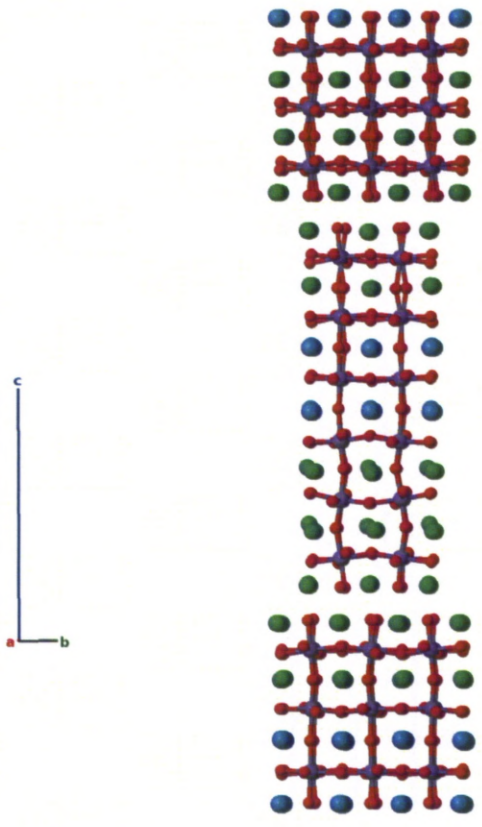

Figure 3.21: LSCMO $n = 6$ structure. Purple: Mn; Red: O; Light Blue: La; Green: Ca

Lattice Parameters

The following tables detail the lattice parameters determined for each structure with each type of calculation.

Table 3.2: Lattice Parameters for Investigated structures for 1×1×1 unit-cell

Structure	a (Å)	b (Å)	c (Å)
$CaMnO_3$ tetragonal	3.70	3.70	3.97
$CaMnO_3$ orthorhombic	5.28	7.35	5.20
n=1	3.73	3.73	11.60
n=2	3.76	3.76	18.94
n=3	3.76	3.77	26.41
n=4	3.78	3.76	33.86
n=5	3.82	3.74	41.30
n=6	3.80	3.80	48.57

Table 3.3: Lattice Parameters for Investigated structures for 2×2×1 unit-cell

Structure	a (Å)	b (Å)	c (Å)
$CaMnO_3$ tetragonal	7.36	7.36	3.85
$CaMnO_3$ orthorhombic	10.53	14.74	5.19
n=1	7.43	7.43	11.66
n=2	7.42	7.42	19.30
n=3	7.44	7.44	26.68
n=4	7.44	7.43	34.19
n=5	7.46	7.44	41.54
LSCMO	7.56	7.58	49.95

Table 3.4: Lattice Parameters for Investigated structures for 2×2×1 unit-cell (1×1×1 for $CaMnO_3$ orthorhombic) with U=3 in GGA+U calculations

Structure	a (Å)	b (Å)	c (Å)
$CaMnO_3$ tetragonal	7.43	7.43	3.88
$CaMnO_3$ orthorhombic	5.31	7.46	5.26
n=1	7.42	7.42	11.76
n=2	7.45	7.45	19.10
n=3	7.45	7.44	26.81
n=4	7.45	7.44	34.30
n=5	7.46	7.45	41.70

Table 3.5: Lattice Parameters for Investigated structures for 2×2×1 unit-cell with U=4 in GGA+U calculations

Structure	a (Å)	b (Å)	c (Å)
$CaMnO_3$ tetragonal	7.43	7.43	3.95
$CaMnO_3$ orthorhombic	5.27	7.45	5.26
n=1	7.42	7.42	11.76
n=2	7.45	7.45	19.10
n=3	7.46	7.46	26.84
n=4	7.46	7.45	34.34
n=5	7.47	7.46	41.75

Comparison of Measurements between differing layers

c-axis measurements

Figure 3.22 shows a comparison of the c-axis lattice parameter of the experimental data and computational data for the 1×1×1 and 2×2×1 unit-cell for each value of n from one to six. The graph shows the c-axis lattice parameter divided by the number of layers, n, to show the compression of the structures in the c-axis as n increases. The computational results obtained from VASP are represented by the red and blue lines, the results obtained by experiment [48] are illustrated by the black line.

In Yans 2007 paper [48] conclusions were reached about the difference between the actual and expected results. The expected c-axis lattice parameter for the n =4, 5 and 6 structures were deduced from the experimental results of the n =1, 2 and 3 structures formed by conventional synthesis methods. The expected c values of 34.65Å, 42.19Å and 49.72Å were deduced in the absence of strain or of variations in composition and octahedral tilting. But once we increase n beyond this point the experimental results show that there is a contraction of the RP compound as shown by the experimental c values of 34.12Å, 41.46Å and 49.11Å. The VASP calculated data matches the values obtained by experiment within an expected DFT error range but maintains the same interpreted outcome were we can see the contraction at higher values of n compared to the 'expected' results still occurs.

In Figure 3.22 the 2×2×1 unit-cell matches closer to the experimental results than the 1×1×1 unit-cell, particularly so for $n = 4$ and $n = 5$. A similar trend as with the 2×2×1 unit-cell is seen for the GGA+U calculations. GGA+U (for both values of U) is a closer match to the c lattice parameter for $n = 1 - 3$ than GGA, however the opposite is true for $n = 4, 5$.

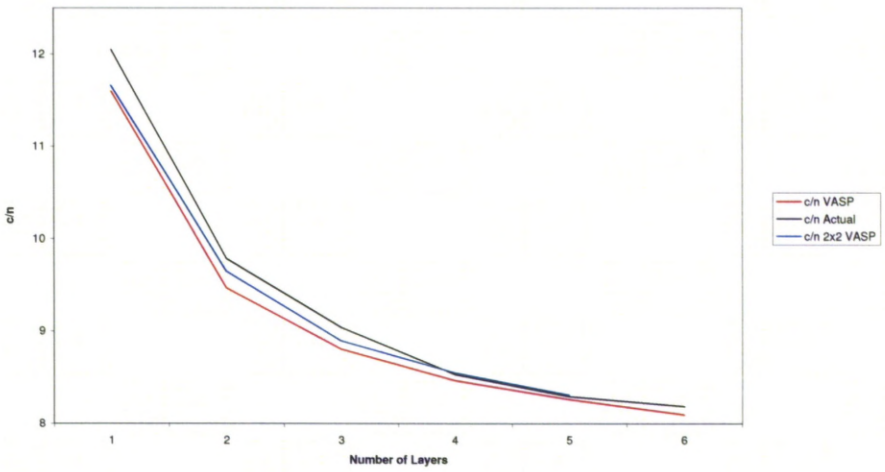

Figure 3.22: Comparison of c-axis length (Å) divided by n for 1×1×1 and 2×2×1 Ruddlesden Popper Structures.

Mn-O Bond Lengths along c-axis

As highlighted when investigating the different structures across each type of calculation trends were seen in the arrangement of the size of the layers and the Mn-O bond lengths along the c-axis.

Figures 3.23, 3.24 and 3.25 show the Mn-O bond lengths along the c-axis working from the 'bottom' Mn-O bond closest to the CaO layer up to the Mn-O bond closest to the CaO layer at the other end of the n perovskites.

In figure 3.23 we clearly see the peaks representing the largest Mn-O bonds being that of the 2nd most outerly Mn-O bonds on either side of each n layered structure apart from $n = 1$ which with only two Mn-O bonds sees both bonds equal. Similarly, the outer-most Mn-O bonds for $n = 2$, 3, 4 and 6 give the smallest Mn-O bond in their respective structures with this allowing the structures to connect with the CaO rocksalt layer. For $n = 5$ there is one smaller Mn-O bond than the

outer-lying bonds and the two largest Mn-O bonds are not the same unlike for other values of n although the general trend still exists.

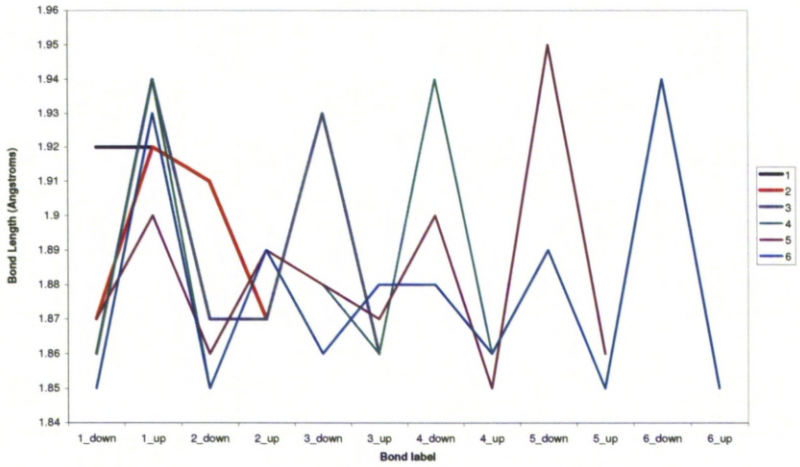

Figure 3.23: MnO bond lengths (Å) in c direction for 1×1×1 Ruddlesden Popper structures.

In the 2×2×1 unit-cell the trend seen in the 1×1×1 case is shown for $n = 1 - 4$. For $n = 5$ the re-organisation of the lengths of the Mn-O bonds across the outer lying layers is not observed in figure 3.24 and there is also a greater amount of fluctuation seen in the middle layers than seen in the 1×1×1 unit-cell. The same trend of the Mn-O length across individual layers is seen for all values of n for the GGA+U calculations.

However, when restricted to the STO lattice parameters in the a and b directions the $n = 5$ structure does show the same trend in variation of the Mn-O bond lengths (Figure 3.25) it had not shown in the 1×1×1 and 2×2×1 unit-cell calculations with fully relaxed lattice parameters. Both $n = 4$ and $n = 5$ here show the smaller outer lying Mn-O adjacent to the largest Mn-O bond with a 'flatter' range of lengths for the middle Mn-O bonds in each structure.

The calculations were started from experimental structures with their Mn-O bond lengths shown in figure 3.26. The same trend highlighted in the main in the calculated results is highlighted in $n = 4$. Here, $n = 3$ and $n = 5$ follow the

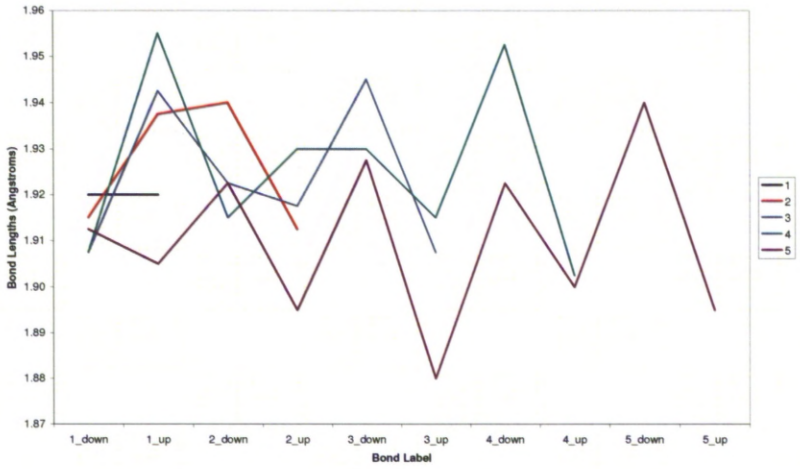

Figure 3.24: MnO bond lengths (Å) in c direction for 2×2×1 Ruddlesden Popper structures.

general trend, although the peak is much higher at one end of the structure than at the other end of the n layers. This could go some way to explain why similar problems occur for $n = 5$ in the 1×1×1 and 2×2×1 unit-cell calculations. In the $n = 1$ structure, we see differing Mn-O bond lengths unlike the calculated results and also unlike Fawcett et al in 1998 [51]. In Fawcett's paper we see both Mn-O bond lengths in the c-axis direction of 2.046(6)Å for $n = 1$ compared to the 1.92Å found in the VASP calculated results across all methods. Fawcett also found the opposite to illustrated trends noticed in this chapter with Mn-O bond lengths of 1.918(6)Å for the two inner lying Mn-O bonds and 2.09(2)Å for the outer lying bonds for $n = 2$.

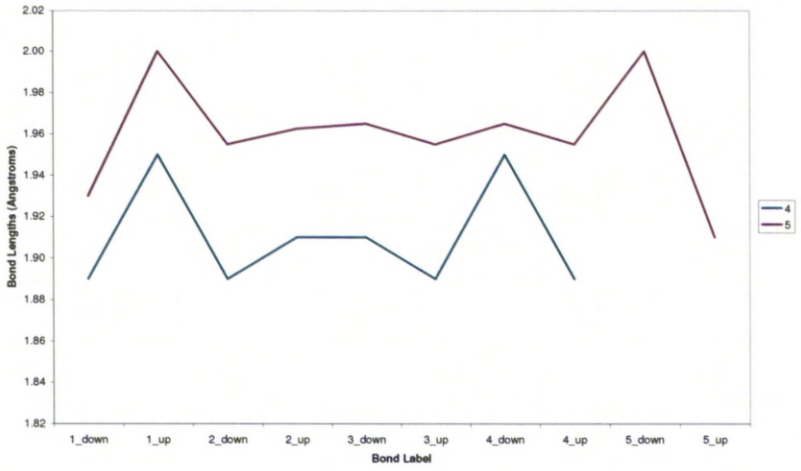

Figure 3.25: MnO bond lengths (Å) in c direction for STO $n = 4, 5$ Ruddlesden Popper structures.

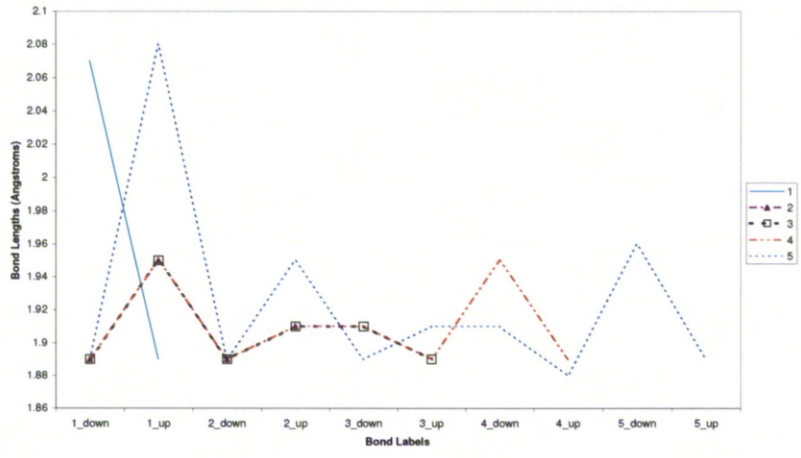

Figure 3.26: MnO bond lengths (Å) in c direction for experimental Ruddlesden Popper structures.

Size of each layer along c-axis

In figures 3.27, 3.28 and 3.29 we see the Ca-Ca distances in the c direction. This essentially represents the height of the respective layer in a structure, although at larger n in the 2×2×1 unit-cell the Ca-Ca distance is not exactly parallel to the c-axis as there is distortion of the position of the Ca in the perovskite. In all calculation methods we see the largest Ca-Ca distance arising in the middle layers and the smallest at the outer lying layers which are adjacent to the CaO layer. This is expected with the CaO layer being smaller than the perovskite layers.

In the 1×1×1 unit-cell the Ca-Ca lengths found for $n = 2 - 6$ are closer to the single layer perovskite found in the $n = 1$ compound than to the n=∞ tetragonal structure. The opposite is the case for the 2×2×1 cell with the Ca-Ca distance being closer to the $n = \infty$ structure. This is due to the octahedra tilting being more prevalent in the 2×2×1 unit-cell because it contains a four formula unit-cell seen in the orthorhombic $CaMnO_3$ structure.

In figure 3.29 obtained with a, b parameters fixed to the STO values we see a larger range of values of the height of outer lying layers compared to the two innermost layers. This is created with no tilting of the perovskites and along with the fixed lattice parameters, no subsequent distortion in the position of the calcium atoms.

A similar trend, is seen for the GGA+U calculations.

For the data taken from experiment used as a starting point for the calculations in this chapter shown in figure 3.30 we only see the same trend for the $n = 3$ and $n = 4$ structures. We see a larger Ca-Ca distance for the $n = \infty$ tetragonal $CaMnO_3$ structure than for calculations.

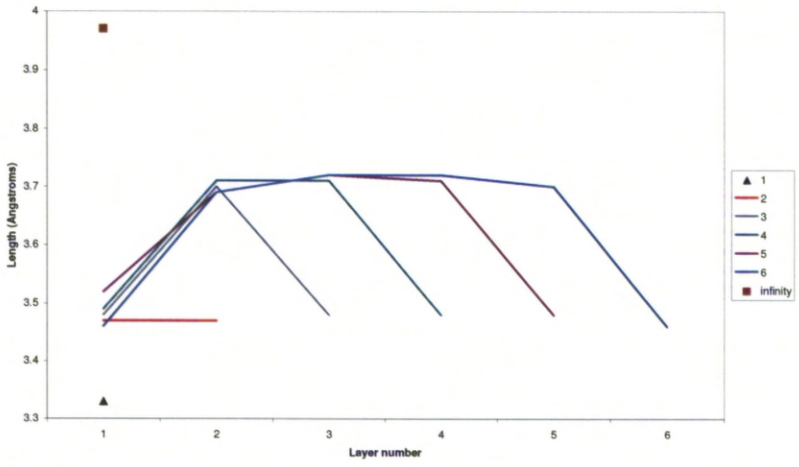

Figure 3.27: Lengths (Å) in c direction for each layer (Ca-Ca) in 1×1×1 Ruddlesden Popper structure.

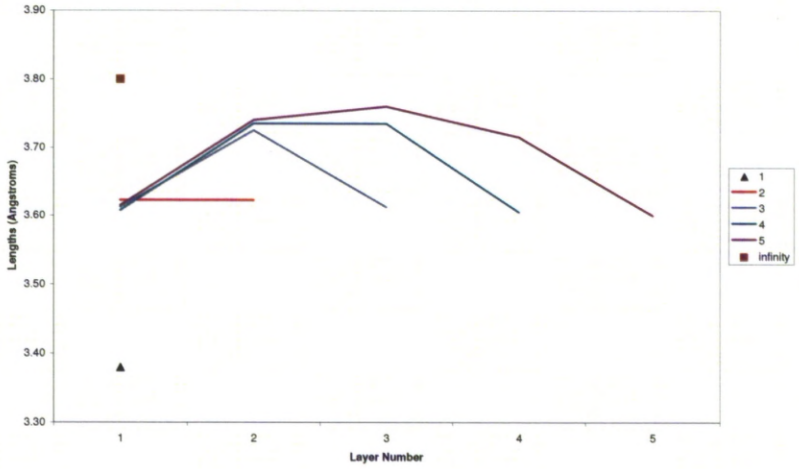

Figure 3.28: Lengths (Å) in c direction for each layer (Ca-Ca) in 2×2×1 Ruddlesden Popper structure.

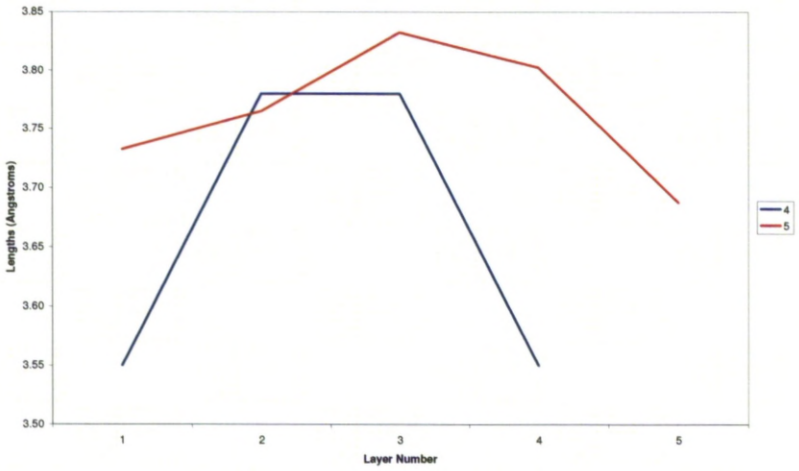

Figure 3.29: Lengths (Å) in c direction for each layer (Ca-Ca) in STO $n = 4, 5$ Ruddlesden Popper structure.

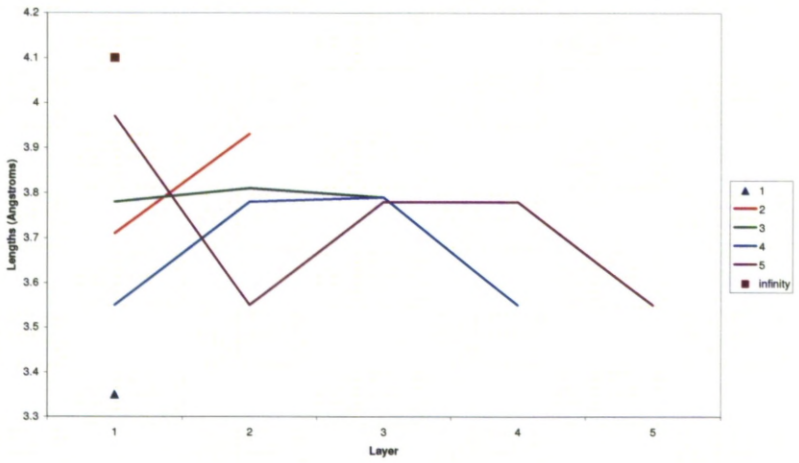

Figure 3.30: Lengths (Å) in c direction for each layer (Ca-Ca) in experimental Ruddlesden Popper structure.

3.2.2 Binding Energy of Ruddlesden Popper Layered Materials

Part of the motivation of the chapter was to look at how these structures were formed, particularly with why $n = 1-3$ can be formed via conventional synthesis methods and $n > 4$ needs to be formed via PLD. The binding energy per atom for each layered structure across all calculation methods was investigated. This was calculcated by taking the total energy of each structure and evaluating the binding energy to that of the total energy of the individual ground state structures of Ca, Mn and O. In figure 3.31 is shown the binding energy per atom for the 1×1×1 and 2×2×1 unit-cells. The binding energy decreases as n increases with the difference in binding energy to $(n-1)$ reducing. Yan et al [48] stated that the $n = 4$ RP manganate $Ca_5Mn_4O_{13}$ is inaccessible in bulk, as classical high-temparature synthesis affords phase separation into $Ca_4Mn_3O_{10}$ ($n = 3$) and $CaMnO_3$ ($n = \infty$). Figure 3.31 shows the $CaMnO_3$ orthorhombic with a 1×1×1 unit-cell having a binding energy per atom close to that of the $n = 3$ 1×1×1 unit-cell. As the orthorhombic phase of $CaMnO_3$ is a four formula unit-cell it compares to the 2×2×1 unit-cell of the $n = 1-5$ structures. This is evident 2×2×1 unit-cell calculation binding energy per atom value converging to the 1×1×1 orthorhombic $CaMnO_3$ structure.

As the Binding Energy per atom converges to the $n = \infty$ structure as n increases we have a smaller difference between that of the binding energy per atom at $n+1$ and $n-1$. By this happening it becomes more difficult to create a structure with only one value of n prevalent throughout the compound. Therefore as we increase n we are going to achieve mixed phase compounds as seen when trying to form the $n = 4$ RP structure.

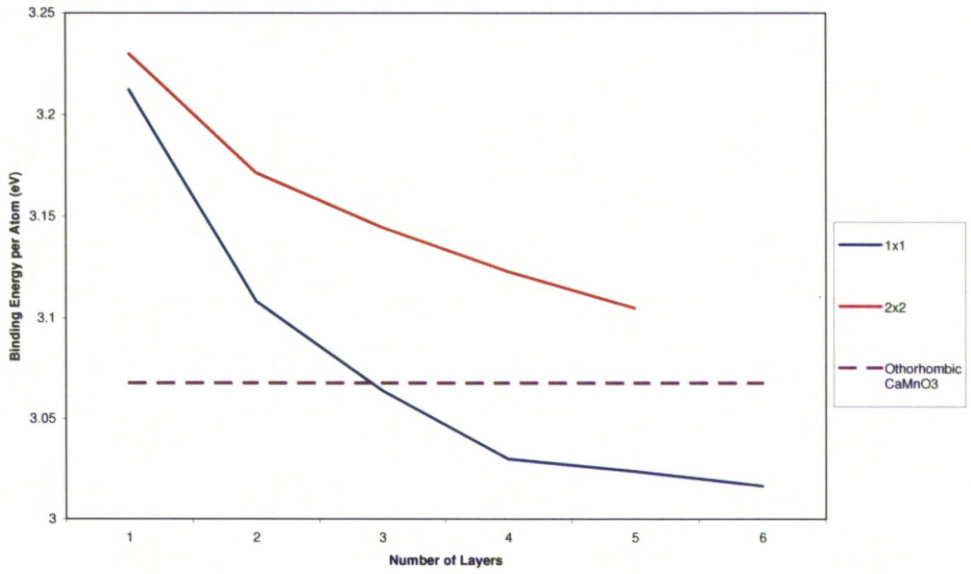

Figure 3.31: Binding Energy (eV) per atom for 1×1×1 and 2×2×1 Ruddlesden Popper structures.

3.3 Conclusion

In this chapter further justification has been obtained to back up the experimental observations of energetics and the development of the crystal structure as the number of layers is increased. There is good agreement with the dimensions of the unit-cells particularly noting the reduction in c/n as we increase n. The increase in octahedra and perovskite distortion as we increase n particularly for the 2×2×1 unit-cell for both GGA and GGA+U calculations further illustrates that the orthorhombic $CaMnO_3$ is the preferred structure for $CaMnO_3$, as previously known.

By introducing doping into the RP material or by influencing the lattice by growing on a substrate the distortion in perovskite layers can be reduced hence enabling higher values of n to be formed.

Addressing the issue of the need for PLD for $n > 4$ the convergence of the binding energy per ion to the orthorhombic $CaMnO_3$ creates energetic similarities between $n > 4$. This means that when using conventional synthesis methods to create higher n we could see multiple phases of the structures present since the binding energies are close. This occurred in experiment when $n = 3$ and the $n = \infty$ orthorhombic phases were formed when trying to form a $n = 4$ structure.

Chapter 4

Chiral II-VI semiconductor nanostructure superlattices based on an amino acid ligand

4.1 Introduction

Nanostructured objects based on II-VI binary chalcogenides such as CdS or ZnS are widely studied for their applications in semiconductor systems including diodes, transistors, or photovoltaic devices [55]. The development of nanostructures of those materials allows tuning the electronic and optical properties of such systems via the control of their dimensions [56]. The optical properties differ in relation to the bandwidth as it is reduced with respect to the bulk. This is due to the reduced dimensions of the inorganic substructure, and results in an increase of the observed band gap. The aim of the present work was to generate purely molecule-based Metal-Sulphide (M-S) arrays formed by sulphur-containing ligands with structural relationships to fragments of the bulk II-VI semiconductors. According to the Cambridge Databank, several coordination polymers involving polymeric M-S substructures based on thiolate ligands have been described with M = Cd [57–65], but only a few with M = Zn [66; 67]. Natural amino acids have recently been shown to be useful ligands for the construction of metal-organic frameworks [68–74], and investigations into the coordination potential of L-cysteinate with metal salts under solvothermal conditions have been performed

in the experimental group at the University of Liverpool. The theoretical results of two three-dimensional chiral materials Cd(L-cysteinate) **1** and Zn(L-cysteinate) **2** are discussed in this chapter. The single polydentate cysteine ligand bearing a thiolate function affords two-atom thick one-dimensional fragments of the high pressure rock salt phase of CdS (in **1**) and the ambient pressure würtzite phase of ZnS (in **2**). Electronic structure calculations show that these extended molecular systems retain the characteristics of the electronic structure of the corresponding bulk sulphide phases.

4.1.1 Setup of Calculations

Calculations were performed in two parts. Initially, structures were optimised using the plane-wave basis set DFT electronic structure program VASP (v4.6.26) [34]. For the calculations reported here the Generalised Gradient Approximation of Perdew and Wang (GGA-PW91) [22] was used for geometry optimisation with atoms represented by the projector augmented wave (PAW) [75] potentials with a plane-wave cut-off energy of 500eV for all systems. In the case of **1**, the atoms were first relaxed before relaxing the cell parameters whereas for bulk würtzite CdS, **2** and ZnS both relaxations were performed simultaneously. Since the rock-salt CdS was a high pressure phase lattice parameters were kept constant with the atoms being relaxed. For the optimisation a Monkhurst-Pack k-point mesh of 3×3×3 was used for each structure with a different k-point mesh for each DOS hybrid calculation which will be covered later in the chapter. DFT is known to underestimate band gaps and hence another suitable method was sought to provide a more accurate answer. Hence, Hybrid Hartree-Fock plus Density Functional Theory functionals were used to evaluate the density of states of the optimised structures (see Chapter 2).

4.2 Results and Discussion

4.2.1 Crystal Structure

In this sub-section the Crystal Structure of two three-dimensional (3D) chiral materials Cd(L-cysteinate) **1** and Zn(L-cysteinate) **2** will be described whilst drawing comparisons to the rocksalt and würtzite CdS structures and the ZnS würtzite structure. A discussion into how the experimental and theoretically optimised structures compare is also considered here. Figure 4.1 illustrates L-cysteinate.

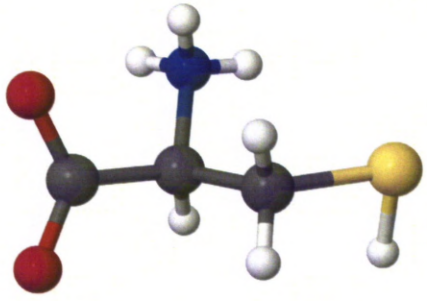

Figure 4.1: L-cysteinate

Cd(L-cysteinate) and CdS

White crystals of Cd(L-cysteinate) **1** crystallizes in a solvothermal reaction in the chiral primitive orthorhombic space group $P2_12_12_1$ with lattice parameters of a) 5.6307Å, b) 9.4827Å, c) 9.5418Å. The structure is built from a 1D ladder arrangement of cadmium and sulphur atoms arising from the bridging of Cd centres by the thiol moiety of cysteine. These 1D units are held together in a regular fashion via the carboxylate function of cysteine which binds to Cd centres of two neighbouring ladders via its two oxygens. The coordination sphere of cadmium is a distorted octahedron, with one L-cysteinate ligand acting as a tridentate capping ligand in a fac fashion via its amine, carboxylate, and thiolate groups. The bite angles of cysteinate are O2-Cd1a-N1 68.00°, O2-Cd1a-S1a 79.80°, and N1-Cd1a-S1a 72.63°. The bond lengths to the three donor atoms from the

chelating ligand are Cd1a-N1 2.32Å, Cd1a-O2 2.46Å, and Cd1a-S1a 2.95Å (Figure 4.2a, Tables A.1, A.2).

When **1** was optimised using the methods in 4.1.1 this resulted in lattice parameters of a) 5.7588Å, b) 9.6376Å, c) 9.8895Å which are a 2.28%, 1.63%, 3.64% enlargement on those derived from experiment. The bite angles of the theoretically optimised cysteinate are O2-Cd1a-N1 68.84°, O2-Cd1a-S1a 77.84°, and N1-Cd1a-S1a 71.16°. The bond lengths to the three donor atoms from the chelating ligand are Cd1a-N1 2.38Å, Cd1a-O2 2.47Å, and Cd1a-S1a 3.06Å (Figure 4.2b). An overview comparison of the 3D experimental and theoretical structures can be seen in Figure 4.3

The Hydrogen bonds in the structure differ the most when comparing bond lengths between the experimental and optimised structures. This is because when a H atom bonds with another atom, the single electron from the H atom is used in bond formation which reduces the electron density concentration around the H nucleus. The experimental structure was determined by X-ray diffraction (XRD) which locates regions of electron density. Hence this method determines the positions of the nuclei from the position of the electrons. The H nucleus cannot normally be directly located, but the electron density associated with the H bond with another atom can be found and allows the H bond distance to be estimated. As shown by the bond length comparisons in A.1 the H bond distance found by XRD is shorter than the actual value [76]. Therefore from herein H bond and associated angles will not be discussed.

During the continuing discussion of the crystal structure, bond and angle measurements will be given as (experiment) [theoretically optimised]. The coordination sphere is completed by two sulphur atoms from cysteine ligands which chelate two neighboring Cd centres in the chain and one oxygen atom from the carboxylate of a cysteine forming a neighboring chain. As a result, the three sulphur atoms at a Cd centre are arranged in a mer fashion and the two oxygen atoms are cis. (Figure 4.2a) [Figure 4.2b]. Each sulphur atom connects three Cd centres in a T-shape pattern, and each Cd centre is bound to three S atoms in a mer fashion: thus, considering only Cd-S bonds, cadmium also displays T-shape coordination. As a consequence, the bonding motif creates a ladder shaped Cd-S substructure along the *a* axis, with Cd and S atoms alternating as the three-connected nodes

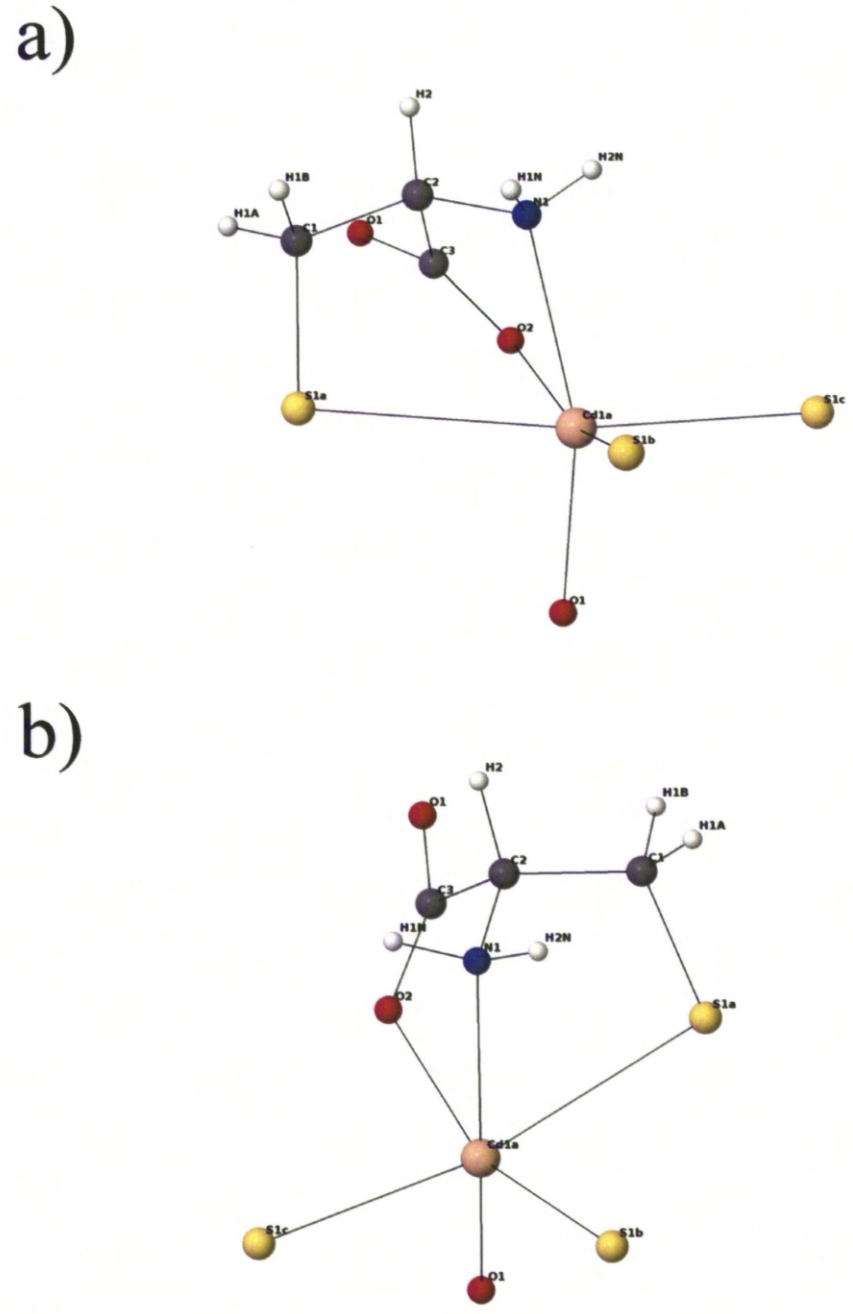

Figure 4.2: a) Coordination sphere of Cd in for experimentally derived **1**. b) Coordination sphere of Cd in for theoretically optimised derived **1**. **1**. Cd: beige; S: yellow; C: grey; O; red; N: dark blue; H: white.

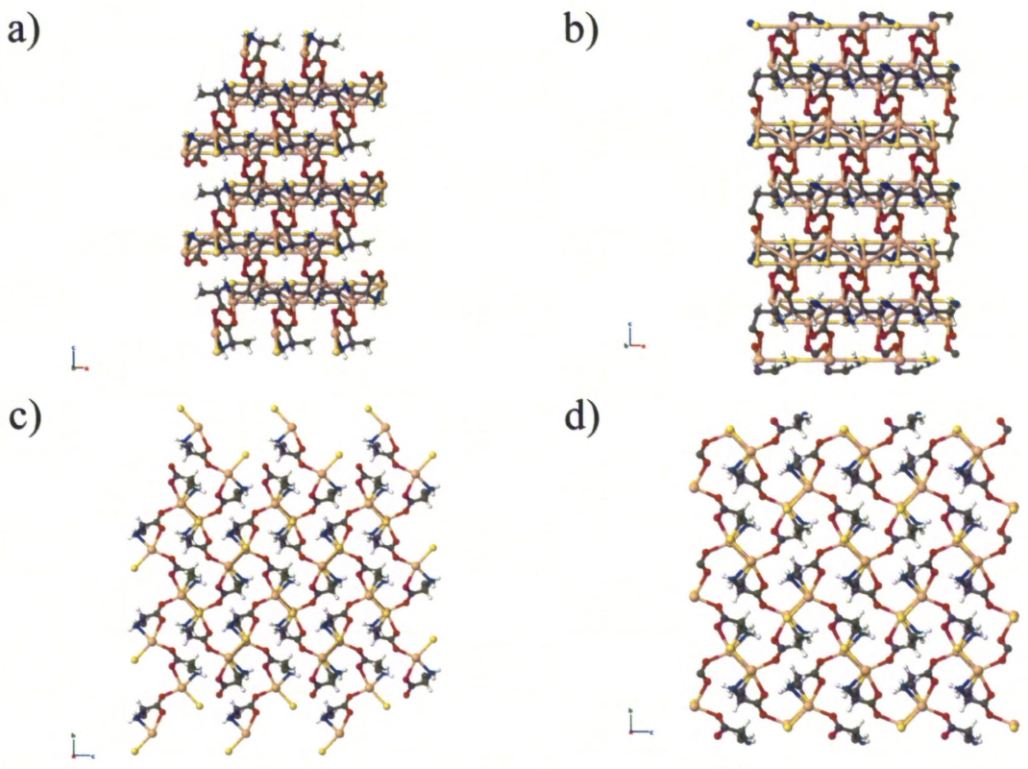

Figure 4.3: a) View of the 3D structure in the (a,c) from experiment. b) View of the 3D optimised structure in the (a,c). c) View of the 3D structure in the (b,c) from experiment. d) View of the 3D structure in the (b,c) from experiment. Cd: beige; S: yellow; C: grey; O; red; N: dark blue; H: white.

of the ladder. The Cd1a-S1b bond corresponding to the step of the ladder is the shortest with a length of (2.60Å) [2.63Å]. Two different bond lengths occur along the axis of the ladder. The chelate Cd1a-S1a bond (2.95Å) [3.06Å] is long but within an acceptable bonding range when compared to other thiolate-based cadmium coordination polymers, [58; 77; 78] whereas the Cd1a-S1c contact bridging the Cd (L-cysteinate) moieties along the *a* axis is shorter (2.71Å) [2.72Å].

The 1D CdS ladder substructure is almost planar as the Cd1a-S1c-Cd1c angle is (168.71° Figure 4.4a) [169.50° Figure 4.5a]. It forms by edge-sharing of neighbouring Cd octahedra. Two adjacent S-S edges connect one Cd to its two neighbours, generating a 1D arrangement (Figure 4.6b), which is a restricted fragment of the rock salt structure, in which all octahedral edges are shared. The large S donor atom can play this edge-bridging role unlike the smaller first row donor atoms.

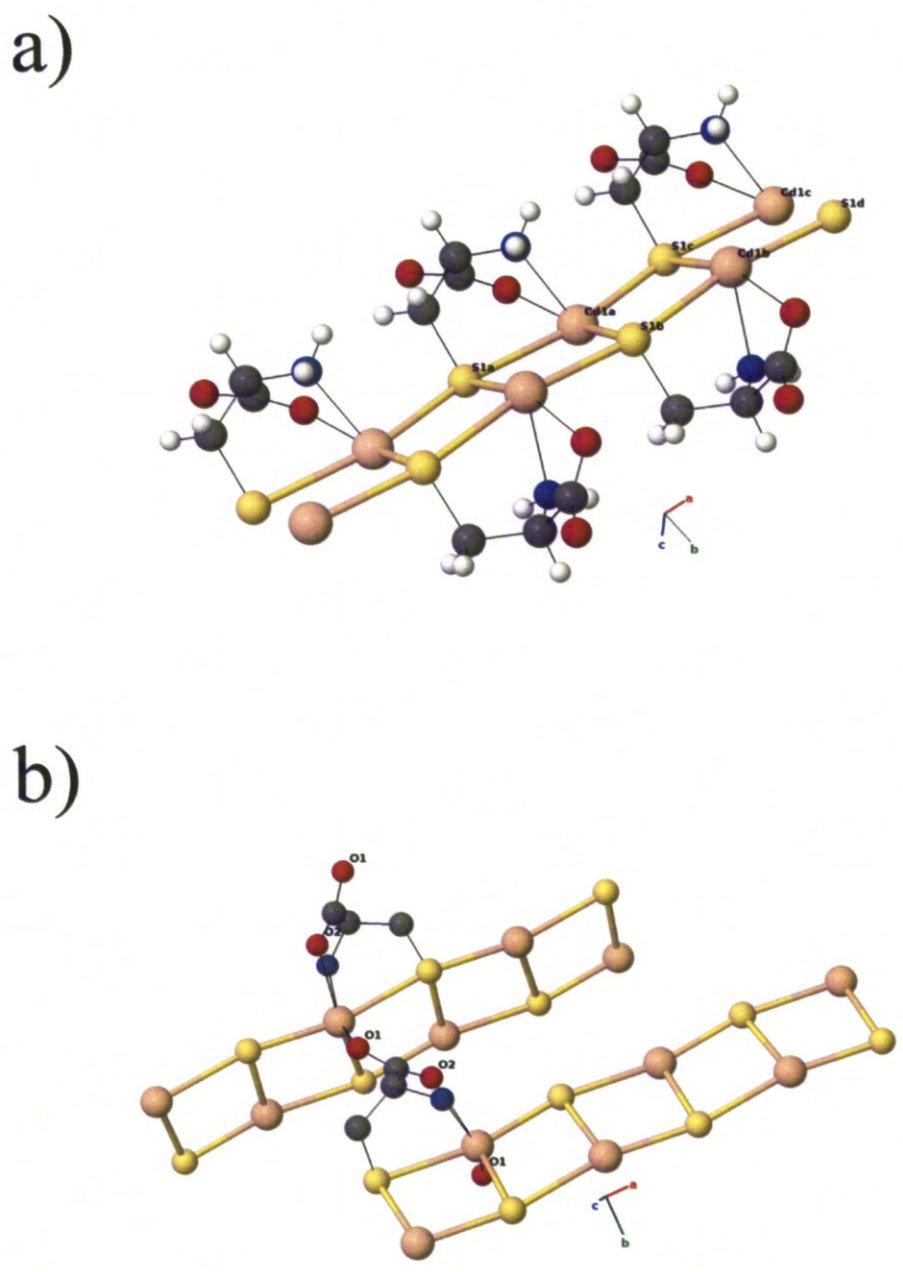

Figure 4.4: All structures shown in this figure are deduced from experimental data. a) The Cd-S ladder substructure which is the fundamental structural unit of **1** (in green). This corresponds to the 2_1 screw axis along a. The Cd1b-S1c-Cd1a angles are 87.88° and the S1c-Cd1a-S1b angles are 97.32°. b) View of two neighbouring ladders in **1** linked by the carboxylate function of cysteine. Cd: beige; S: yellow; C: grey; O; red; N: dark blue; H: white.

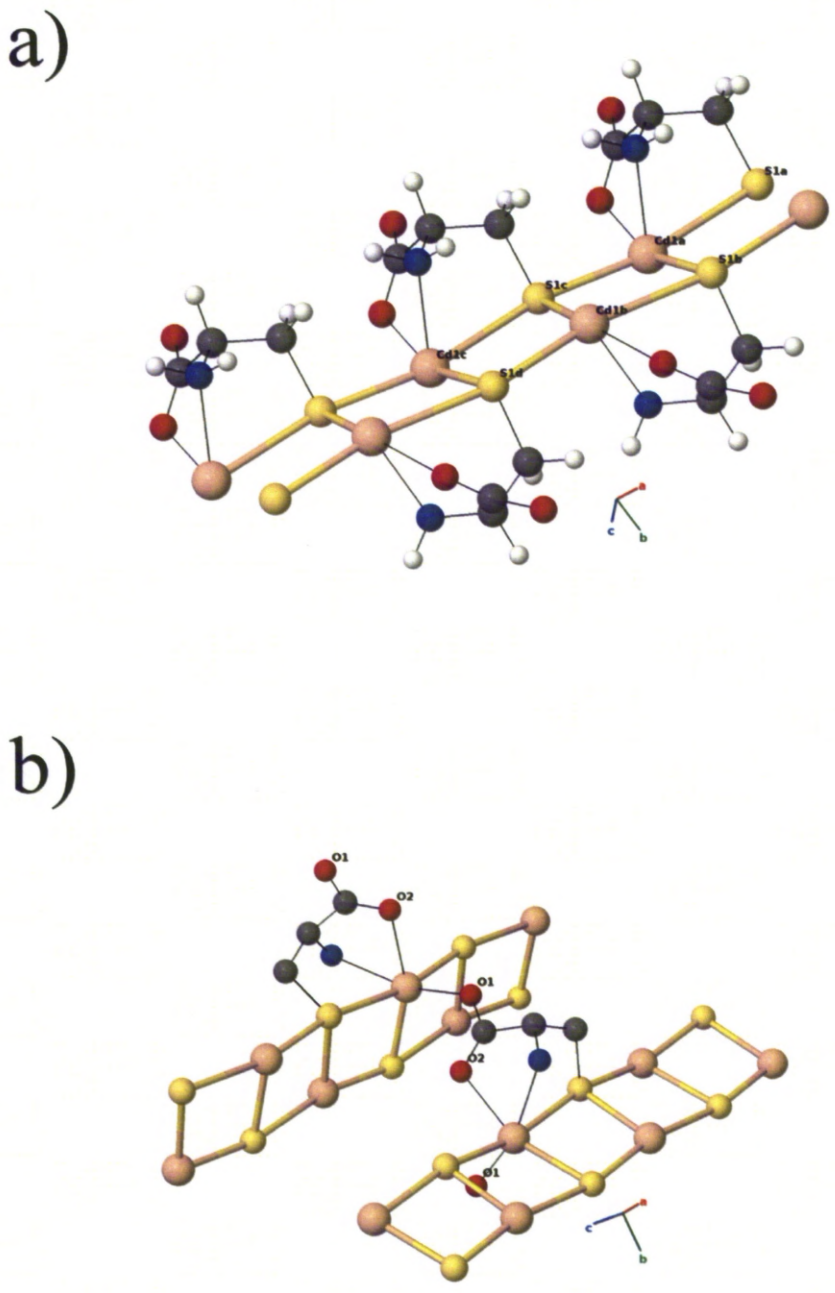

Figure 4.5: All structures shown in this figure are deduced from theoretically optimised data. a) The Cd-S ladder substructure which is the fundamental structural unit of **1** (in green). This corresponds to the 2_1 screw axis along a. The Cd1b-S1c-Cd1a angles are 90.03° and the S1c-Cd1a-S1b angles are 97.35°. b) View of two neighbouring ladders in **1** linked by the carboxylate function of cysteine. Cd: beige; S: yellow; C: grey; O; red; N: dark blue; H: white.

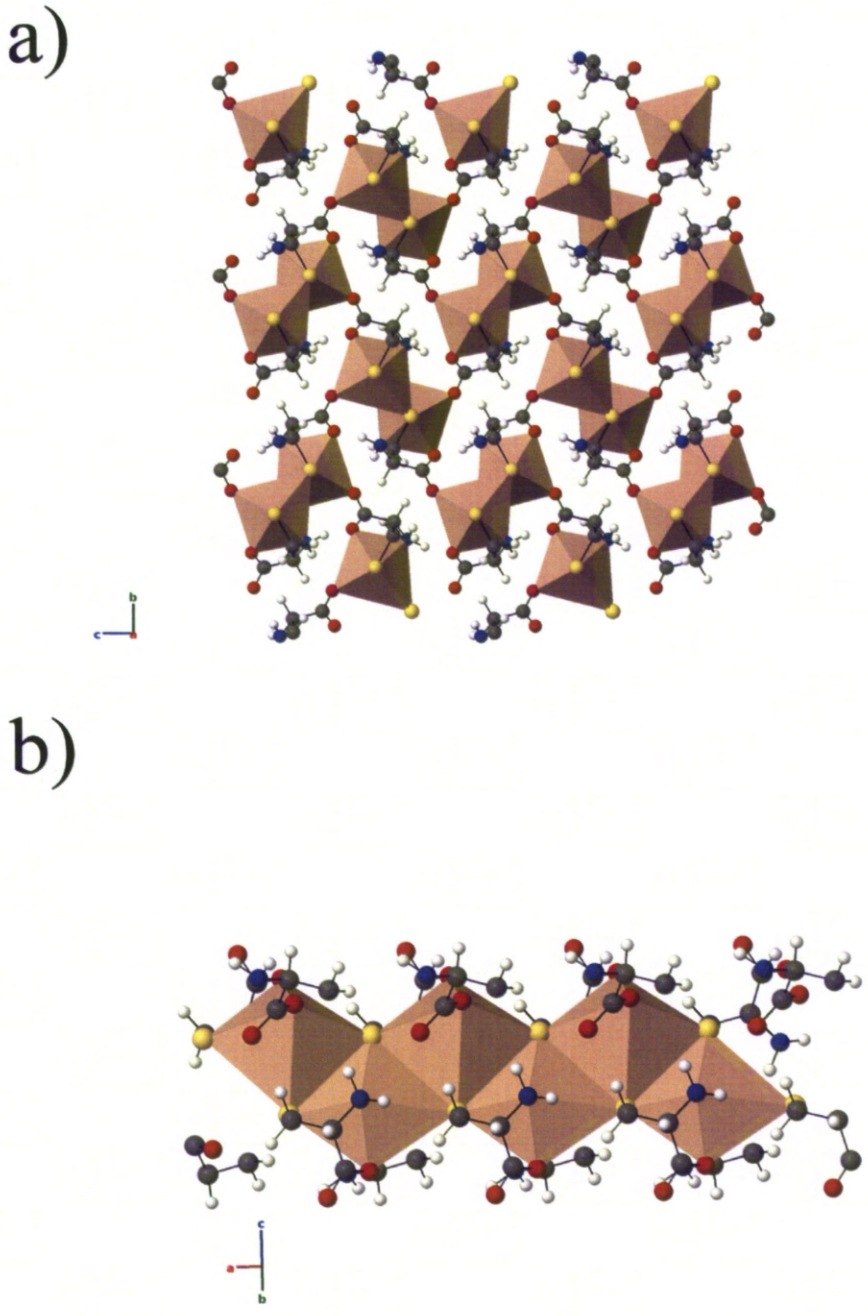

Figure 4.6: a) View of the 3D structure of **1** in the (b,c) plane. All ladders (polyhedral representation) are oriented along the *a* axis and share no edges or corners with each other. Octahedra are centred on Cd atoms. b) Polyhedral representation of a single ladder, showing that each Cd centre shares two cis edges with its two CdL_6 neighbours, forming a 1D arrangement. Octahedra are centred on Cd atoms; Cd: beige ; S: yellow; C: grey; O; red; N: dark blue; H: white.

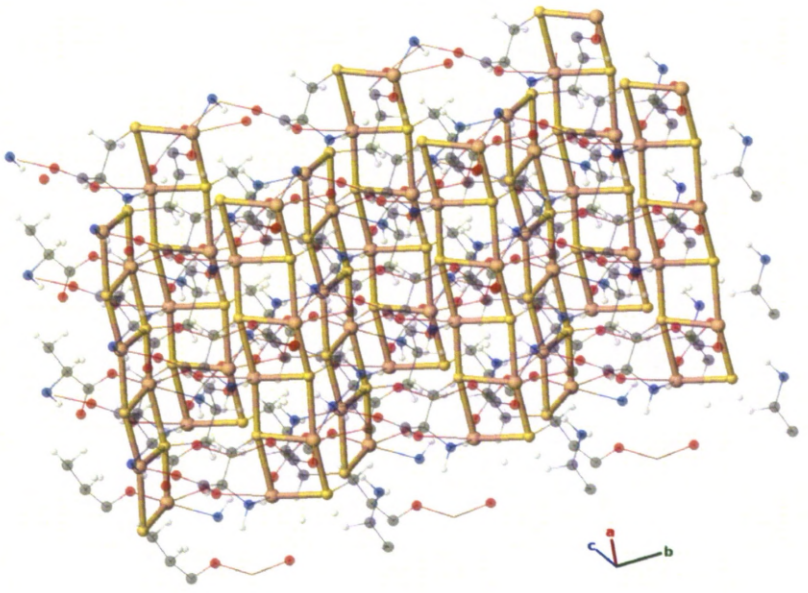

Figure 4.7: View displaying the arrangement of ladders along a in **1**. The amino acid backbone is made translucent for clarity. Cd-S bonds generate ladders and are highlighted in bold beige / yellow. The structure shown is that of the theoretically optimised which has an angle of 86.28° between neighbouring ladders. Cd: beige ; S: yellow; C: grey; O; red; N: dark blue; H: white.

The nitrogen atom (N1) and one of the oxygen atoms of the carboxylate function (O2 cis to N1) of cysteine are both monodentate to Cd. The last site in the cadmium coordination sphere (trans to N1) is occupied by the O1 oxygen atom of a carboxylate belonging to a neighbouring ladder. These three atoms prevent any further edge-sharing for the Cd octahedron and thus prevent the substructure from extending in the (b,c) plane (Figure 4.6a). The ladders mutually saturate the coordination sphere of their constituent metal centres by connecting to each other via bridging carboxylates. Each ladder acts as a ligand (via its O1 atoms) toward two of its neighboring ladders (Figure 4.6a). As O1 and O2 are cis to each other, a carboxylate group forms a Cd-O2 chelate bond with one ladder that lies almost in

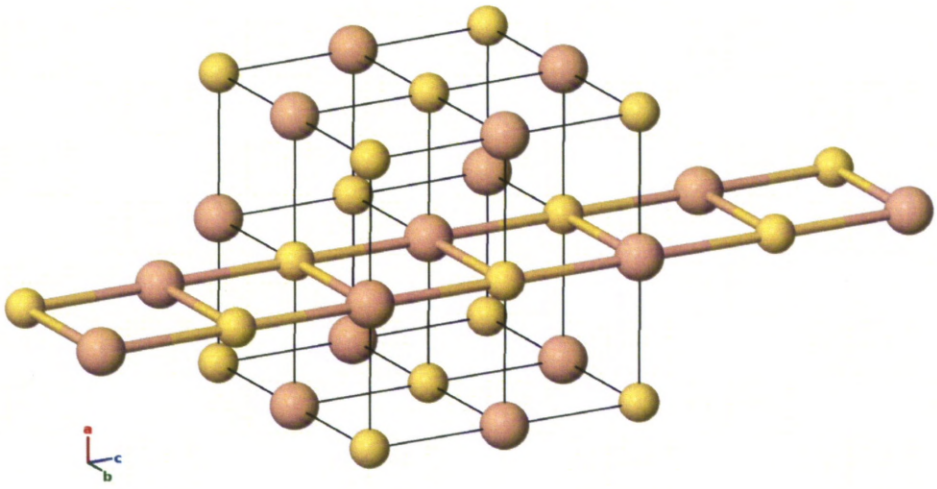

Figure 4.8: View of the structure of the high pressure (40 kbar) rock salt phase of cadmium sulphide. A fragment of the bulk that compares to the CdS ladder substructure of **1** is highlighted with thick bonds. Cd: beige; S: yellow

the mean plane of the CdS ladder substructure and a Cd-O1 bridging bond with a second ladder that is forced to be almost perpendicular to the mean plane of that second CdS substructure, (Figure 4.4b) [Figure 4.5b]. As a consequence, two neighboring 1D CdS substructures form an angle of (94.15°) [86.28°](Figure 4.4b) [Figures 4.5b and 4.7]. The Cd coordination sphere is very distorted as this second oxygen generates angles of O1-Cd1a-N1 (154.87°) [153.04°] and O1-Cd1a-S1b (109.23°) [110.22] (Figure 4.2).

The array of Cd-S bonds which form the core structural feature of **1** can be related to the structures of both the ambient and high pressure forms of bulk CdS. The ladder-shaped CdS array in **1** is a fragment present in the high pressure rock salt CdS phase (Figure 4.8). The Cd1b-S1c-Cd1a (87.88°) [90.03°] and S1c-Cd1a-S1b (97.32°) [97.35°] angles are close to 90 found in the bulk phase. With the

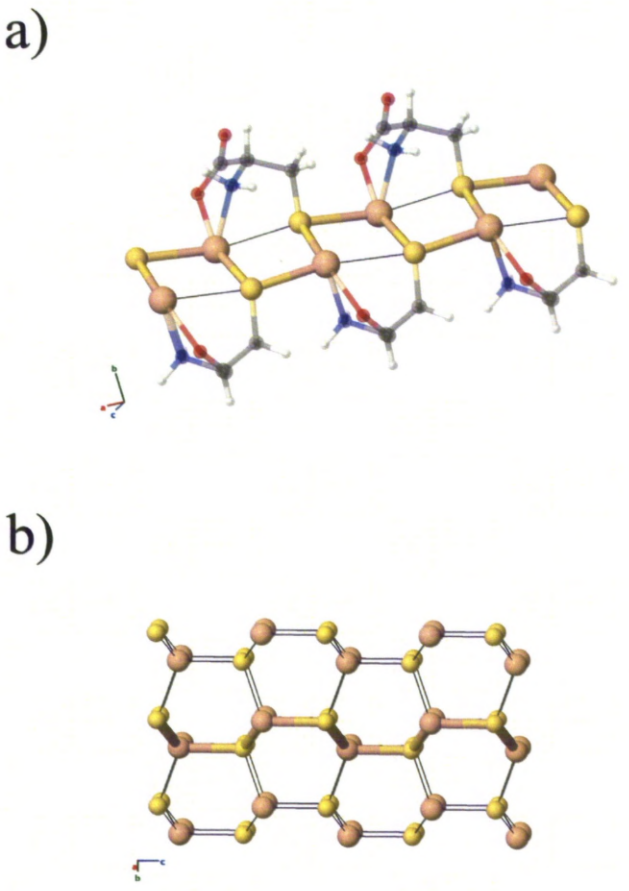

Figure 4.9: a) View of the structure of **1** to show the relationship of the CdS array to the ambient pressure würtzite polymorph of CdS. The 1D CdS substructure is represented with thick bonds. The thing black bonds correspond to the long Cd-S chelate bond. b) View of the structure of bulk CdS würtzite with a 1D fragment illustrated with thick bonds comparable to the substructure in **1** Cd: beige ; S: yellow; C: grey; O; red; N: dark blue; H: white.

lattice parameters fixed to simulate the high pressure in the CdS bulk phase when optimised the atoms did not move when evaluating the structure with VASP as expected. The mean Cd-S bond length (2.75Å) [2.80Å] is also close to the rock salt value of 2.72Å (at 40 kbar). The length difference between the bonds oriented along the *a* axis ((2.95Å) [3.06Å] for the chelate bond Cd1a-S1a, (2.71Å) [2.72Å] for the bridging bond S1c-Cd1a, (Figure 4.4a) [Figure 4.5a]) indicates a certain degree of distortion. If Cd1a-S1a is not considered as forming part of the Cd coordination sphere, the CdS substructure appears as a zigzag chain compressed along the *a* axis. This is a highly distorted fragment of the würtzite structure of CdS (Figure 4.9). The bond lengths in this bulk phase are significantly shorter (2.526Å and 2.532Å) [2.58Å and 2.56Å], and cadmium is only four coordinate in würtzite CdS, making the high pressure CdS phase analogy more appropriate for **1** where the Cd coordination number is six. The higher coordination number at ambient pressure in **1** compared to CdS can be understood as favored by the smaller size of the first row N and O ligands also involved in bonding to Cd in **1**, compared to the CdS phases where S is the only ligand. The CdS substructures in **1** are thus best described as slightly distorted 1D fragments of the high pressure phase (rock salt) of CdS. It is worth noting that this mer arrangement of three S ligands is rare in cadmium compounds, as the corresponding CdS bulk phase is not stable at ambient pressure. Most cadmium sulphide [79; 80](or cadmium thiolate [57–65]) systems display a würtzite-like connectivity. The fact that the Cd1a-S1a bond (2.95Å) [3.06Å] is the longest of all the Cd-S bonds in **1** suggests that the presence of S1a in the coordination sphere of Cd1a is only maintained because of the chelate effect. If the thiol group was not connected to the rest of the amino acid backbone, relaxation along the *a* axis could occur to allow the 1D CdS substructure to adopt a more favorable würtzite-like arrangement (Figure 4.9). The specific rock salt 1D CdS pattern in **1**, characterized by a mer arrangement of three S ligands producing an edge-sharing chain, is thus enforced by the chelate effect of the ligand.

With regard to the CdS ambient and high pressure phase structures and the effects of optimisation on the crystal structure that of the CdS rocksalt high pressure phase as previously stated remains unchanged. This was primarily due to the restriction of the cell lattice parameters to simulate the high pressure phase. The

CdS würtzite phase saw an increase in the Cd-S bonds from 2.532Å and 2.526Å to 2.566Å and 2.577Å which consequently brought about a small enlargement of the unit cell.

Zn(L-cysteinate) and ZnS

Similarly for **2** the nomenclature for bond lengths and angles will be (experimental) [theoretically optimised] with a fuller discussion comparing the two structures after a description of the crystal structure.

White crystals of **2** are grown from solvothermal reactions and crystallizes in the chiral space group $P2_12_12_1$ (a) 6.025Å, b) 8.830Å, c) 9.460Å) [a) 6.337Å, b) 9.814Å, c) 10.166Å]. As a result of the theoretical optimisation there is a 5.18%, 11.14% and 7.46% increase in the lattice parameters in the a, b and c axes respectively. This large change upon optimisation will be discussed later.

The major structural difference from **1** stems from the reduced coordination number of the smaller Zn, which is four coordinate in a tetrahedral environment in **2**. This changes the nature of the 1D ZnS structural subunit formed by L-cysteine, which in **2** is only bidentate via the N and S atoms toward one Zn centre (Figure 4.10a) [Figure 4.10b]. The extended structural unit defining **2** is a zigzag alternating Zn-S chain, where the second S in the Zn coordination sphere is generated by the bridging thiolate function of a cysteinate that is bidentate to the neighbouring Zn in the chain (Figure 4.11a) [Figure 4.12a]. In contrast to **1**, the carboxylate group does not bind to the Zn atom locked into this chain subunit by the S and N functions, and thus cysteine is not involved in the tridentate chelate binding mode. Instead, the carboxylate group is oriented outward away from the chain and binds in a monodentate fashion to a second Zn centre in a neighboring chain. The Zn (N, O, 2S) tetrahedral environment is thus defined by bidentate (N,S) and bridging S from two cysteine ligands defining the chain and O from the carboxylate of a cysteine that defines a neighbouring chain. The resulting chain is much more regular than in **1**, with similar bond lengths for the bidentate Zn1a-S1a (2.37Å) [2.37Å] and the bridging Zn1a-S1b (2.36Å) [2.35Å] bonds (Figure 4.11a, Table B.1) [Figure 4.12a]. The Zn1a-S1b-Zn1b angle is (92.47°) [100.73°] and the S1a-Zn1a-S1b angle (124.61°) [125.37°]. The distorted Zn tetrahedra (Table B.2)

a)

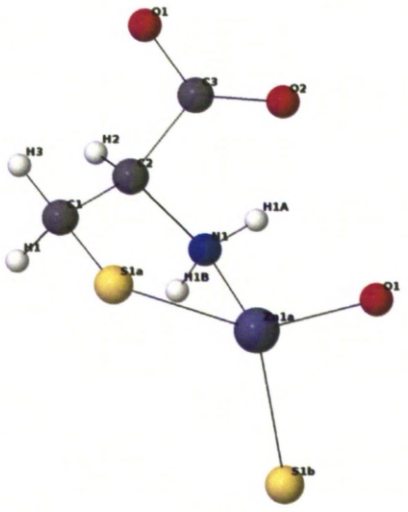

b)

Figure 4.10: a) Coordination sphere of experimentally derived Zn in **2**. b)Coordination sphere of theoretically optimised derived Zn in **2** Zn: Grey / Blue; S: yellow; C: grey; O; red; N: dark blue; H: white.

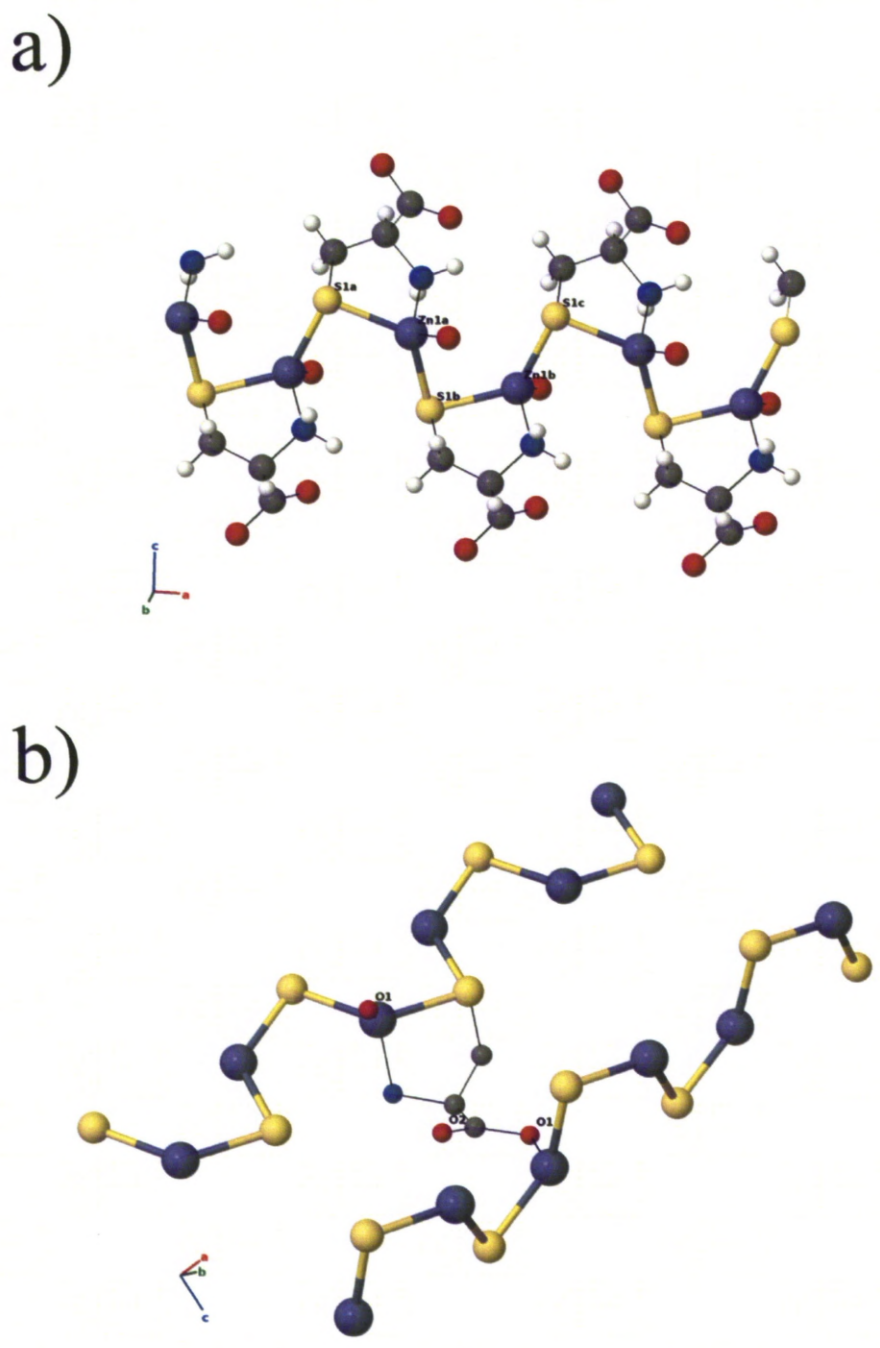

Figure 4.11: All structures shown in this figure are deduced from experimental data. a) Zig-zag 1D Zn-S substructure in **2**; b) Two neighbouring chains are bridged by the carboxylate function; the mean planes of the two chains are at an angle of 89.21°. Zn: Grey / Blue; S: yellow; C: grey; O; red; N: dark blue; H: white.

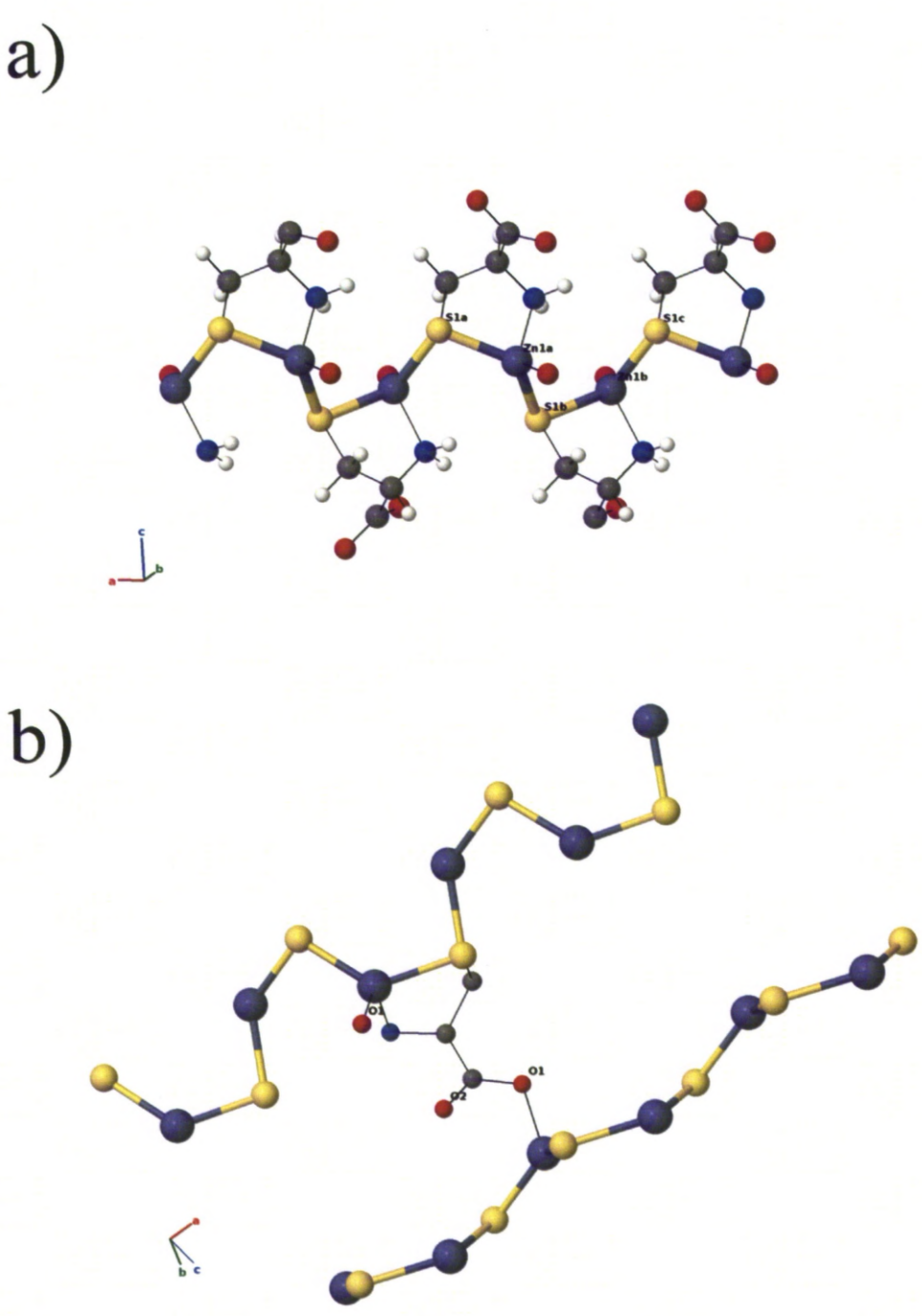

Figure 4.12: All structures shown in this figure are deduced from theoretically optimised data. a) Zig-zag 1D Zn-S substructure in **2**; b) Two neighbouring chains are bridged by the carboxylate function; the mean planes of the two chains are at an angle of 73.12°. Zn: Grey / Blue; S: yellow; C: grey; O; red; N: dark blue; H: white.

a)

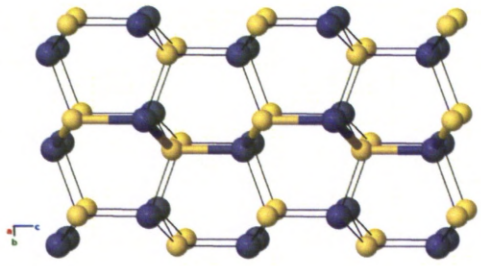

b)

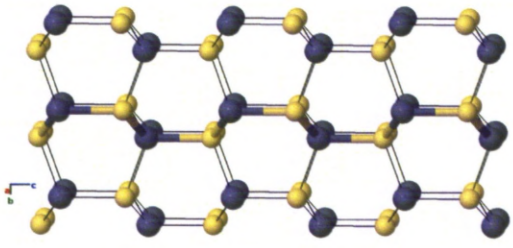

Figure 4.13: All structures shown in this figure are deduced from experimental data. a) View of the structure of the experimentally derived würtzite phase of bulk ZnS. A comparable fragment to the ZnS chain substructure in **2** is highlighted with thick bonds. b) View of the structure of the theoretically optimised derived würtzite phase of bulk ZnS. A comparable fragment to the ZnS chain substructure in **2** is highlighted with thick bonds. Zn: Grey / Blue; S: yellow; C: grey; O; red; N: dark blue; H: white.

are linked into chains by sharing S atom corners. The other two corners of the tetrahedron are locked by N and O atoms, which limits the dimensionality to 1D. As in **1**, the chains mutually saturate the coordination sphere of their Zn centres by connecting to one another via the carboxylate functions (Figure 4.14a) [Figure 4.14c], but in **2** the carboxylates solely bind to chains not formed by their parent cysteine molecule. The arrangement of neighbouring chains relative to the original one corresponds to the 2_1 screw axes along b and c. As in **1**, all chains are thus aligned along the a axis with angles of (89.21°) [73.12°] between neighboring chains (Figure 4.11b) [Figure 4.12b]. In **2**, the substructure is close to a distorted ZnS würtzite structure with angles along the chains of (92.47°) [100.73°] (Zn1a-S1b-Zn1b) and (124.61°) [125.37°] (S1a-Zn1a-S1b), while the corresponding angle is 109.51 in the würtzite bulk structure (Figure 4.11a and 4.13a) [Figure 4.12a and 4.13b]. Zn-S bond lengths of (2.36Å) [2.35Å] and (2.37Å) [2.37Å] in **2** are extremely close to the bulk values (2.34Å and 2.35Å) [2.37Å and 2.36Å]. Zn also remains four coordinate, as in the bulk structure. The zigzag ZnS chain can be viewed as a distorted 1D fragment of the bulk würtzite structure. The non-bonding Zn-S contact Zn1a-S1c (3.84Å) [4.23Å] is significantly longer than the Zn-S bonds. The carboxylates are bidentate in **1** and are only monodentate in **2**, further decreasing the coordination number of the metal by one unit, accounting for the octahedron-based geometry of **1** and the tetrahedron-based geometry of **2**.

In the case of **2**, the DFT optimised structure differs too strongly from the crystal structure to be considered a reliable model of **2**. Cell parameters change from $a = 6.025$Å, $b = 8.830$Å, $c = 9.460$Å to $a = 6.337$Å, $b = 9.814$Å, $c = 10.166$Å, showing a significant increase in b and c. The coordination number, the first coordination sphere of Zn and the connectivity of L-cysteine remain similar, with acceptable bond lengths and angles in comparison with the experimentally determined structure (Tables B.1 and B.2). However, the DFT-derived structure is less compact than the actual structure of **2** as shown in the comparison of the experimentally and theoretically derived structures in figure 4.15. In particular, the ZnS substructure is affected: the non bonding Zn-S contact along the a axis is extended by 10.15% and the folding angle of the chain along a increases by 8.93%. This problem did not occur in **1**, owing to the tridentate and bridging coordina-

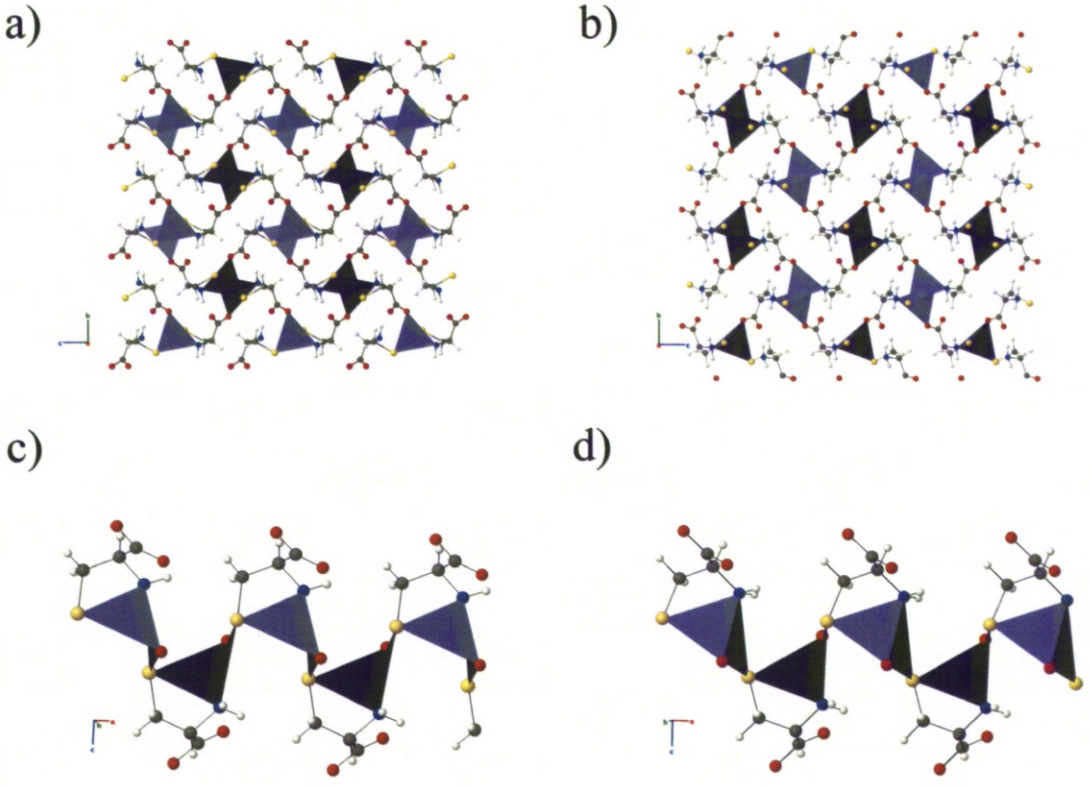

Figure 4.14: a) View of the 3D structure of the experimentally derived **2** in the (b,c) plane. The pendant carboxylates connect one chain to its four neighbours. b) View of the 3D structure of the theoretically optimised derived **2** in the (b,c) plane. c) Tetrahedral representation of a chain (experimental structure), showing that the 1D ZnS substructure is generated by corner-sharing tetrahedra. d) Tetrahedral representation of a chain (theoretically optimised structure); Zn: grey/blue; S: yellow; C: grey; O; red; N: dark blue; H: white.

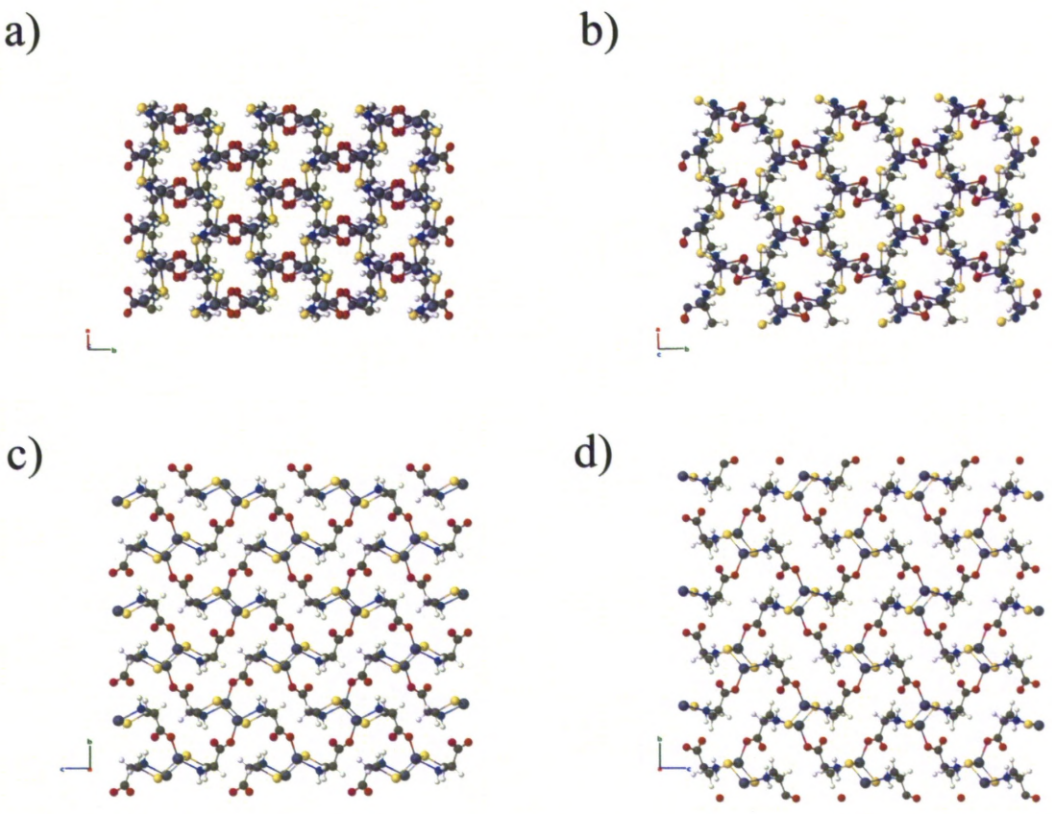

Figure 4.15: a) View of the 3D structure in the (a,b) from experiment. b) View of the 3D optimised structure in the (a,b). c) View of the 3D structure in the (b,c) from experiment. d) View of the 3D structure in the (b,c) from experiment. Zn: Grey / Blue; S: yellow; C: grey; O; red; N: dark blue; H: white.

tion of cysteine that generate a constrained structure with denser packing. In **1**, no significant difference from the experimental structure is observed in the Cd-S bonds (less than 3.73% difference). In **2**, cysteine is only bidentate and gives the framework much more flexibility, as evidenced by the increase of the non bonding Zn1a-S1c contact from 3.84Å to 4.23Å (Figure 4.15). This can explain the expansion of the cell volume that is observed during optimisation, and also suggests that the isolated phase of **2** might be a metastable phase of Zn(L-cysteinate). It was suggested that the initial experimentally determined Zn(L-cysteinate) structure was incorrect due to the large difference in the lattice parameters but was deemed not to be true on further inspection.

This change in structure could be due to the noted potential problem with labile

metal ions such as Cd^{2+} and Zn^{2+} [81]. These ions often do not impose as strong a preference for a given geometry compared to other ions hence making it harder to predict the structure of the network obtained. Flexibility in the bridging ligand is also a potential problem, along with, that a single metal coordination geometry can propagate into more than one type of network.

4.2.2 Density of States Calculations

Cd(L-cysteinate) and CdS

The calculated density of states for **1** (Figure 4.16) from the hybrid functional caclulations allows us to evaluate a theoretical band gap of 4.2 eV. Observation of the energies at specific k-points allowed us to determine the nature of the band gap. For **1** no single k-point was found to correspond to both the highest energy of the valence band and the lowest energy of the conduction band. This indicates that the optical band edge transition must be phonon assisted and that the gap is therefore indirect. The lowest energy of the conduction band in **1** corresponds to the k point (0.125, 0.125, 0.125), whilst the highest energy of the valence band can be found for k points (-0.375, 0.125, 0.125), (0.375, 0.125, 0.125), and (-0.375, -0.125, 0.125) [82].

The calculated value of the band gap only slightly underestimates the value obtained by experiment which was 4.29 eV for an indirect transition. The underestimation of band gaps is a known shortcoming of DFT [83] hence the use of hybrid functionals to partially correct this. This effect of DFT will be discussed in this chapter with comparison to the band gap of HSE03 Hybrid Functional.

A detailed study of the atomic parentage of the levels involved in the band edge transition in **1** reveals that the edge of the valence band (Figure 4.17) is mostly composed of p orbitals of sulphur atoms with less prominent contributions from p_O and d_{Cd}. The s orbitals of Cadmium give the main contribution to the levels on the edge of the conduction band (Figure 4.18). Figure Figures 4.17 and 4.18 are sampled at a higher rate than figure 4.16.

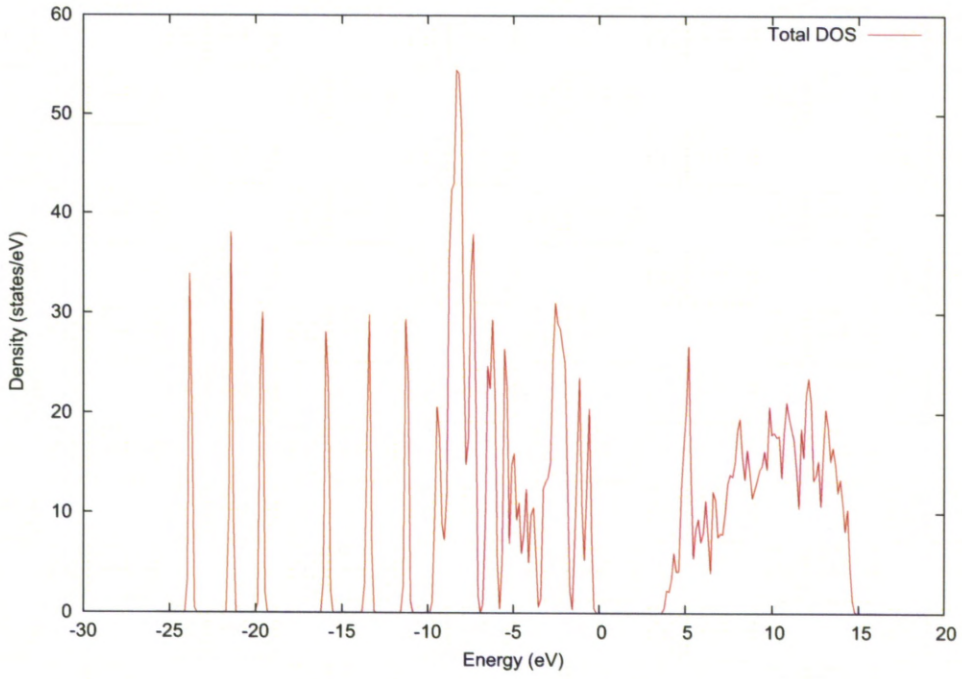

Figure 4.16: Density of States from Hybrid Calculations for **1**

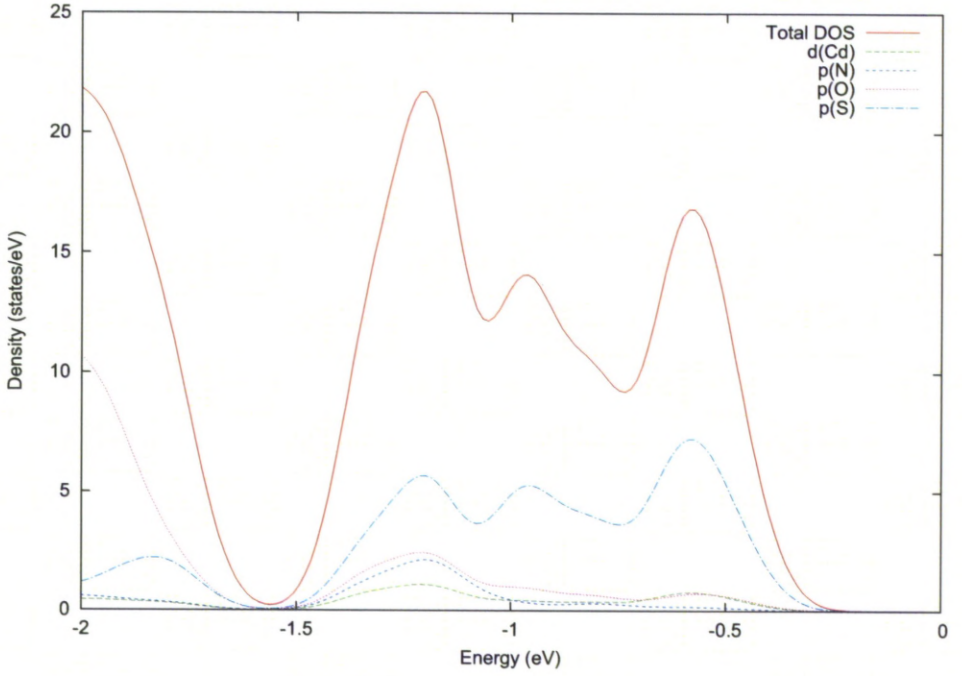

Figure 4.17: Density of States at Valence Band edge from Hybrid Calculations for **1**

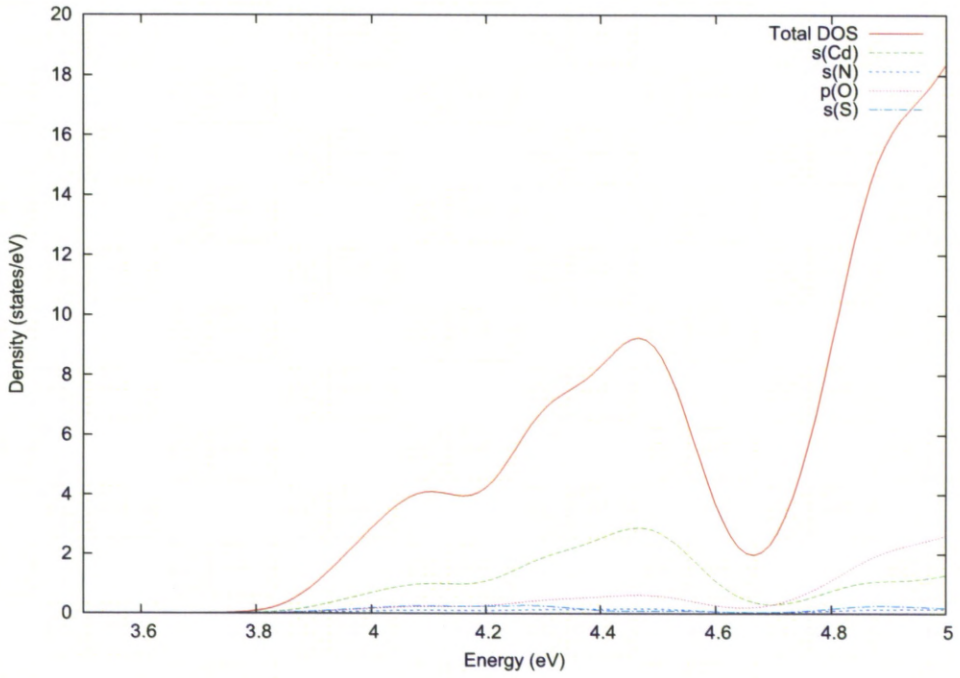

Figure 4.18: Density of States at Conduction Band edge from Hybrid Calculations for **1**

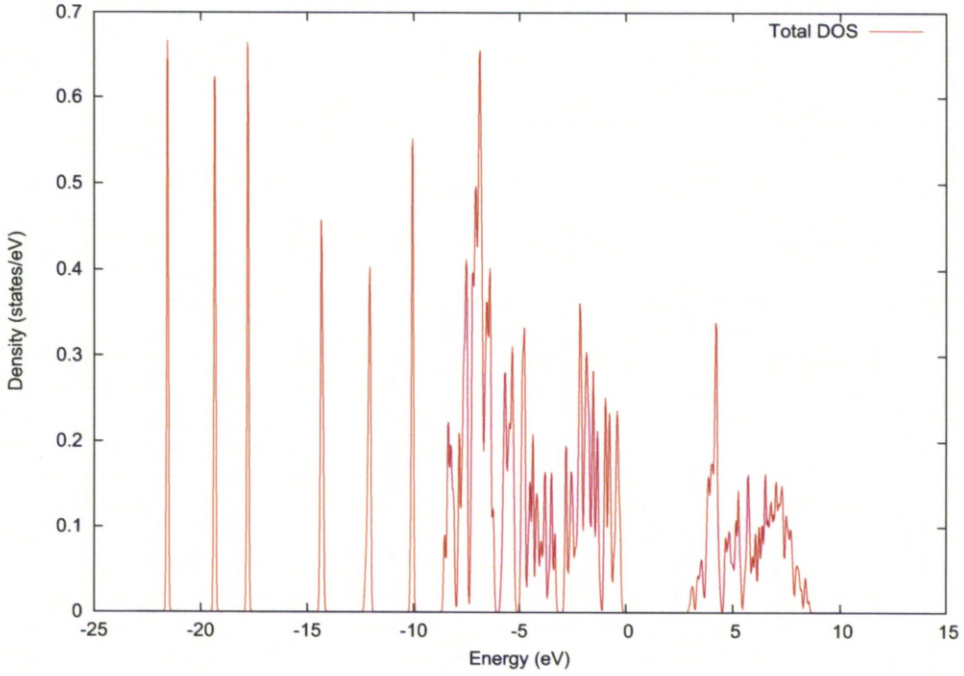

Figure 4.19: Density of States from GGA Calculations for **1**

As expected the DFT calculations underestimate the band gap with the GGA calculations showing a band gap of 3.25eV for **1** (Figure 4.19). Although, the band gap is reduced from that of the HSE03 calculations some key characteristics remain in the Density of States. The band gap is illustrated to be an indirect gap with the lowest energy of the conduction band corresponding to the k-point (0.000, 0.000, 0.000) and the highest energy in the valence band corresponding to the k-point (0.333, 0.000, 0.000).

Similarly, when studying the atomic parentage of the levels involved in the band edge transition in **1** reveals that the edge of the valence band (Figure 4.20) is mostly composed of p orbitals of sulphur atoms with less prominent contributions from p_O and d_{Cd}. The s orbitals of Cadmium give the main contribution to the levels on the edge of the conduction band (Figure 4.21).

The GGA DOS for **1** (Figure 4.19) compares favourably with the Hybrid DOS (Figure 4.16) with both showing six molecular states below -10eV and similar corresponding peaks in the bulk states albeit more compact in Figure 4.19. A closer look at the conduction band edge shows an extra peak at 3.1eV in figure 4.21 which contributes further to the reduction of the band gap in DFT.

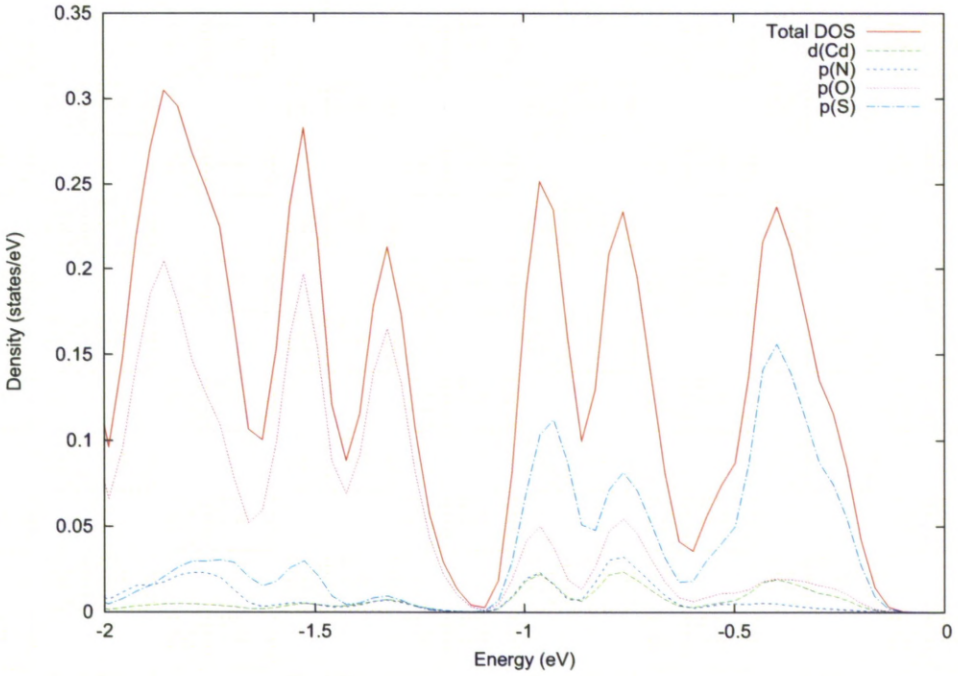

Figure 4.20: Density of States at Valence Band edge from GGA Calculations for **1**

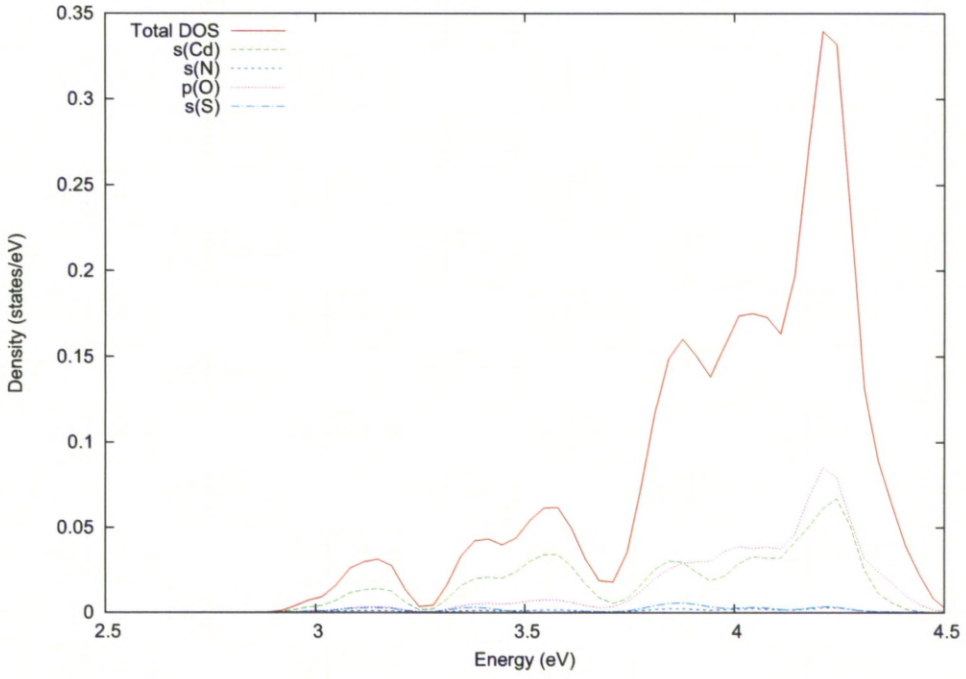

Figure 4.21: Density of States at Conduction Band edge from GGA Calculations for **1**

We also performed DOS calculations on the parent rock salt high pressure phase of CdS. In this case, due to the metastable character of the phase, lattice parameters were fixed at the experimental value of a = 5.43Å (at 40 kbar) [84]. With this restriction, the atomic positions were optimised whilst the lattice parameters were fixed at the experimental values and used as an input to calculate the DOS. The gap was found to be 1.1eV, compared to the higher experimental value of 1.7 eV. This was calculated with a k-point mesh of 10×10×10 as it was the largest mesh that could be used for the calculation with the computational facilities available. The nature of the band gap was determined to be indirect as the lowest energy of the conduction band and the highest energy of the valence band corresponded to different k-points. (0.0, 0.0, 0.0) corresponds to the lowest energy of the conduction band for the CdS rock salt, while (0.4, 0.4, 0.0) corresponds to the highest energy of the valence band.

The atomic parentage at the valence and conduction bands in **1** was also observed in bulk rock salt CdS: the main contribution to the edge of the valence band is from p_S orbitals with a smaller contribution from d_{Cd} orbitals (Figure 4.23), while the edge of the conduction band is composed essentially of s_{Cd} orbitals (Figure 4.24).

Comparing the Cd (L-cysteinate) structure to that of the bulk rock salt structure of CdS illustrate similarities in the local arrangement of the 1D CdS substructures in **1**, the indirect nature of its gap and its absence of luminescence.

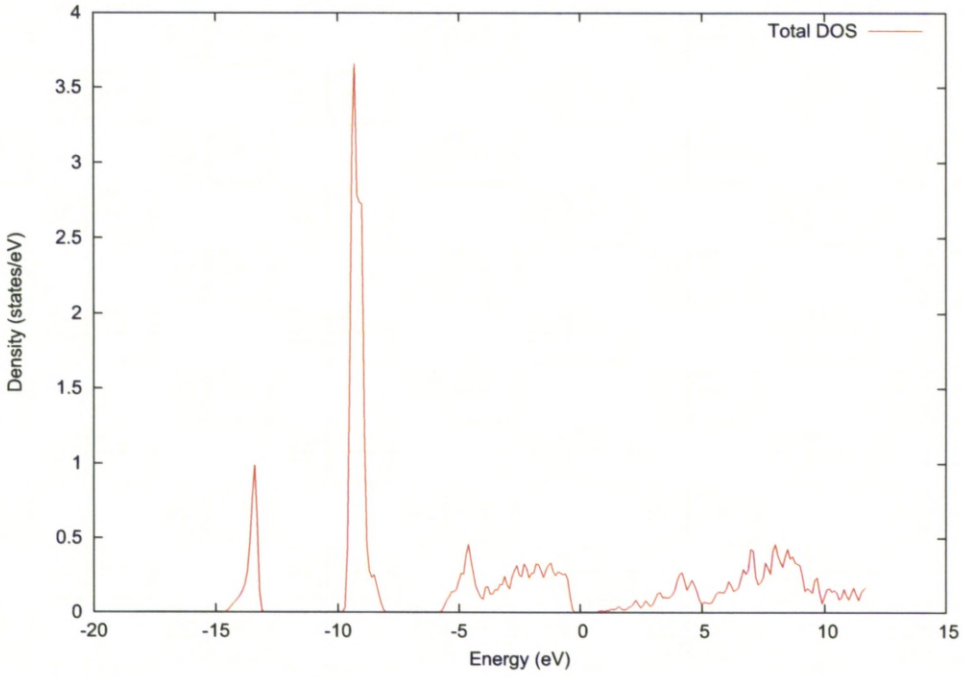

Figure 4.22: Density of States from Hybrid Calculations for CdS Rocksalt

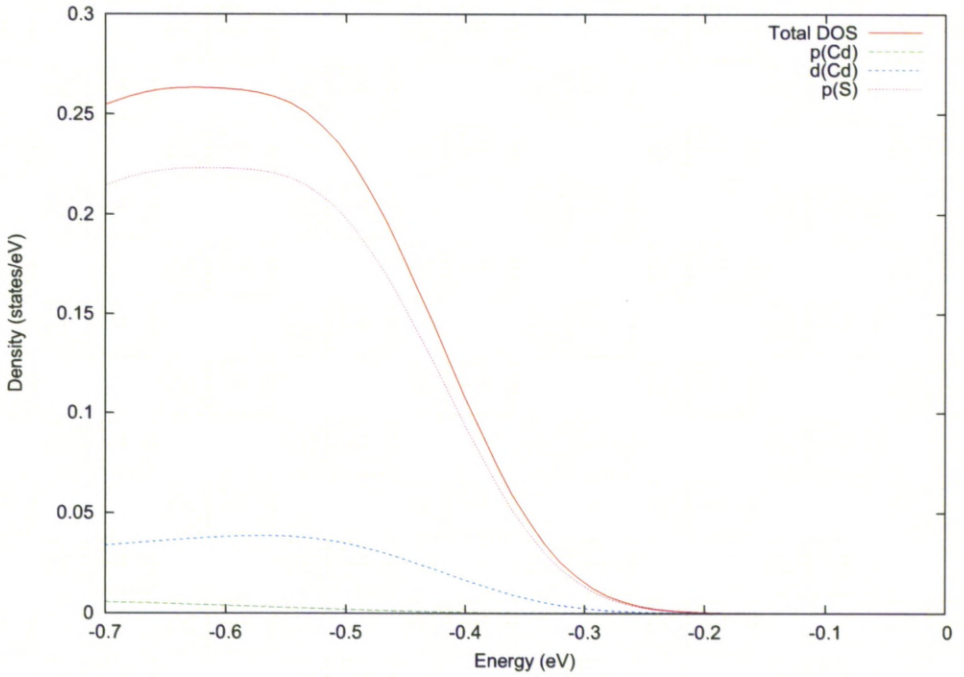

Figure 4.23: Density of States at Valence Band edge from Hybrid Calculations for CdS rocksalt

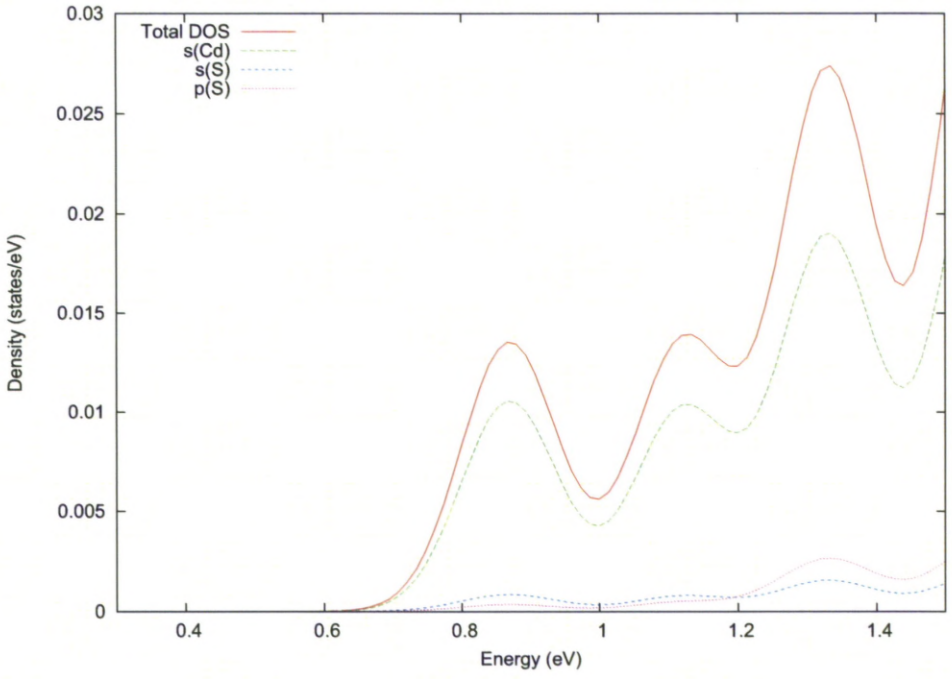

Figure 4.24: Density of States at Conduction Band edge from Hybrid Calculations for CdS rocksalt

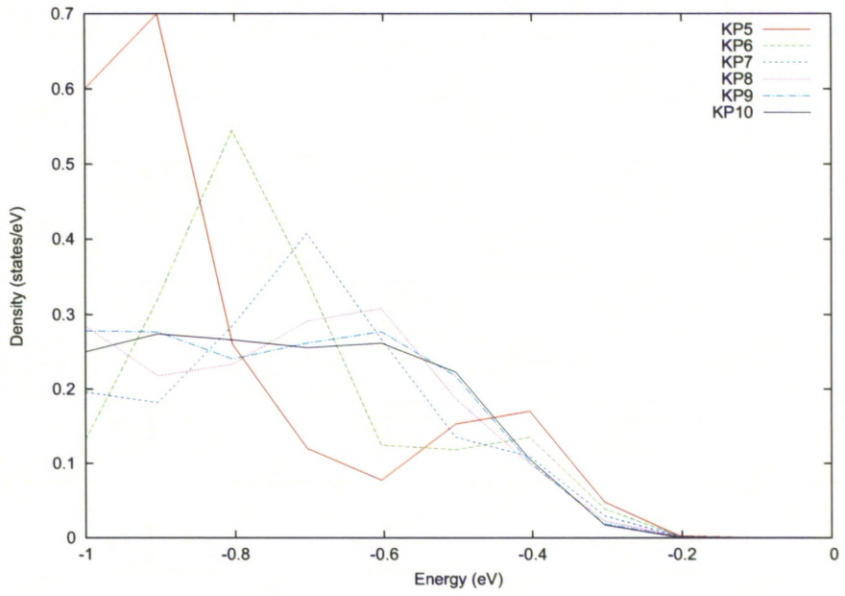

Figure 4.25: Density of States at the Valence Band edge from Hybrid Calculations for CdS Rocksalt comparing for different k-point meshes ranging from 5×5×5 to 10×10×10

The size of the k-point mesh and its effect on the DOS was evaluated for the CdS rocksalt layer to see if an improvement on the result could have been gained. The smallest k-point mesh used was 5×5×5 with the largest as illustrated above, 10×10×10. They were all evaluated over the same number of states to maintain consistency in their representation. Figure 4.25 shows the valence band edge for the differing k-point meshes with all calculations showing the density to become negligible around -0.2eV. When looking closer at the valence band edge, as would possibly be expected the density becomes negligible sooner approaching the edge as the number of k-points increases (Figure 4.26).

The influence of the size of the k-point mesh at the conduction band is illustrated in figure 4.27. We can see the band gap produced by a 5×5×5 mesh is the smallest and the initial motivation for further evaluation. Whilst not as clear as at the valence band edge, we can see a convergence of the size of the band gap with the the conduction band edge for 5×5×5 to 9×9×9 k-point meshes fluctuating either side of the larger 10×10×10 mesh with the difference between the corresponding mesh reducing. Further increasing the mesh is restricted by the expense of the hybrid calculations.

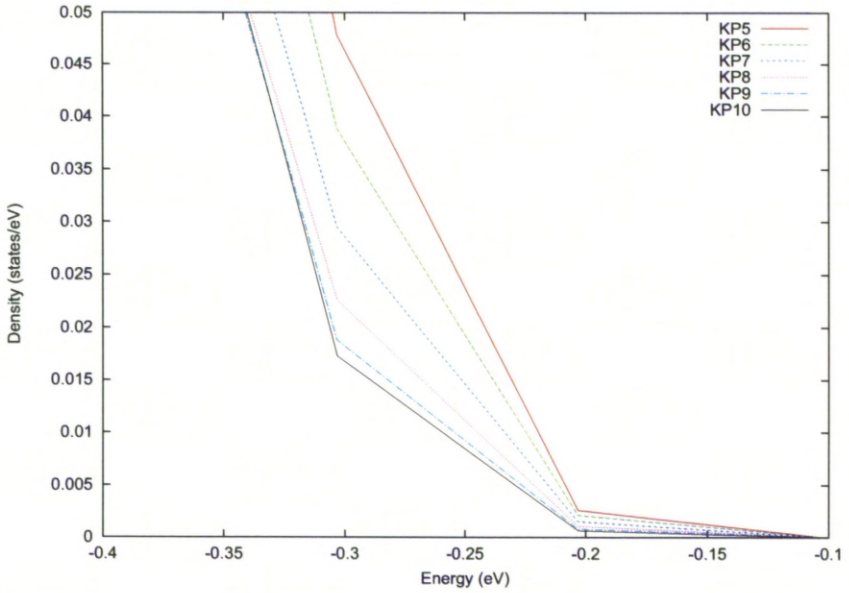

Figure 4.26: A closer look at the Density of States at the Valence Band edge from Hybrid Calculations for CdS Rocksalt comparing for different k-point meshes ranging from 5×5×5 to 10×10×10

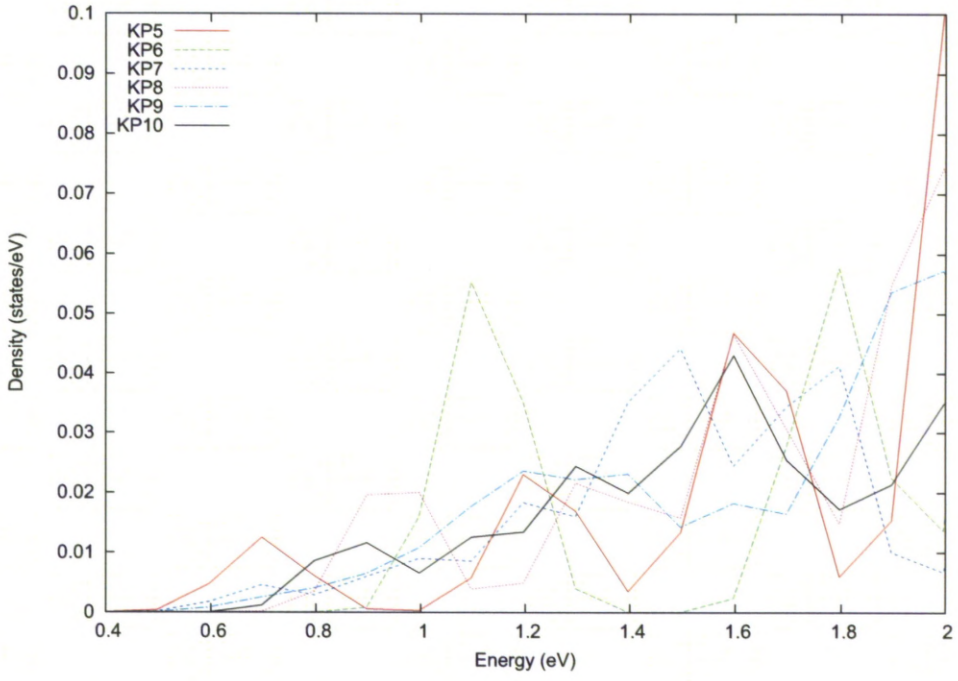

Figure 4.27: Density of States at the Conduction Band edge from Hybrid Calculations for CdS Rocksalt comparing for different k-point meshes ranging from 5×5×5 to 10×10×10

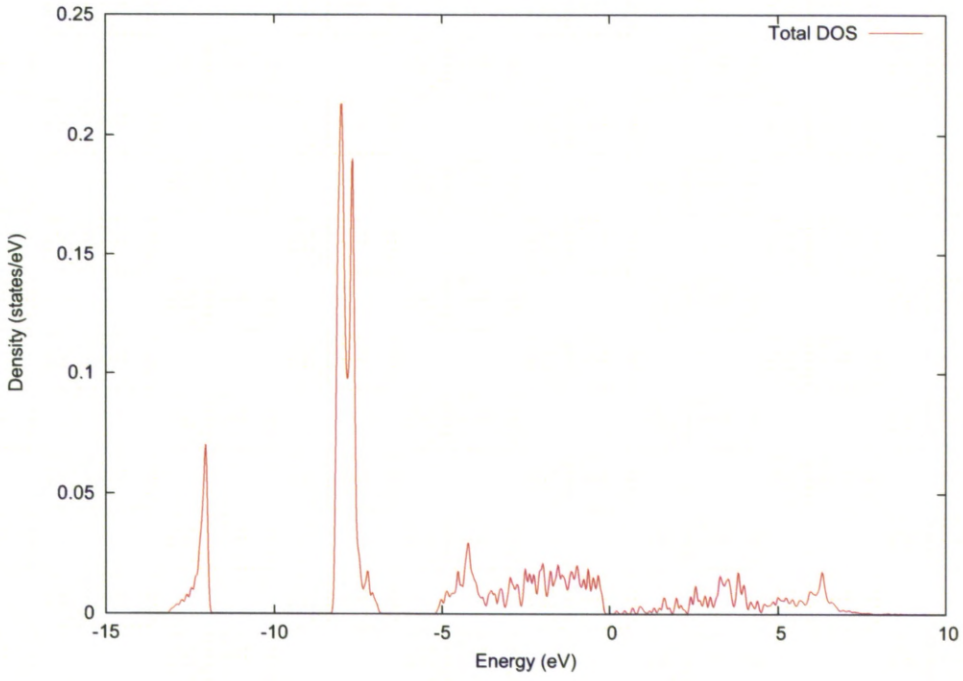

Figure 4.28: Density of States from GGA Calculations for CdS Rocksalt

From the GGA Calculations for the CdS rocksalt we obtain a band gap of 0.3eV (Figure 4.28) which is significantly lower than the experimental 1.7eV and the Hybrid 1.1eV. Despite this, as with the GGA and Hybrid calculations for **1** and the hybrid calculations for the same CdS rocksalt structure it shares the same prominences in the atomic parentage at the valence and conduction band edge. With a p_S dominance at the valence band edge (Figure 4.29) and a s_{Cd} dominance at the conduction band edge. Similarly, DFT determined the rocksalt CdS structure to have an indirect band gap.

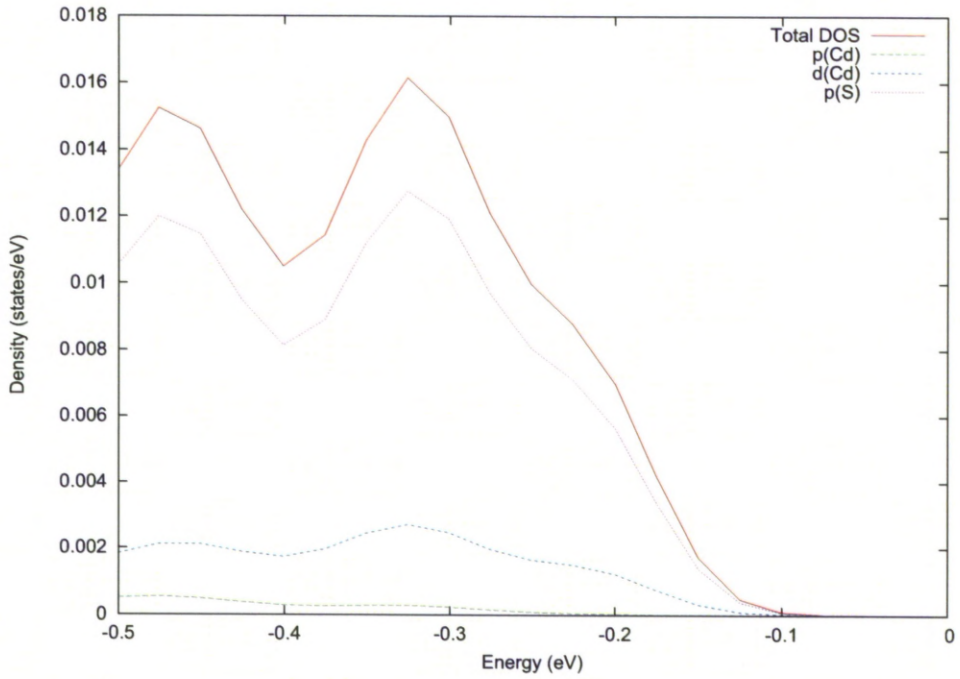

Figure 4.29: Density of States at Valence Band edge from GGA Calculations for CdS Rocksalt

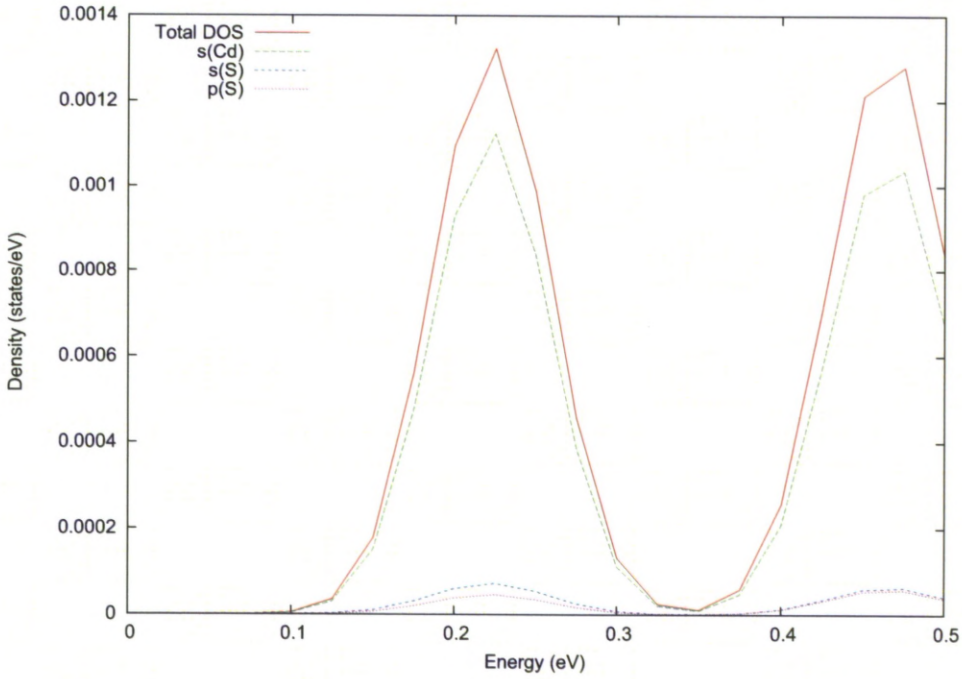

Figure 4.30: Density of States at Conduction Band edge from GGA Calculations for CdS Rocksalt

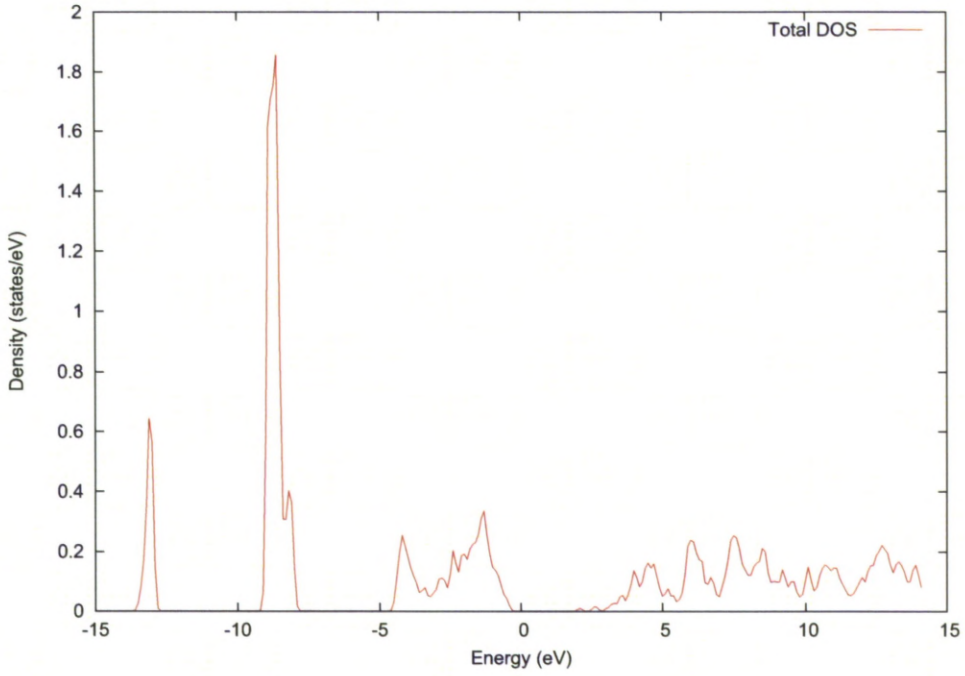

Figure 4.31: Density of States from Hybrid Calculations for CdS Würtzite

To further examine the identity of the CdS substructure we also calculated the density of states of CdS. The previously described method was used. The calculated band gap was found to be 2.35 eV (Figure 4.31), slightly higher than previously reported calculations [83], but once again smaller than the experimental value of 2.42 eV at room temperature. The lowest energy of the conduction band and the highest energy of the valence band correspond to the same k-point (-0.125, 0.125, 0.125). Hence the CdS würtzite phase is a direct gap system. This agrees with experiment. The same major contributions are observed on the edge of the gap in bulk würtzite CdS as with **1** and rocksalt CdS (Figures 4.32 4.33).

The calculations here thus agree with the experimental finding that the gap increases as the Cd coordination number decreases.

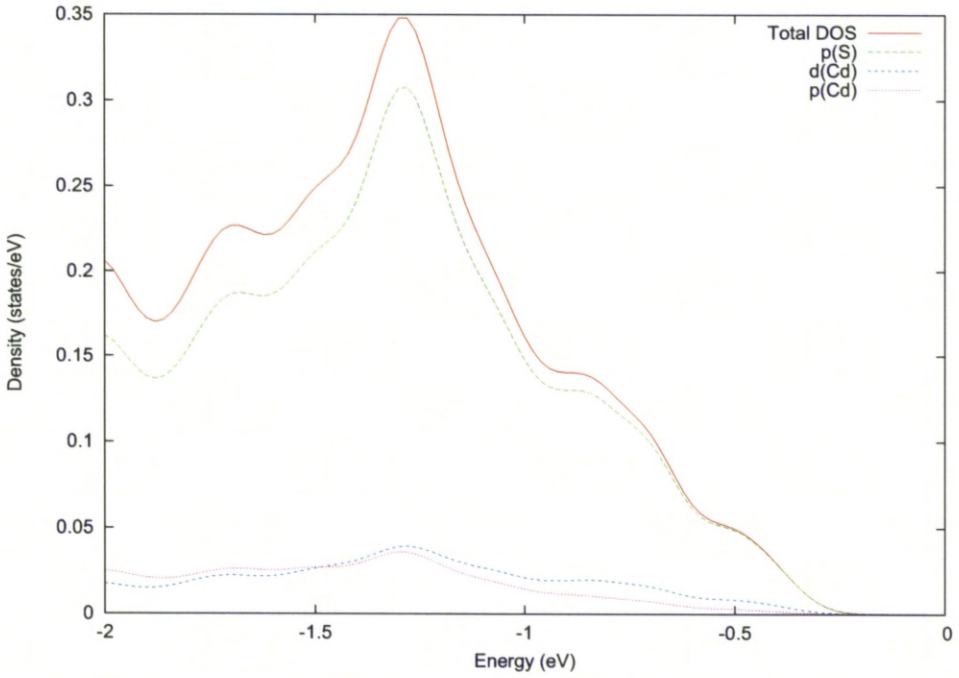

Figure 4.32: Density of States at Valence Band edge from Hybrid Calculations for CdS Würtzite

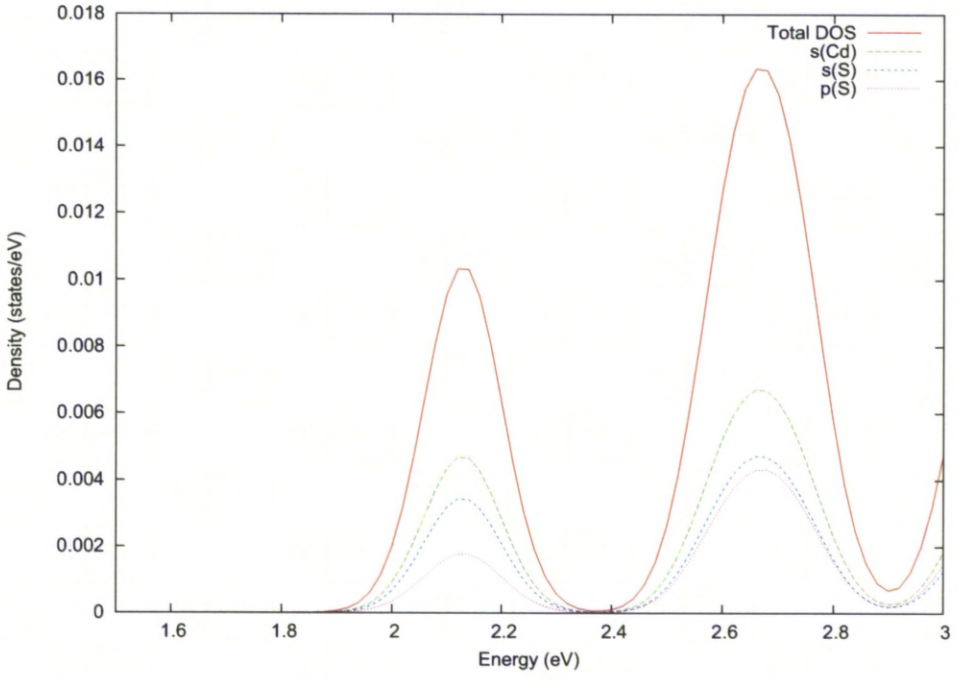

Figure 4.33: Density of States at Conduction Band edge from Hybrid Calculations for CdS Würtzite

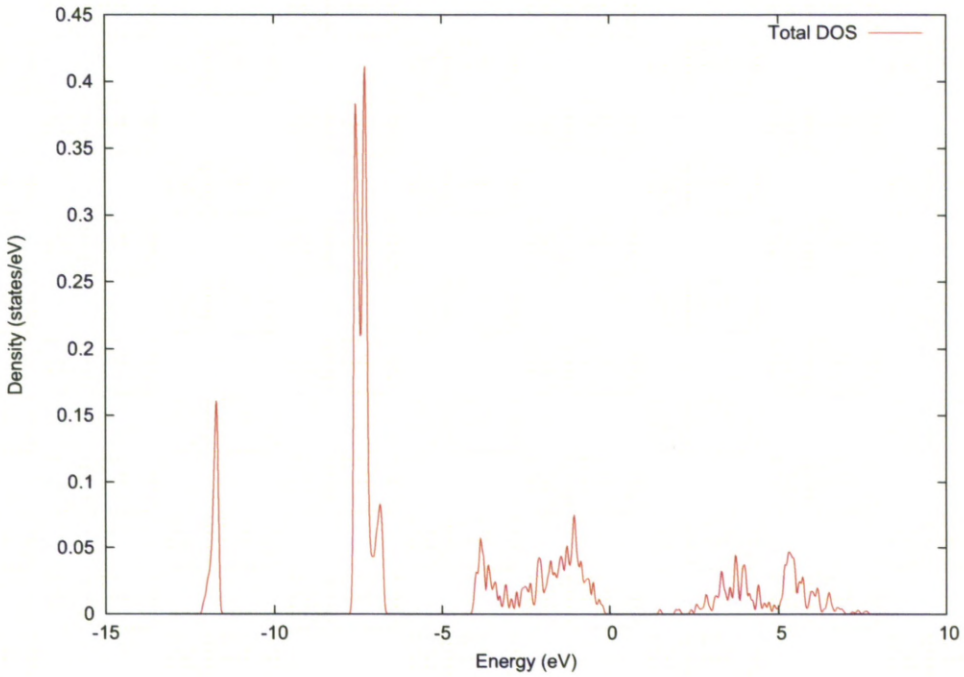

Figure 4.34: Density of States from GGA Calculations for CdS Würtzite

From the GGA Calculations for the würtzite CdS we obtain a band gap of 1.55eV (Figure 4.34). Despite this, as with the GGA and Hybrid calculations for **1** and the hybrid calculations for the same würtzite CdS structure it shares the same prominences in the atomic parentage at the valence and conduction band edge. With a p_S dominance at the valence band edge (Figure 4.35) and a s_{Cd} dominance at the conduction band edge (Figure 4.36). Similarly, DFT determined the würtzite CdS structure to have a direct band gap.

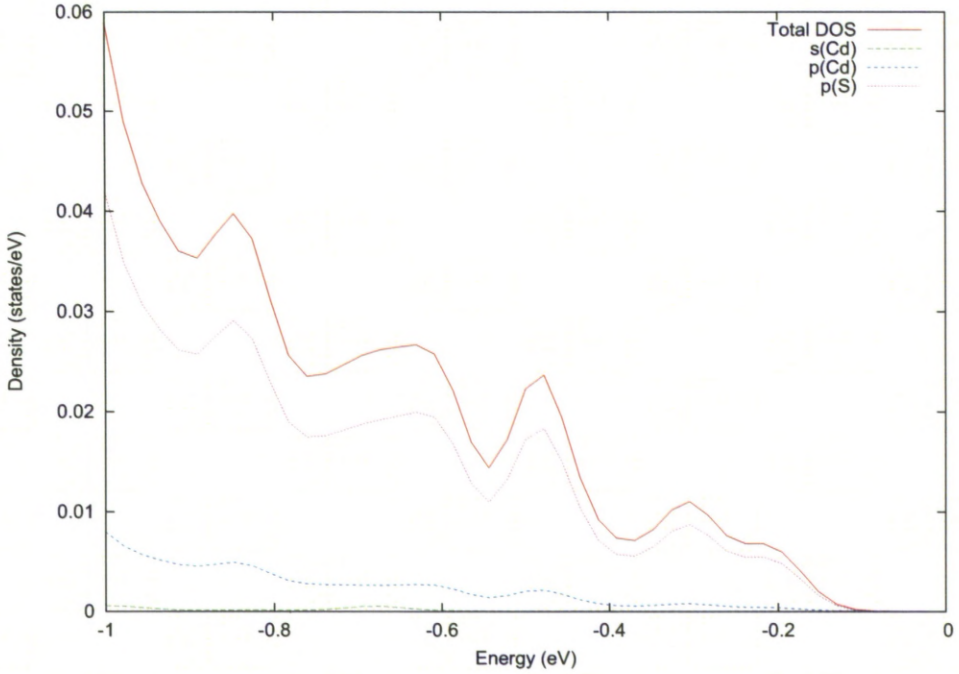

Figure 4.35: Density of States at Valence Band edge from GGA Calculations for CdS Würtzite

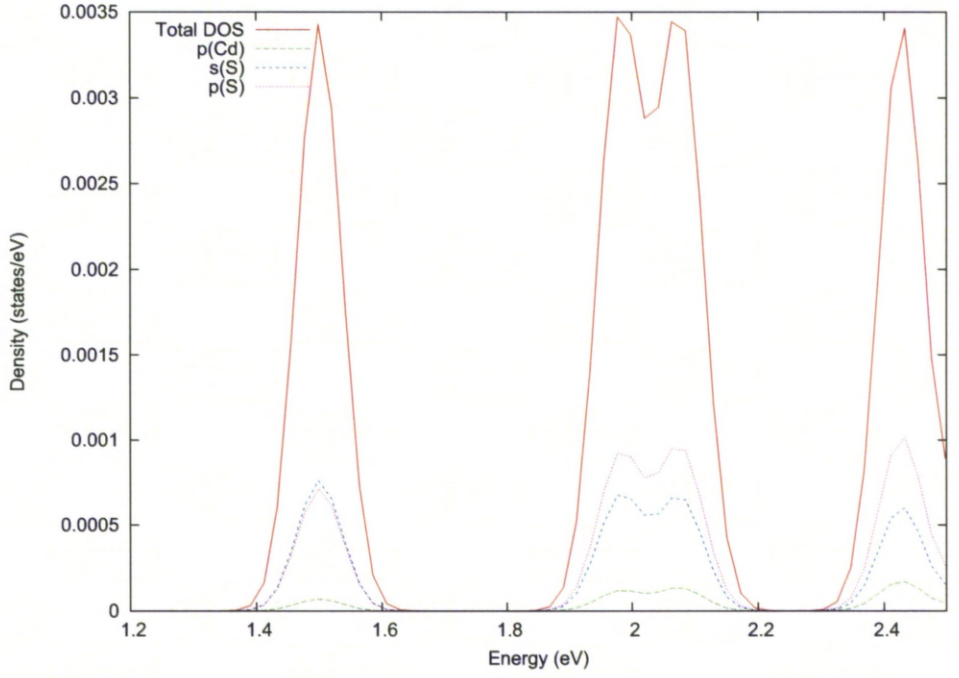

Figure 4.36: Density of States at Conduction Band edge from GGA Calculations for CdS Würtzite

The electronic structure of the chalcogenide-derived unit in **1** is thus very similar in terms of the orbitals contributing to the band edge transition to that of bulk CdS (rock-salt and würtzite), despite the molecular origin of the S moiety here. The p_S contribution on the edge of the valence band in **1** extends from -0.3 to -1.6 eV (1.3 eV wide) before becoming negligible. The equivalent contribution in the bulk CdS phases is spread over 5.5 eV (rock salt CdS) and 4.2 eV (würtzite CdS). The s_{Cd} contribution on the edge of the conduction band in **1** extends from 3.7 to 5.5 eV (1.8 eV wide) before becoming negligible, whereas in the bulk phase the spread is over 4.6 eV (rock salt CdS) and 4.2 eV (würtzite CdS), confirming that the energy widths of the p_S and s_{Cd} bands in **1** are significantly decreased by reduction of the S coordination number.

The DOS at the edge of the valence band in **1** is predominantly from p_S orbitals, while the DOS on the edge of the conduction band is essentially based on s_{Cd} orbitals. The contribution of atoms other than S on the edge of the valence band of **1** is extremely weak. This pattern is identical to that observed in both CdS bulk phases (würtzite and rocksalt). A band edge optical transition (between p_S adn s_{Cd} states) in **1** corresponds to a change in wavevector and thus needs to be phonon assisted, giving the indirect gap behaviour found for the high pressure bulk CdS rocksalt phase. The würtzite phase of CdS displays a direct gap electronic structure. This result illustrates the relationship between **1** and the rock-salt phase of bulk CdS. The Cd is in a six coordinate environment with a mer arrangement of electronic-structure-determining S donors that corresponds more closely to the high pressure than the ambient pressure tetrahedrally coordinated polymorph of CdS. This arrangement is enforced by the tridentate nature of the chelating amino acid ligand.

Zn(L-cysteinate) and ZnS

For **2** we cannot directly compare the theoretically optimised structure to the results obtained from experiment due to the expansion in the structure. However, we can look at the theoretical results from the optimised structure and also for the experimental structure (not allowing VASP to optimise the structure when calculating). This can help us evaluate key characteristics of **2** and possible reasons for the change in the structure.

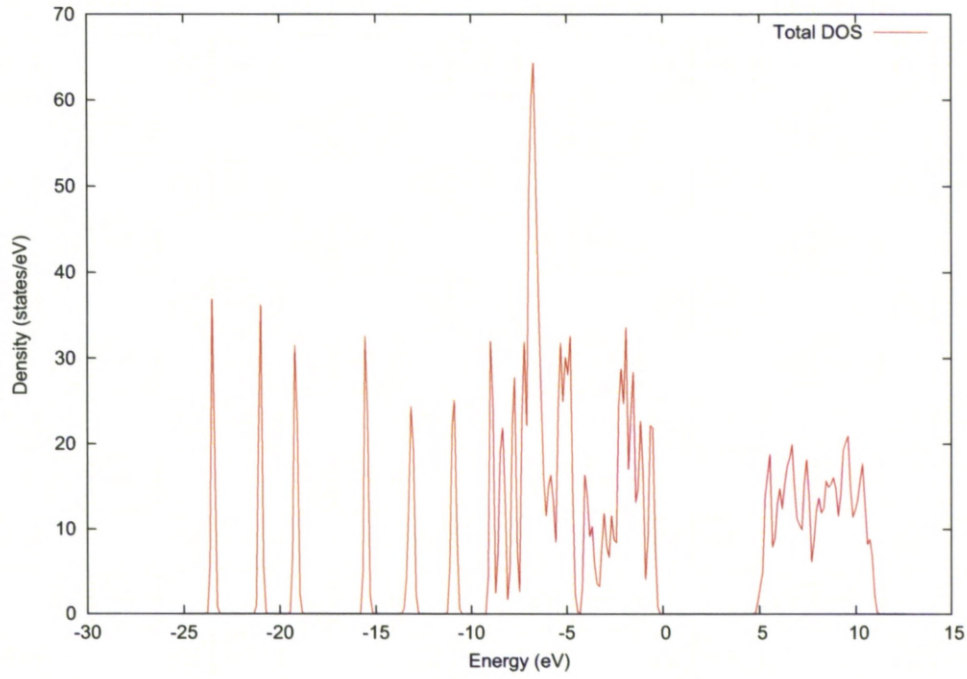

Figure 4.37: Density of States from Hybrid Calculations for the optimised **2** structure

The calculated density of states for optimised **2** (Figure 4.37) from the hybrid functional calculations allows us to evaluate a theoretical band gap of 5.15 eV. Observation of the energies at specific k-points allowed us to determine the nature of the band gap. For optimised **2** a single k-point (0.000, 0.000, 0.000) was found to correspond to both the highest energy of the valence band and the lowest energy of the conduction band. This indicates that the optical band edge transition is therefore direct.

The calculated value of the band gap slightly overestimates the value obtained by experiment which was 5.05 eV for a direct transition, although due to change in structure it is hard to draw a direct comparison between these results.

A detailed study of the atomic parentage of the levels involved in the band edge transition in **2** reveals that the edge of the valence band (Figure 4.38) is mostly composed of p orbitals of sulphur atoms with less prominent contributions from p_O and d_{Zn}. The p orbitals of Carbon give the main contribution to the levels on the edge of the conduction band, with the main contribution from the ZnS substructure coming from the s orbitals of Zinc (Figure 4.39).

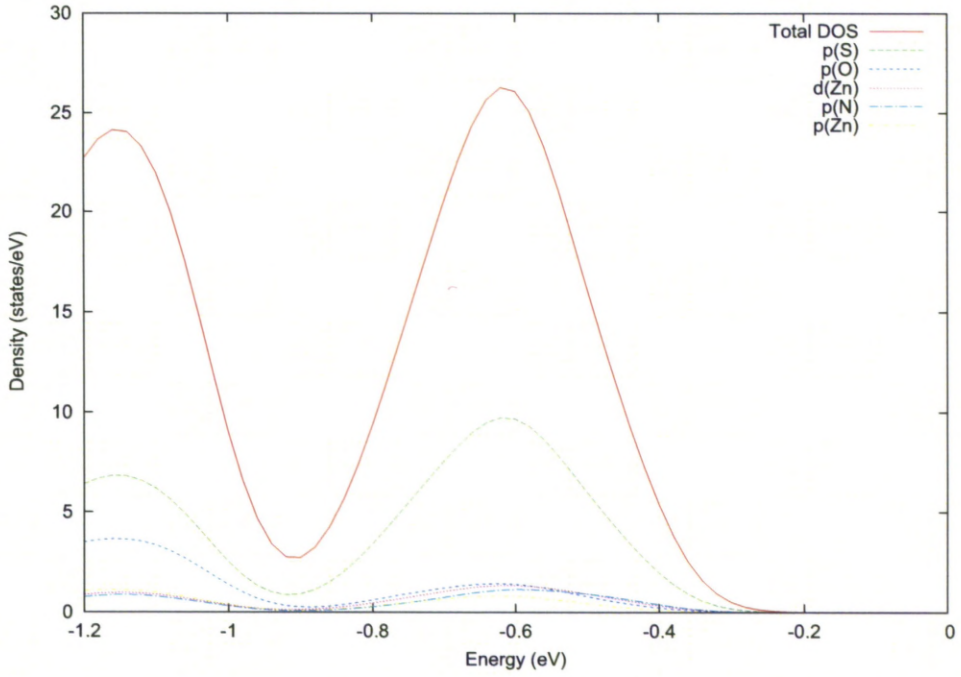

Figure 4.38: Density of States of the Valence Band edge from Hybrid Calculations for the optimised **2** structure

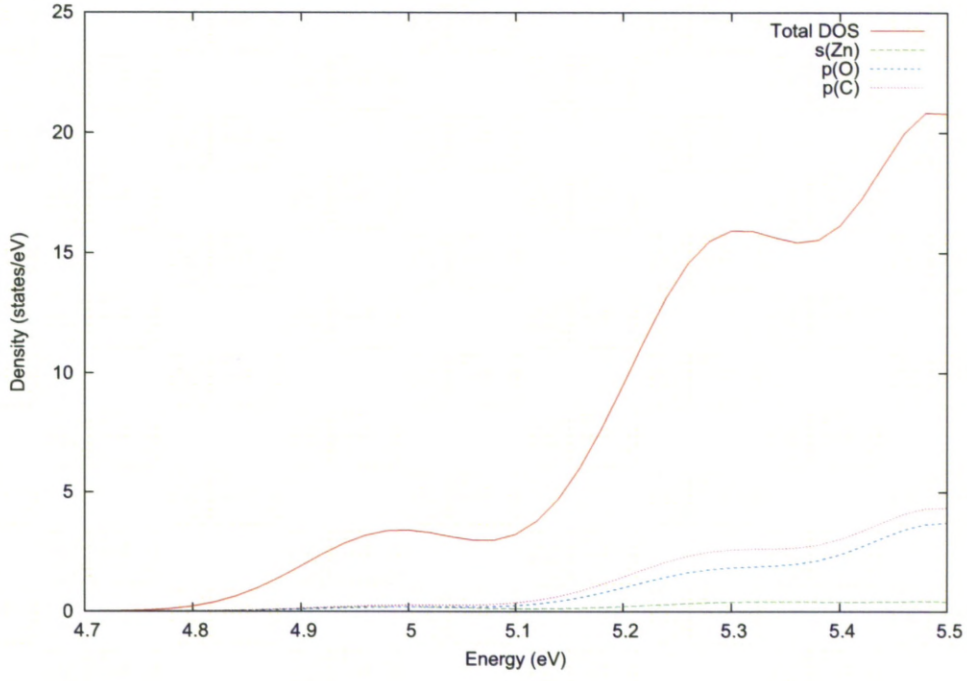

Figure 4.39: Density of States of the Conduction Band edge from Hybrid Calculations for the optimised **2** structure

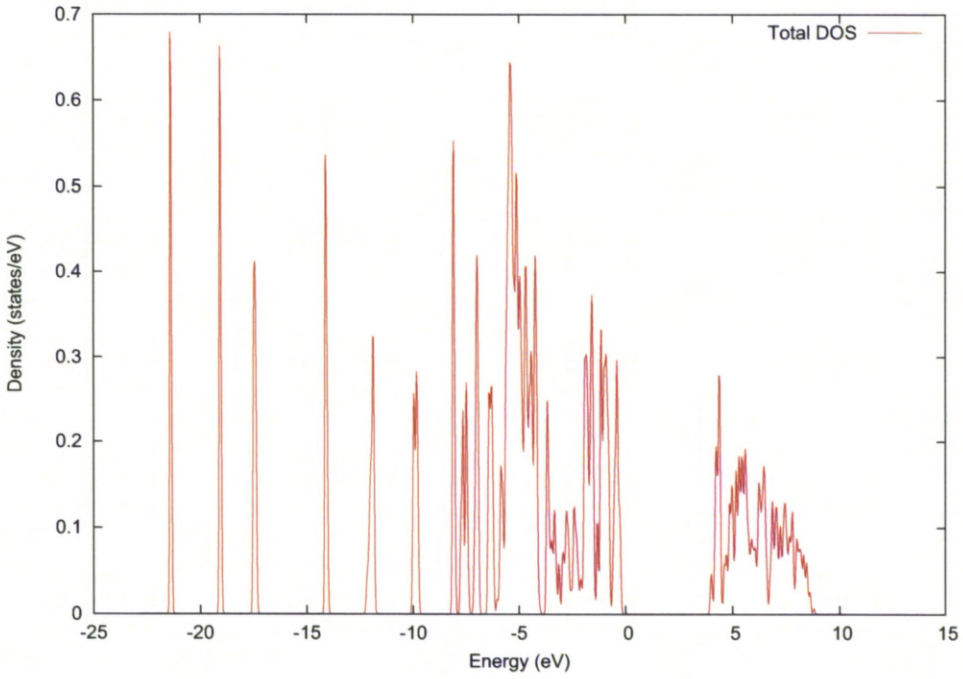

Figure 4.40: Density of States from GGA Calculations for the optimised **2** structure

The GGA calculations of the optimised **2** give a band gap of 4.35eV. Similarly, with the comparison of hybrid and GGA calculations for **1** we see shared characteristics in the DOS with six molecular states below -10eV and more compact bulk states either side of the band gap. The optical band edge was seen to be direct with both the highest energy of the valence band and the lowest energy of the conduction band corresponding to the single k-point (0.000 0.000 0.000). Also, similar to the GGA calculations in **1** we see a reduction in the energy range that the bulk states occupy either side of the band gap.

The atomic parentage of the levels involved in the band edge transition in GGA calculated optimised **2** reveals the same major contributions as found in the hybrid calculations. At the edge of the valence band (Figure 4.41) it is mostly composed of p orbitals of sulphur atoms with less prominent contributions from p_O and d_{Zn}. The p orbitals of Carbon give the main contribution to the levels on the edge of the conduction band, with the main contribution from the ZnS substructure coming from the s orbitals of Zinc (Figure 4.42).

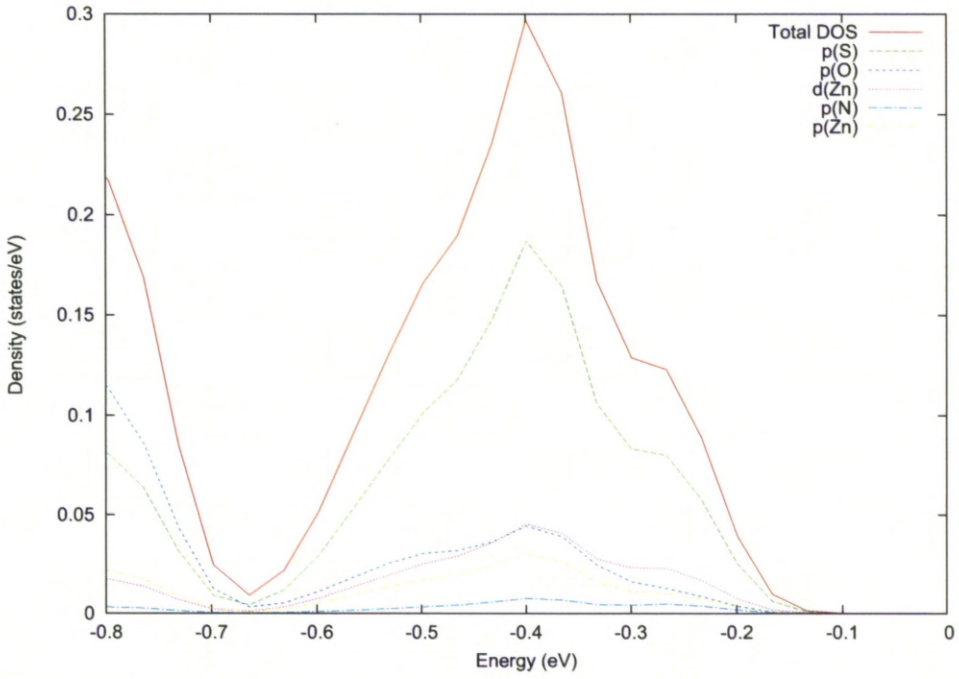

Figure 4.41: Density of States of the Valence Band edge from GGA Calculations for the optimised **2** structure

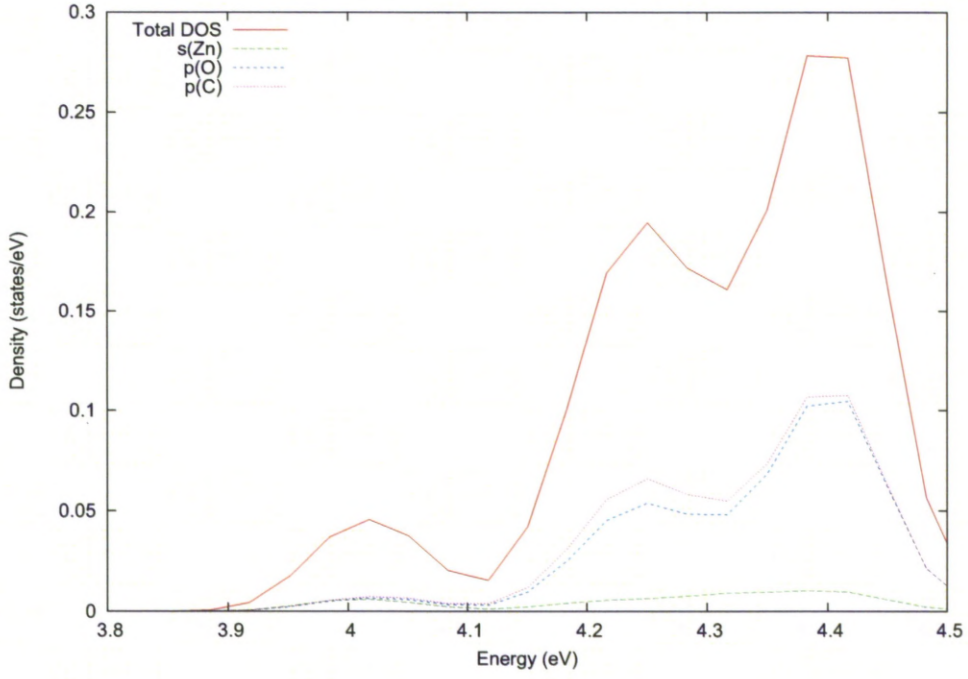

Figure 4.42: Density of States of the Conduction Band edge from GGA Calculations for the optimised **2** structure

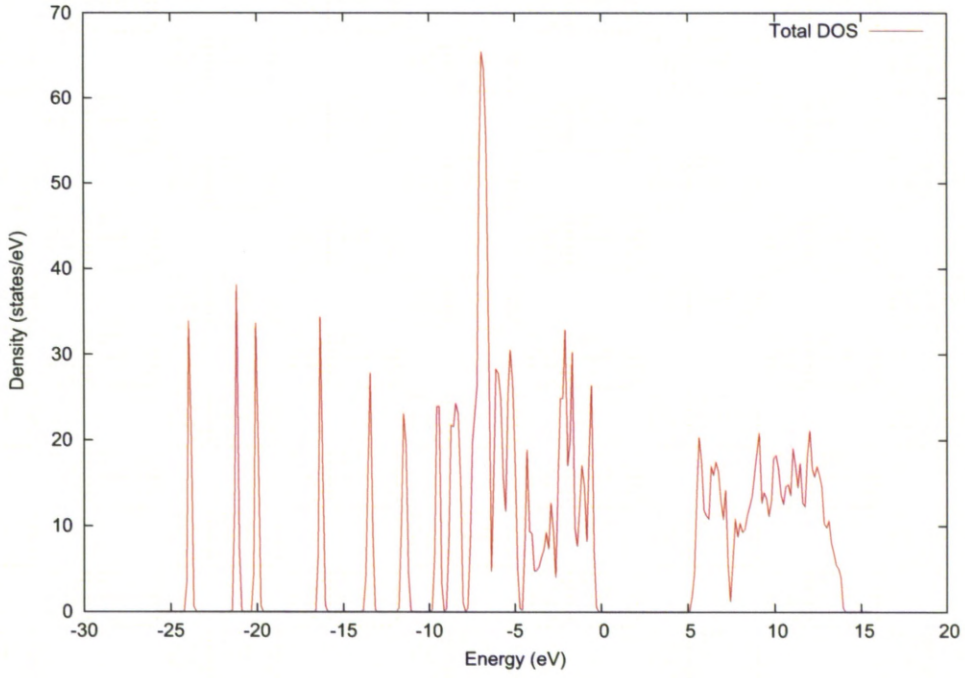

Figure 4.43: Density of States from Hybrid Calculations for the un-optimised **2** structure

For the structure as deduced from experiment the VASP calculated DOS gives a band gap of 5.55eV. This is larger than the gap derived from experiment of 5.05eV and that of opimised **2** structure of 5.15eV (Figure 4.43). The key characteristics of the DOS remain for both the optimised and un-optimised structures (Figures 4.37 and 4.43) with a small shift in the conduction band edge in un-optimised **2** giving rise to a slightly larger band gap. However, here we see an indirect gap with the highest energy of the valence band arising from the k-point (0.000, 0.000, 0.333) and the lowest energy of the conduction band at k-point (0.000, 0.000, 0.000).

The same major contributions from the atomic parentage as the optimised **2** with p_S at the valence band edge (Figure 4.44) and p_C (s_{Zn} from ZnS substructure) at conduction band edge (Figure 4.45) dominating.

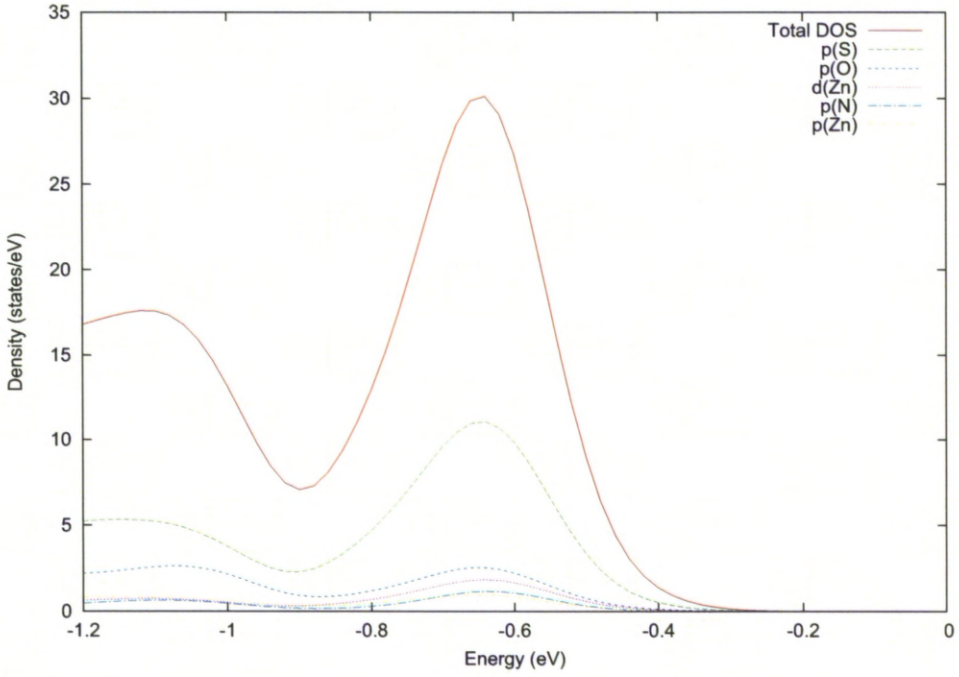

Figure 4.44: Density of States of the Valence Band edge from Hybrid Calculations for the un-optimised **2** structure

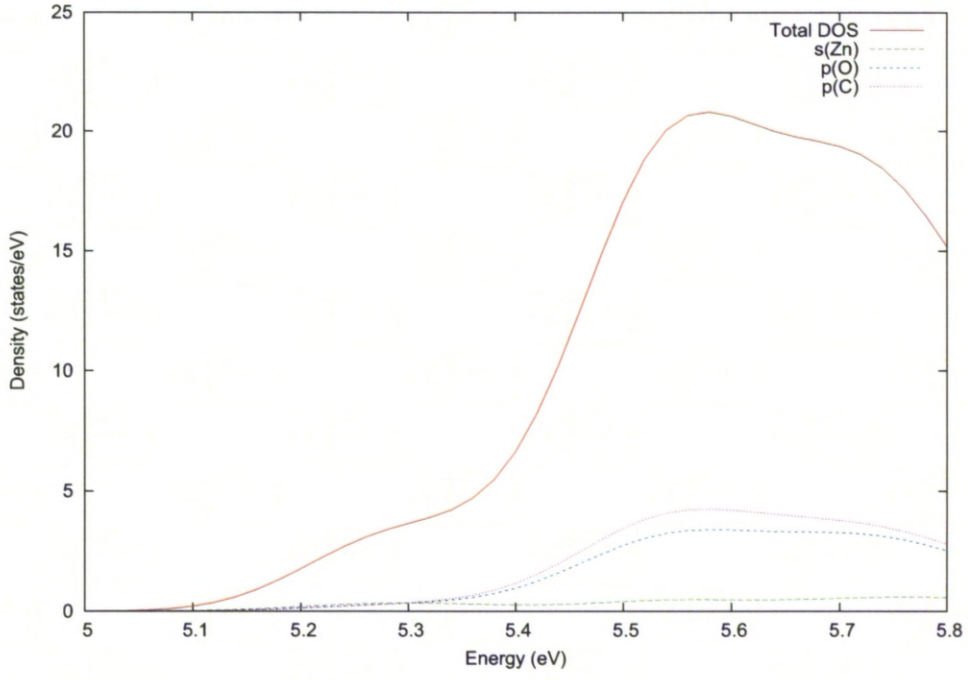

Figure 4.45: Density of States of the Conduction Band edge from Hybrid Calculations for the un-optimised **2** structure

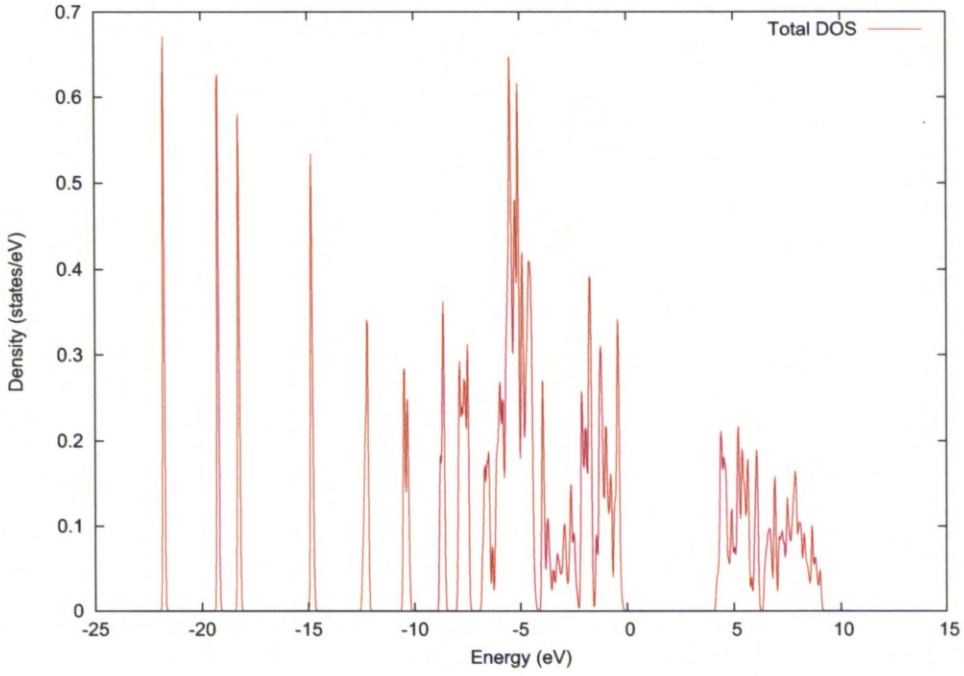

Figure 4.46: Density of States from GGA Calculations for the un-optimised **2** structure

The GGA calculations of the un-optimised **2** returns an indirect band gap of 4.35eV (Figure 4.46) with the highest energy of the valence band found at k-point (0.000, 0.000, 0.000) and the lowest energy of the conduction band found at k-point (0.000, 0.333, 0.000).

The same major contributions from the atomic parentage as the optimised **2** and the hybrid calculations for the un-optimsed **2** with p_S at the valence band edge (Figure 4.47); and p_C and (s_{Zn} from ZnS substructure) dominating at the conduction band edge (Figure 4.48).

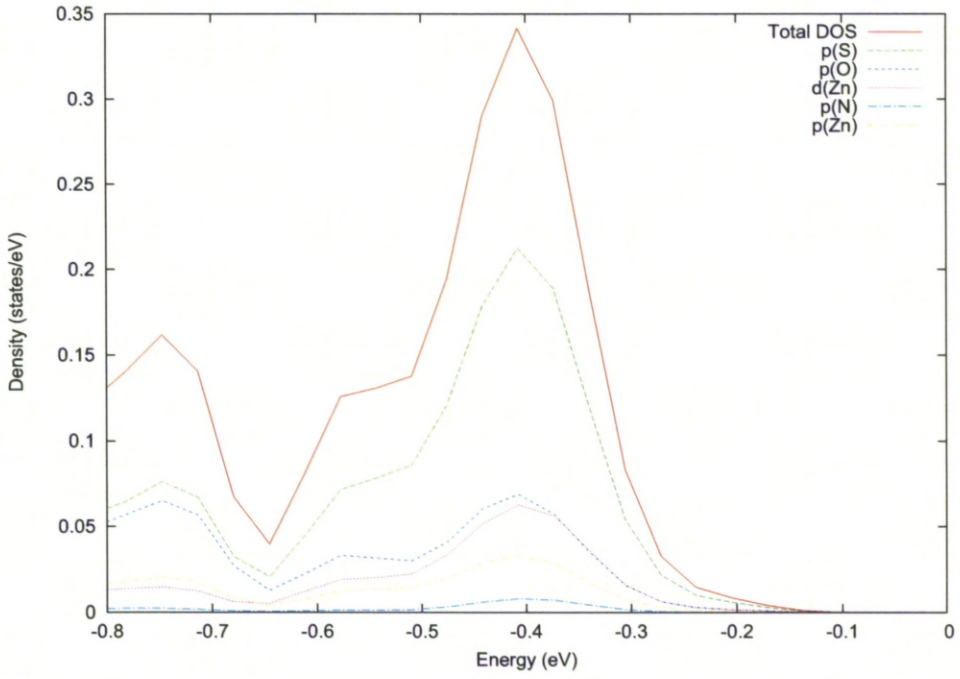

Figure 4.47: Density of States of the Valence Band edge from GGA Calculations for the un-optimised **2** structure

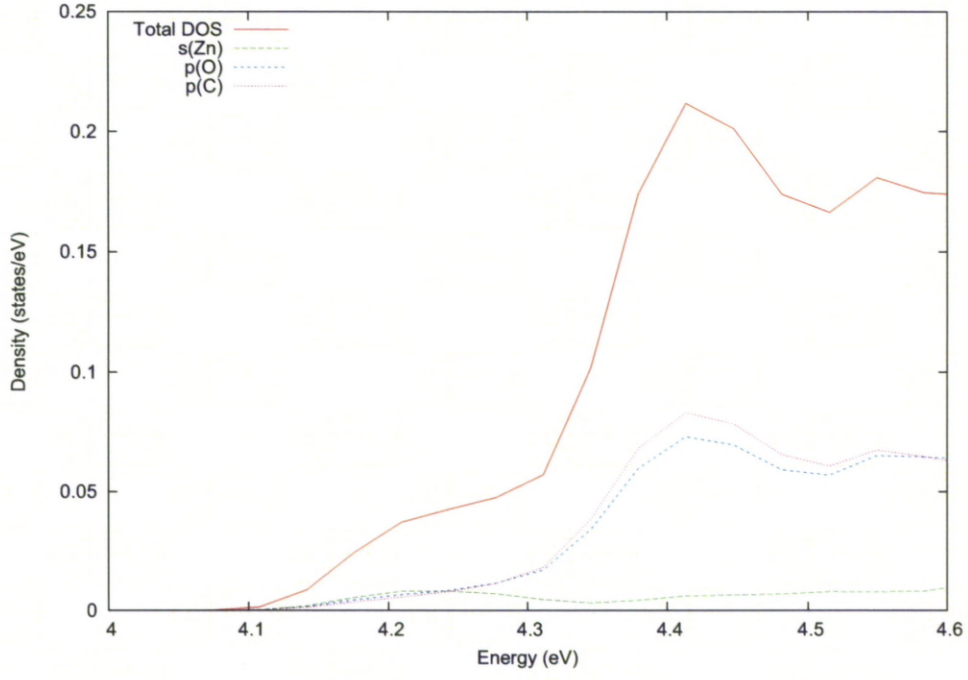

Figure 4.48: Density of States of the Conduction Band edge from GGA Calculations for the un-optimised **2** structure

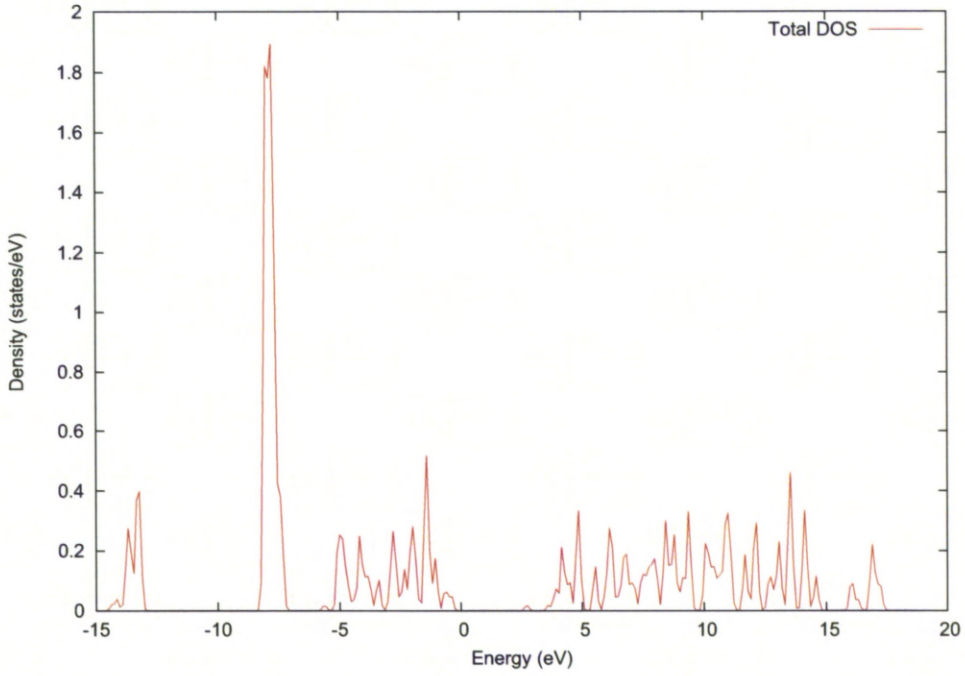

Figure 4.49: Density of States from Hybrid Calculations for the optimised ZnS structure

We can further evaluate **2** by looking at the ZnS substructure by analysing the bulk ZnS würtzite structure. The calculated band gap was found to be 3.5 eV (Figure 4.49), which is slightly less than the experimental bandgap of 3.68eV. The lowest energy of the conduction band and the highest energy of the valence band correspond to the same k-point (0.000, 0.000, 0.000). Hence the ZnS würtzite phase is a direct gap system. This agrees with experiment. The same major contributions are observed on the edge of the gap in bulk würtzite ZnS as with both optimised and un-optimsed **2** with p_S dominating at the valence band edge (Figure 4.50) and s_{Zn} likewise at the conduction band edge (Figure 4.51).

The calculations here thus agree with the experimental finding that the gap increases as the Zn coordination number decreases

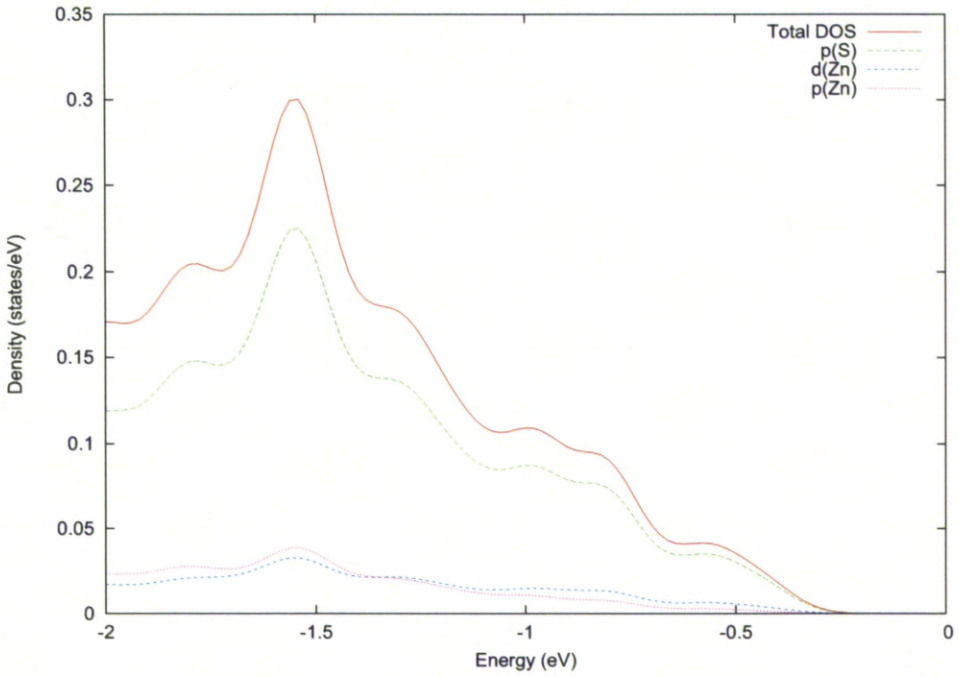

Figure 4.50: Density of States of the Valence Band edge from hybrid Calculations for the optimised ZnS structure

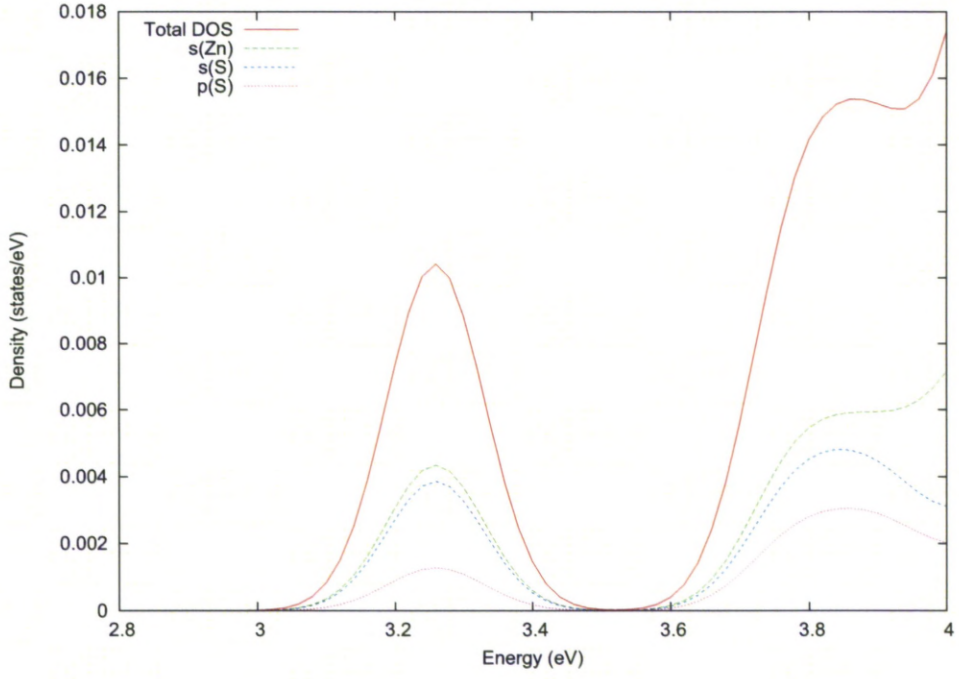

Figure 4.51: Density of States of the Conduction Band edge from hybrid Calculations for the optimised ZnS structure

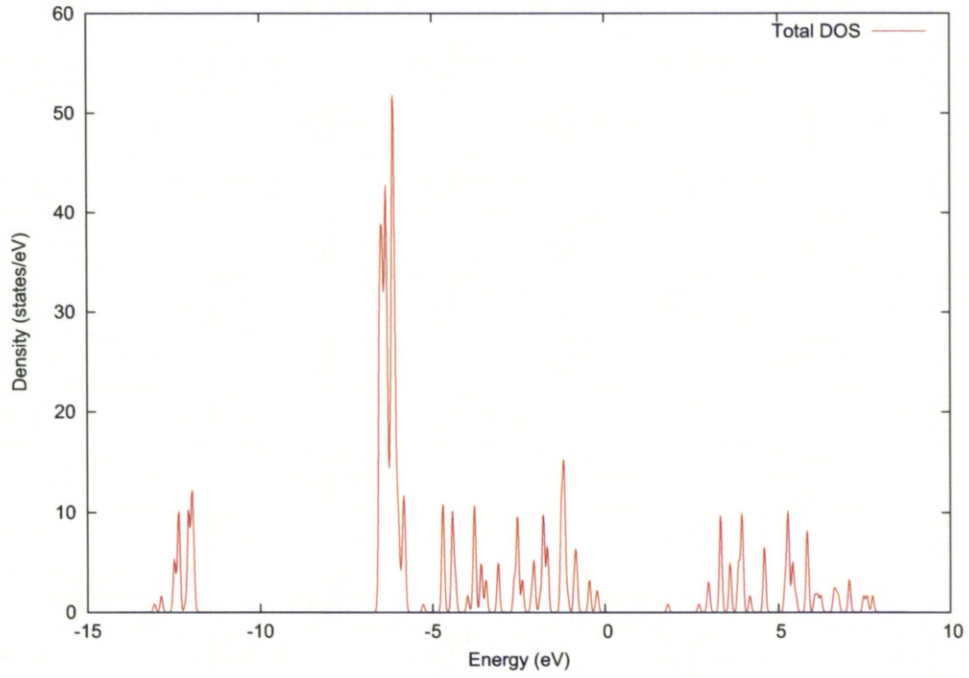

Figure 4.52: Density of States from GGA Calculations for the optimised ZnS structure

From the GGA Calculations for the würtzite ZnS we obtain a band gap of 1.95eV (Figure 4.34). Despite this as with the GGA and Hybrid calculations for **2** and the hybrid calculations for the same würtzite ZnS structure it shares the same prominences in the atomic parentage at the valence and conduction band edge. With a p_S dominance at the valence band edge (Figure 4.53) and a s_{Zn} dominance at the conduction band edge (Figure 4.54). Similarly, DFT determined the würtzite ZnS structure to have a direct band gap.

Comparing the theoretical DOS for the optimised and un-optimised **2** (Figures 4.40 and 4.46) we can see they are very similar with 6 molecular states less than -10eV and near identical prominences in the bulk states either side of the band gap which only differ by 0.4eV. From this we can deduce that the the one dimensional substructure remains near enough unchanged from experiment (Figure 4.14) although the inter-planar bonding between the 1D substuctures has not been determined correctly by X-Ray diffraction resulting in the large 18% difference between the inter planar distance as deduced by experiment (89.21°) and VASP (73.12°).

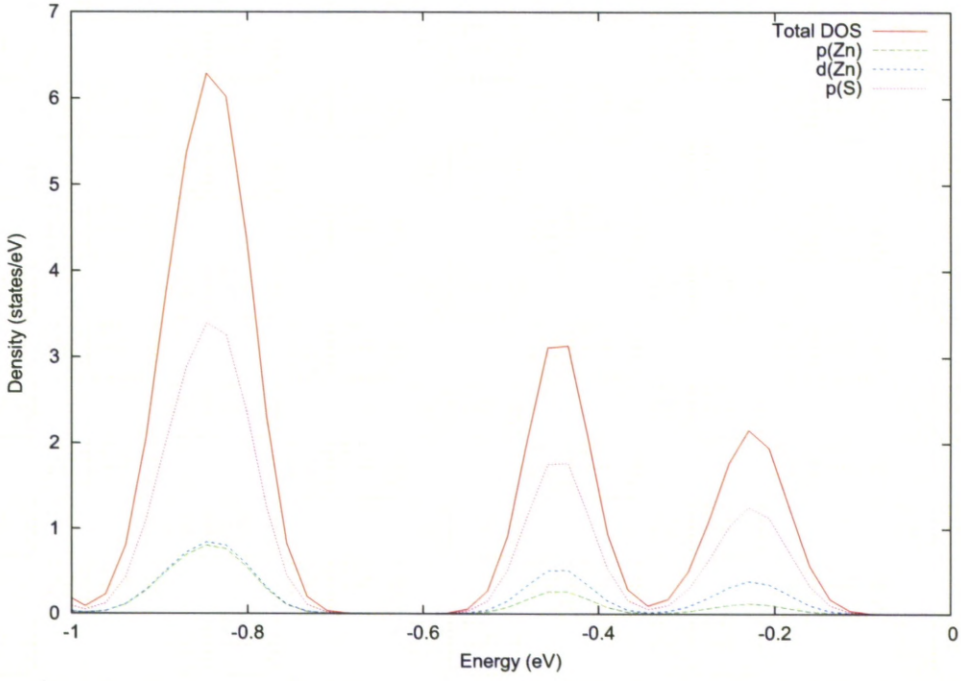

Figure 4.53: Density of States of the Valence Band edge from GGA Calculations for the optimised ZnS structure

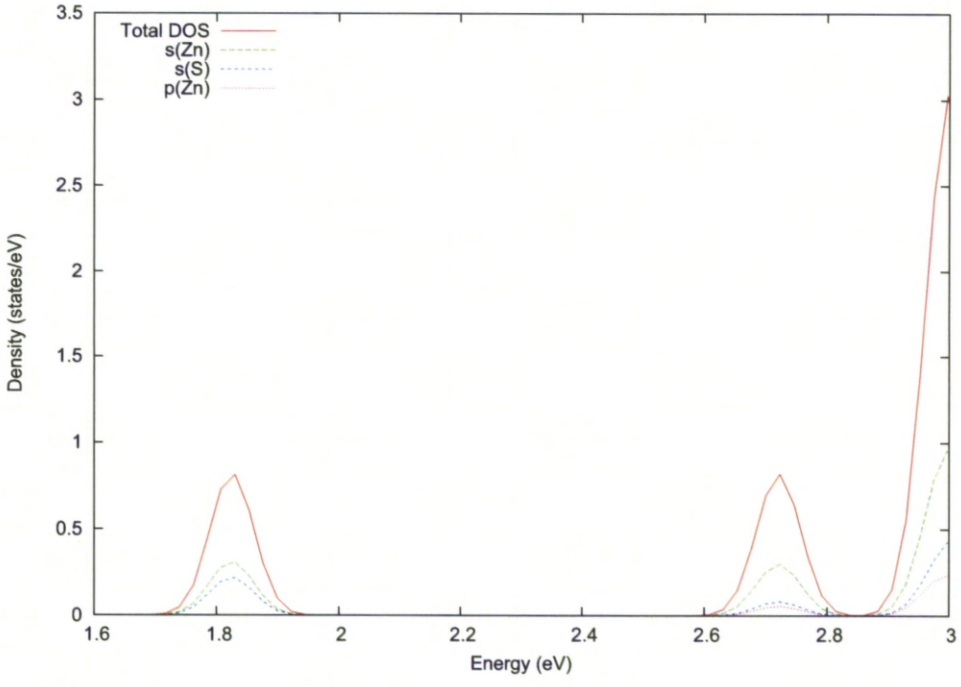

Figure 4.54: Density of States of the Conduction Band edge from GGA Calculations for the optimised ZnS structure

4.3 Conclusion

1 displays a local structure reminiscent of the rock salt phase of CdS, with an electronic structure and optical properties related to this CdS bulk phase. In **2**, the local arrangement of the metal and sulphur atoms is a distorted 1D fragment of the bulk würtzite phase and the decrease of the ZnS system dimensions manifests itself by a blue shift of the absorption edge. The magnitude of the blue shifts observed in **1** and **2** is in agreement with the trends observed by decreasing dimensionality from bulk to 2D, then to 1D structures [85].

The density of states at the edge of the valence band in **1** is predominantly from p_S orbitals, while the DOS on the edge of the conduction band is essentially based on s_{Cd} orbitals. The contribution of atoms other than S on the edge of the valence band of **1** is extremely weak. This pattern is identical to that observed in both CdS bulk phases (würtzite and rock salt). A band edge optical transition (between p_S and s_{Cd} states) in **1** corresponds to a change in wavevector and thus needs to be phonon assisted, giving the indirect gap behaviour found for the high pressure bulk CdS rock salt phase. This was different to the würtzite phase of CdS which displays a direct gap electronic structure. Note we get the correct contraction of the band widths due to less bonding in the molecular structure.

The density of states at the edge of the valence band in the optimised and unoptimised **2** is predominantly from p_S orbitals, while the DOS on the edge of the conduction band is essentially based on p_C and s_{Zn} orbitals. This is identical to that as observed in the ZnS bulk würtzite phase for Zn and S contributions. The 1D substructure remains constant from experiment in **2** with X-ray diffraction potentially not predicting the inter planar connections correctly.

As previously expected DFT underestimates the band gap, although it matches the key characteristics of gap type and atomic parentage shown by hybrid calculations albeit with more compact bulk states. A comparison of band gaps between experiment, hybrid and DFT is shown in table 4.1.

Table 4.1: Summary of band gaps (eV) for **1**, **2**, CdS (würtzite and rocksalt) and ZnS)

Structure	Experimental	Hybrid	GGA	Nature of gap
1	4.29	4.2	3.25	indirect
CdS rocksalt	1.7	1.1	0.3	indirect
CdS würtzite	2.42	2.35	1.55	direct
Optimised **2**	-	5.15	4.35	direct
Un-optimised **2**	5.05	5.55	4.35	indirect
ZnS würtzite	3.68	3.5	1.95	direct

Chapter 5

A simplified Genetic Algorithm approach to Materials Design

5.1 Introduction

Over the last 20 years many new methods have been developed for the problem of cluster geometry optimisation, namely the search for the lowest energy configuration of a cluster of a given number of atoms in a given potential. A cluster can consist of between a few to many millions of atoms, ions or molecules. The constituents of a cluster may all be identical or cover many different species. Clusters are particularly interesting in that they constitute a new type of material which may have properties which are distinct from those of discrete molecules of bulk matter [86]. Of particular interest which is also useful when analysing cluster geometry optimisation is the size dependent evolution of cluster properties. Due to the nature of clusters, many of their properties are difficult to measure experimentally so theory can play a key role. However, *ab initio* calculations can prove difficult for large clusters as they are computationally expensive. Here empirical atomistic potentials can play a role.

One of the methods used for cluster geometry optimisation is the Genetic Algorithm (GA). GAs are an Evolutionary Algorithm based on a Darwinian "survival of the fittest" approach. Primarily, regardless of whether using empirical potentials or *ab initio* theory to describe the bonding in clusters, the main objective

in optimising the cluster geometry is to find the arrangement of atoms, ions or molecules that corresponds to the lowest potential energy, otherwise known as the global minimum (GM). Clusters corresponding to the GM are the most likely candidates for the most probable structure formed in a cluster experiment. Obviously, this depends on the nature of the experiment which may form the metastable (local minimum) structure due to the conditions of the experiment.

As expected the number of local and global minima present increase with the cluster size therefore the process of finding the GM becomes more difficult as you increase the number of constituents in a cluster. Traditional Monte Carlo and Molecular Dynamic (MD) type approaches often encounter difficulties in finding the global minima for particular types of interatomic interactions [87]. Here is where GAs can excel in improving the success of cluster geometry optimisation. It uses operators that are analogues of the evolutionary processes of mating, mutation and natural selection to explore multi-dimensional parameter spaces. They were first developed by John Holland in 1975 [88] and they are a stochastic global optimisation method. It is a computational technique which is used to solve problems in which there are many potential solutions, but only a few of which are optimal.

5.1.1 Terminology

GAs developed from a biological problem, hence, a GA can be applied to any problem where the variables to be optimised can be encoded to form a string where each string represents a trial solution of the problem. I will discuss some of the terminology here used throughout the GA process as discussed by Johnston [86]. This covers operators and methods that have been previously used, but not necessarily used in the development of the program I produced and used.

As an evolutionary process we start a typical GA with a population of individual constituents which as Darwin showed evolve over a number of generations. The number of generations is a variable that can be defined as a fixed number or determined by some exit criteria dependent on the suitability of the population at a given generation.

The initial population is usually a randomly generated set of individuals to prevent

bias in the search for, in this case, a globally optimised cluster. Although, previous knowledge of structures can and has been used as a starting point.

It is important to measure the quality of a population with respect to what is being optimised. This is otherwise known as the fitness of the population. If we know the upper and lower limits of the function being optimised then we can use the absolute fitness. In this case we can compare the fitness of an individual constituent from generation to generation. However, in most cases for cluster geometry optimisation this is not known. In most instances for GAs dynamic fitness scaling is used. The fitness of individual constituents is then compared relative to the best and worst members of the current population. The fitness of individuals is important to determine which will take part in mating and crossover and survive to the next generation i.e. "survival of the fittest."

From the fitness operator we can determine the selection process. The selection process will determine which individual constituents are chosen for the subsequent crossover. There are many methods available for this, with a new method to be discussed later that is used in the program developed for this thesis. Two more popular methods are the roulette wheel selection and tournament selection. For the roulette wheel selection a string is chosen at random and if its fitness value (with the fitness value being between 0 and 1) is less than a randomly generated number then the string will be chosen for crossover. If not, another string's fitness value will be compared. A 'better' fitness value increases the probability of being chosen. The tournament selection selects a number of constituents from a population to form a 'tournament' with the two strings of highest fitness being selected from each tournament.

Once we have selected our constituents / strings we can perform the crossover or mating of the, what are now known as the, 'parent' strings to generate 'offspring'. As with the selection operator there are many methods for the mating process, with again a different method applied in this thesis which will be discussed later. Earlier forms of GAs for cluster geometry optimisation and other problems used binary strings for representation and it will be used here to describe some mating operators. In one-point crossover, the two parent strings are cut at the same point with the complementary parts of the parents combined i.e. the first part of parent 1 with the second part of parent 2 and vice versa. As Binary strings this could

see two parents 11010011 and **01011001** become 11011001 and **01010011**. In a two point crossover we see the parents cut at two points with the middle sequence of either parent being inserted into the middle of the other parent. Using the same parents as above this could yield the offspring 11**011011** and **01**010**001**. Another method is the uniform crossover where a certain number of variables (or genes to use a biology analogy) is found in the offspring from each parent with no restriction on where these genes occur in the parents.

The mating process can eventually lead to stagnation with a lack of diversity in the population since we are only mixing genetic material that previously existed. This stagnation could see the population converge to a non optimal local minimum solution. We can introduce a mutation operator into the GA to introduce new genetic material into the population and to help diversity. For example, mutation would see a binary offspring string change from 11011011 to 11010011. There are two types of mutation, static and dynamic. The former gives a random value to the mutated gene whereas the latter changes the gene by a small random amount. The different mutation operators can take even more forms when applying them to the specific problem of cluster geometry optimisation.

5.1.2 Previous Work

In the last 20 years we have seen the use of GAs in cluster geometry optimisation with a variety of different methods and GA operators, but no definitive method has been produced. Early work in 1993 saw optimisation of small silicon clusters by Hartke [89] and molecular clusters (benzene, naphthalene and anthracene) by Xiao and Williams [90]. Both sets of work where produced with the cluster geometries encoded as binary strings similar to above. 1995 saw further development in the techniques and operators used. Bush, Catlow and Battle on a ternary oxide Li_3RuO_4 [91]. Hartke tried to address the known problems and attempted to address the first three [92]:

- Exponential increase of the number of local minima with cluster size;
- Suitable representation of the problem (e.g. choice of co-ordinates or parameters to be optimised);

- Proper representation of the search space;
- High expense of *ab initio* potential energy surface calculation.

A major development in how cluster geometry optimisations are performed by GAs was by Zeiri who used the real number cartesian co-ordinates instead of the previously used binary strings to represent the cluster geometries and subsequent minimisations and mating was performed without the need to encode and decode the 'genes' [93]. Deaven and Ho [94] also used cartesian co-ordinates, stating the use of a binary number string is "not very efficient." The use of a 3-dimensional 'cut and splice' crossover operator was also used here which gave a more physical meaning to the mating of two clusters. This involved random rotations of the cluster with one or two cuts through the clusters (similar to one and two point crossover discussed earlier) with the complementary fragments spliced together. Michaelian looked at small NaCl clusters using a binary representation up to an ion pair hexamer [95]. Up to 100 ions were evaluated in ionic sodium chloride clusters by Kabrede and Hentschke in 2002 [96] which introduced more options for genetic operators. Woodley et al [97] looked at restricting the search space by using knowledge of the cell dimensions and constituent elements to generate known binary and ternary oxides including perovskite structures.

Johnston's group at the University of Birmingham further looked at developing the GA operators looking at MgO clusters [87] amongst others and producing a review paper on the use of GAs [86]. Periodic systems were looked at by Abraham and Probert [98] with the enhancement of Deaven and Ho's cut and splice with the introduction of a wave-like cut to allow crossover between different cells.

5.1.3 Motivation

There has been plenty of work to try and develop GAs into a more real life approach in simulation [86], but throughout, more and more complicated GA operators are developed for selection, crossover and mutation of clusters. In this chapter a more primitive look at these operators will be examined to see if simpler GA operators can still yield correct results for the GM of a cluster. If so, then this could make GAs more efficient with less time needing to be spent on more complex 'cuts' or representations. Also, most work on ionic clusters works on the

preface that they are in ionic pairs and looks at even number of ions solely. No stoichiometry will be imposed throughout this chapter and an odd number of ions will also be considered. The method used in this chapter develops more primitive operators to help towards generating a more efficient GA.

5.2 Genetic Algorithm Program

A flow chart showing the operation of my cluster geometry optimisation program is show in figure 5.1. The specific features of the program are described in more detail below.

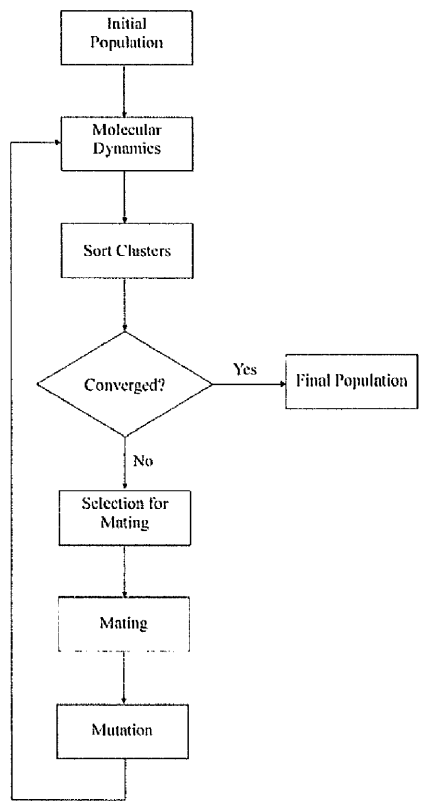

Figure 5.1: Flow Chart for the cluster genetic algorithm used within this chapter.

5.2.1 Initial Population

The initial population is generated for a set number of clusters N_{clust} with each containing a set number of atoms / ions N. These are generated at random using a random number generator from numerical recipes in Fortran [99]. This is scaled to a fixed size cell which is set at the start of the calculation to give the cluster geometry in cartesian co-ordinates. The number of types of element to be investigated by any calculation can also be set here, but for the purposes of this chapter we will only be investigating two. The mass of each constituent ion is kept the same regardless of type. The initial population is then minimised by Molecular Dynamics (MD).

5.2.2 Molecular Dynamics

The clusters are minimised using MD following the Verlet Algorithm (see chapter 2.6). From this the clusters are minimised with energy conserved throughout with the output being a MD optimised cluster geometry and a Total Energy for the cluster which can be used to test the fitness of a cluster and ultimately determine if the particular cluster is the GM. The MD is run with a temperature of 100K. With the temperature kept constant there will remain a 1KJ error bar on results.

Potential

A simple pair-wise potential is used, that keeps computational runtime to a minimum whilst also suitable for simple ionic clusters. The variables in the potential are fitted to produce a NaCl dimer separation distance of approximately 2.5Å.

$$V = ae^{(-\alpha r)} + \frac{e_1 e_2 b}{r} \tag{5.1}$$

where r is the distance between two atoms / ions, 1 and 2; e_1 and e_2 are the charge on the ions (+1 and -1 for Na and Cl type ions for this investigation); and $a = 10$, $b = 0.3$ and $\alpha = 2.5$ are variables to be set.

5.2.3 Sort Clusters

For the method of crossover used the clusters are sorted by centering each cluster around the nearest Na type ion closest to the centre of mass of the cluster. A heap sort [99] is used to sort the atoms in order according to the distance from the now central Na-type ion.

5.2.4 Convergence Check

The convergence check involves the program deciding whether it believes it can no longer find a better match to the GM of the cluster. For this we have set two exit parameters which are set at the start and which can be varied to investigate how the values of these parameters affects the ability of the program to find the GM. Obviously, we want to be able to leave the program running long enough to potentially find the GM, but with in many cases not knowing the GM before performing the calculation we need suitable criteria to ensure that the program does eventually stop.

For this program there is a convergence check every 10 generations, with a maximum number of generations also set to ensure that any particular calculation is not never-ending. The two parameters to be set are an exit threshold, T_x, and C_x. Every 10 generations we check the energy of the best cluster. If the percentage energy difference from the energy 10 generations previous is less than T_x then 1 is added to a count. If the energy difference is greater than T_x then the count is reset to zero. When the count is equal to C_x we exit the program to return the final population.

5.2.5 Selection for Mating

The selection of parents is important in selecting adequate clusters with a high fitness value to ensure that we achieve evolution across the generations to help us find the GM. Here we use a different type of selection than discussed earlier. The selection operator used here allocates the fitness of both parents at a time rather than the the fitness of the individual. This then looks at their suitability for mating.

A probability of any two clusters mating is generated for every combination which are subsequently sorted by lowest $P_m$with the required number of parent pairs passed onto mating. This probability is defined as:

$$P_m = 0.5 + | \frac{E_i - E_j}{E_j} | \tag{5.2}$$

where $E_i > E_j$ with both being the energy of two parent clusters with $i \neq j$.

This method of mating also has the added benefit of involving a bit more diversity into the selection process with the highest two energy clusters potentially having a lower mating probability than the first and third lowest energy structures.

5.2.6 Mating

As discussed earlier a different operator is used here to look at a more primitive approach to mating, in some aspects similar to that of the binary string representation. We now have ordered lists of pairs of clusters according to their suitability for mating with each other with each cluster centred at the Na-type ion closest to the centre of mass and ordered outwards from this point. Two clusters can be represented as two ordered lists of atoms as per figure 5.2

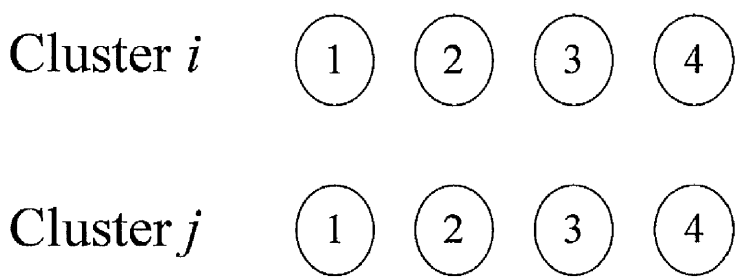

Figure 5.2: Figure of two clusters with N=4 to explain mating operator

If cluster i is the lowest energy cluster we set atom / ion 1 as the first atom / ion in the offspring. For the following atom selections we generate a random number. If the random number is less than P_m then atom 2 of cluster i is chosen otherwise atom 2 of cluster j is chosen. This is repeated until we have N atoms / ions in each offspring with the operator being used again for subsequent selected pairs until we have N_{clust} offspring.

5.2.7 Mutation

One type of mutation has been used here which was described as atom permutation by Johnston [86]. A mutation parameter, P_{mut}, is set at the start of the program and is fixed throughout. Each cluster is passed through the operator an atom at a time. If a random number that is generated is less than the mutation parameter set then the atom type of that particular atom is changed without changing the geometry of the structure. This type of mutation is usually used for ionic clusters.

5.2.8 Subsequent Generations

The process described above is repeated until the convergence check criteria is matched. To help maintain a forward moving process to always maintain the structure is either kept the same or improved, we can make the GA elitist by passing the lowest energy structure from the previous generation to the current generation without mating or mutation, to ensure the best member of the population cannot get worse from one generation to the next.

5.3 Results

Clusters of size $N = 4-20, 30, 40, 50$ were evaluated by the GA program produced for this thesis looking at not only the possible GM for each cluster, but also how parameters such as N_{clust}, the mutation parameter and the convergence criteria effect the ability and speed to converge to the GM. Each cluster will be looked at separately with comparisons made to NaCl clusters calculations by Ayuela et al [100], Michaelian [95] and Kabrede and Hentschke [96]. The energy and the development of the energy with each generation will also be evaluated with respect to the number of clusters, N_{clust}, in the population and the mutation parameter. The mutation parameter is set essentially as a percentage, with a random number generated to test if an ion will be mutated. The higher the percentage, the more chance of mutation occuring. A range of exit parameters are also investigated to test for any possible preferred values. When the relative parameter is not getting investigated the following values are set: $N_{clust} = 10$, $T_x = 0.01\%$, $C_x = 5$ and $P_{mut} = 20\%$. The units of the energy throughout is in Hartrees.

5.3.1 N=4

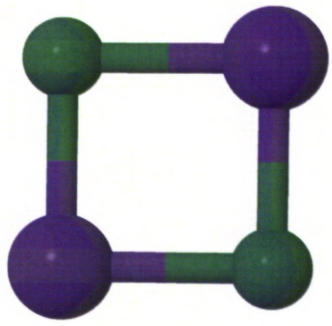

Figure 5.3: N=4 GM Cluster

As expected for N=4 we see a square structure consisting of two Na ions and two Cl ions (figure 5.3). This matches the findings by Ayuela, Michaelian and Kabrede. Having a small number of ions there are fewer local minima structures possible for the four ions to settle in, although this is increased with no restraint on the stoichiometry unlike the comparative papers considered here. In figure 5.4

it shows that $N_{clust} = 2, 5$ both exist in local minima briefly at the start of the evolutionary process. $N_{clust} = 10$ is in the GM cluster from the first generation. The larger value of N_{clust} creates a higher possibility of the global minimum being found just from MD.

This is further highlighted when looking at figure 5.5 which shows all values of the P_{mut} parameter yielding a GM structure from the first generation. The fluctuation in energy is due to the MD retaining some kinetic energy in the clusters. This also shows that in this case mutation is not necessary.

All possibilities of the exit parameters set give the GM cluster. The GA program checks every ten generations comparing the current energy to the energy ten generations ago to see if the convergence criteria are met. Hence, if $C_x = 1$ and the criteria are met the GA will exit out after twenty generations. All but the most restrictive T_x allow the convergence criteria at the earliest possible opportunity. When $T_x = 0.001\%$ and $C_x = 2$ the GM cluster is returned and the GA program exited after 110 generations, where for $C_x = 5, 10$ the GA program runs until the maximum number of generations set. Even though the cluster remains geometrically unchanged in the main, the fluctuation in the MD from energy left in the calculation ensures that the convergence criteria are not met.

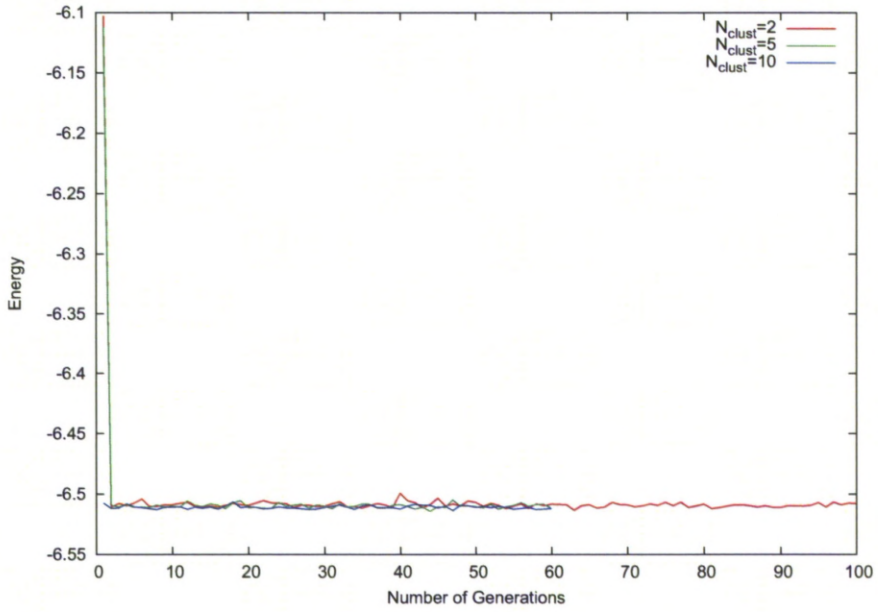

Figure 5.4: N=4 N_{clust} Energy comparison

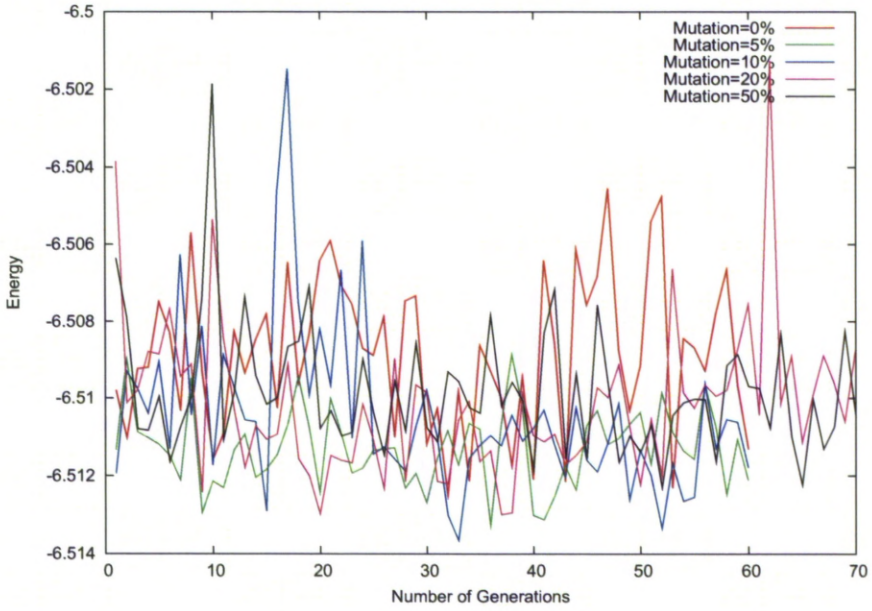

Figure 5.5: N=4 Mutation Parameter Energy comparison

5.3.2 N=5

Figure 5.6: N=5 GM Cluster

Figure 5.7: N=5 GM Cluster

We have no means for comparison to the work of Kabrede, Michaelian and Ayuela when looking at odd numbered clusters since they only evaluated even numbered clusters. The calculations will offer insight here into the arrangement and stoichiometry of all odd numbered clusters and how the total energy compares to that of even number clusters.

Figures 5.6 and 5.7 show two GM clusters. Their arrangement is the same with five ions arranged linearly alternating atom type along the line. The difference between the two being the stoichiometry with two Na ions and three Cl ions in 5.6 and three Na ions and two Cl ions in 5.7.

As shown for N=4 the energy plots looking at the variance of N_{clust} and the P_{mut} show that the GM is reached after the first generation. All but, $N_{clust} = 2$ and $P_{mut} = 20\%$ show the convergence criteria met at the earliest possible opportunity. This is due to the MD as explained earlier and looks more prominent for $N_{clust} = 2$ since the lowest energy cluster is recorded at each generation. The more clusters in the population then the less the fluctuation will be prevalent in the energy plot since there is increased chance that a cluster will occur with an energy at the lower region of the MD fluctuations.

Again, all but for $T_x = 0.001\%$ we see the convergence criteria met at the earliest opportunity. When $C_x = 2$ there are 150 generations with the maximum number of generations used when $C_x = 5, 10$.

5.3.3 N=6

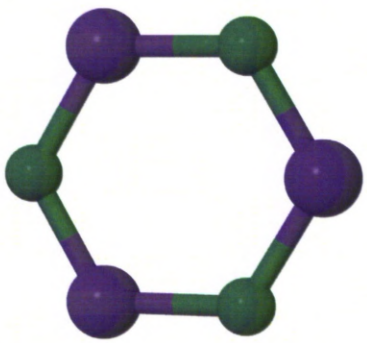

Figure 5.8: N=6 GM Cluster

The hexagonal structure consisting of three Na ions alternating with three Cl ions (figure 5.8) is also predicted by Ayuela, Michaelian and Kabrede. This GM structure is the only structure output across all variety of parameters tested.

When evaluating the change of energy development with N_{clust} we see similarities to N=5 with $N_{clust} = 5, 10$ exiting at the earliest possible opportunity, but $N_{clust} = 2$ needing 110 generations despite all being in the GM from the first generation. We see evidence of local minima for N=6 in figure 5.9 with $P_{mut} = 0\%$ showing two local minima at approximately -7.5Ha and 9.6Ha before settling into the GM after five generations. For all other P_{mut} values tested the GM was found after

the first generation. Since the GM was found before the first convergence check at the tenth generation the convergence criteria were still met at the earliest opportunity.

Once again we see more generations needed when $T_x = 0.001\%$ with 310 needed for $C_x = 2$ and the maximum number otherwise. We also see the need for 200 generations when the GA is ran with a $T_x = 0.01\%$ and $C_x = 10$.

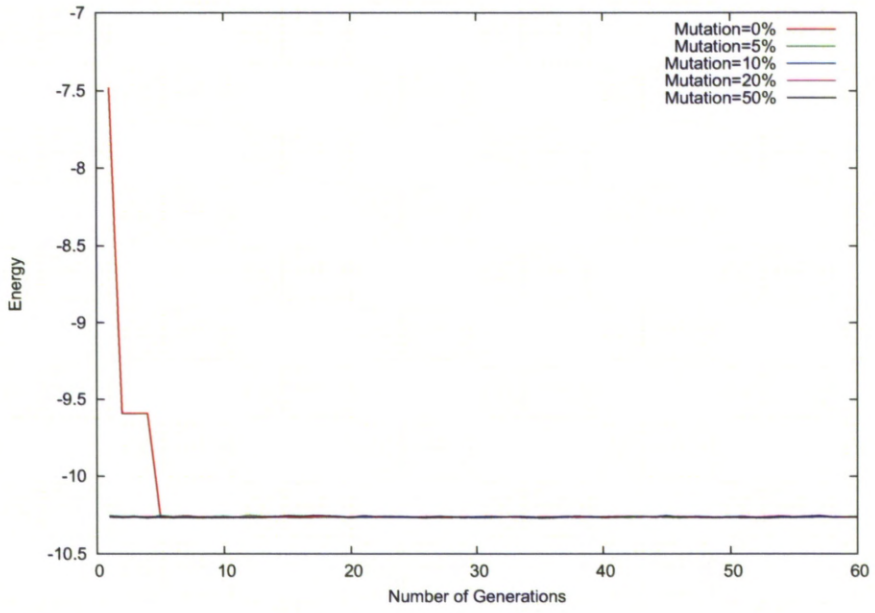

Figure 5.9: N=6 Mutation Parameter Energy comparison

5.3.4 N=7

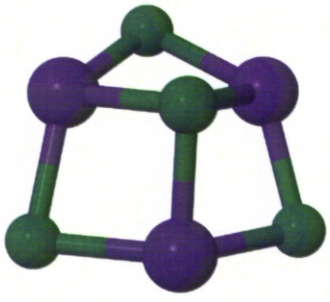

Figure 5.10: N=7 GM Cluster

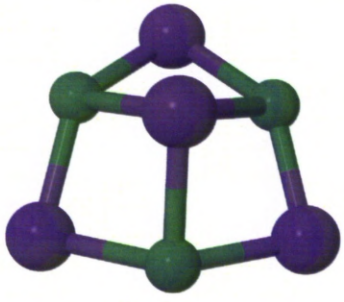

Figure 5.11: N=7 GM Cluster

For N=7 we see two GM structures formed (figures 5.10 and 5.11) and one local minimum structure (figure 5.12). The two GM structures are distorted cubic

Figure 5.12: N=7 Local Minimum Cluster

structures with a missing ion. In 5.10 we have three Na ions and four Cl ions, with four Na ions and three Cl ions in 5.11. The local minimum structure (figure 5.12) found from the GA is a curved line of four Na ions and three Cl ions.

The local minimum structure was produced when $N_{clust} = 2$ as shown in figure 5.13. $N_{clust} = 5$ and $N_{clust} = 10$ existed in this local minimium state for 21 and 2 generations respectively. This highlights the need for a higher value of N_{clust} for N=7 to ensure the GM is found. Because of the longer time needed when $N_{clust} = 5$ to find the GM an extra 20 generations are needed compared to $N_{clust} = 10$.

In figure 5.14 we see the same local minimum and ultimately GM present with the cluster staying longer in the local minimum for $P_{mut} = 10\%$ staying there for 18 generations. Consequently this cluster requires an extra ten generations before the convergence criteria are met.

As previously we see $T_x = 0.001\%$ and $C_x = 5, 10$ producing the need for the maximum number of generations and $C_x = 2$ requiring 130 generations. 40 and 70 generations, an extra 10 generations from the minimum, were required for $C_x = 2, 5$ respectively when $T_x = 0.05\%$.

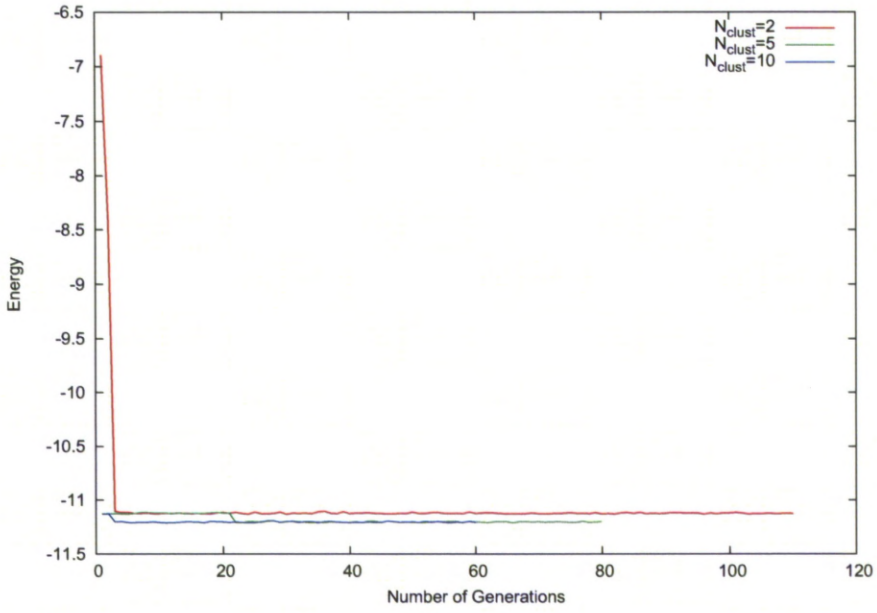

Figure 5.13: N=7 N_{clust} Energy comparison

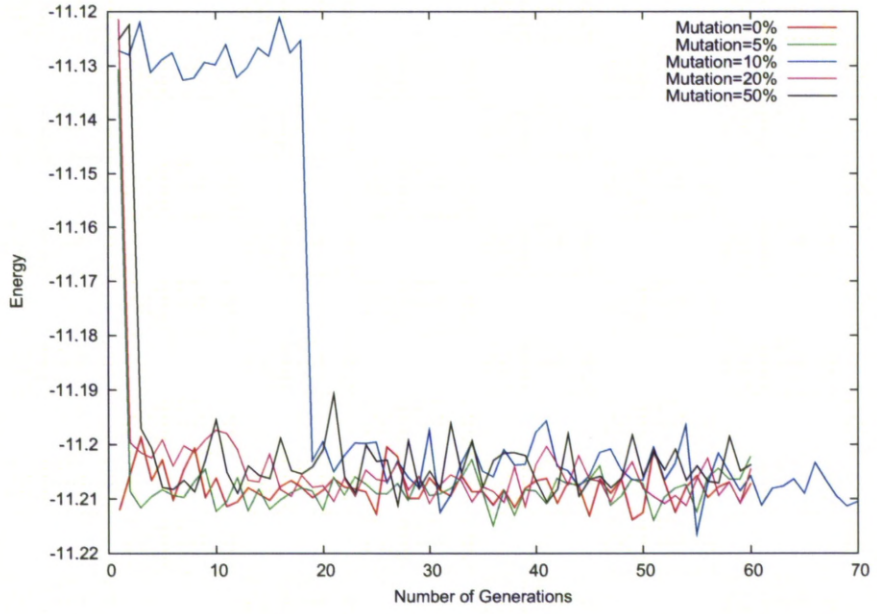

Figure 5.14: N=7 Mutation Parameter Energy comparison

5.3.5 N=8

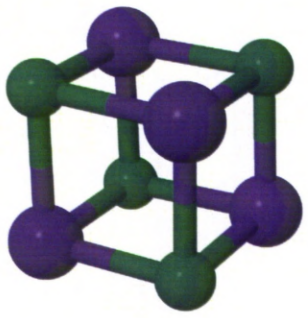

Figure 5.15: N=8 GM Cluster

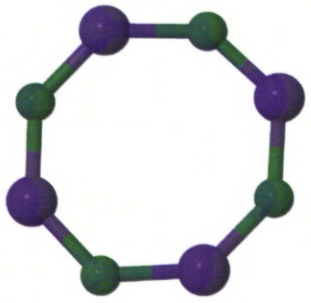

Figure 5.16: N=8 Local Minimum Cluster

For N=8 we obtain the GM for all but two of the GA runs. Figure 5.15 shows the GM cluster which is a cubic structure consisting of four Na ions and four Cl ions. This structure was also predicted by Ayuela, Michaelian and Kabrede. One local minimum structure is also produced as seen in figure 5.16. The octagon structure seen here consisting of four Na ions and four Cl ions was predicted as the second lowest energy structure by Michaelian.

We see three local minimum structures evident when varying N_{clust} shown at approximately -10.8Ha, -13.1Ha and -13.9Ha (figure 5.17). For all calculated values of N_{clust} we see them spend time as the hexagon structure, with the least time spent as this structure for $N_{clust} = 10$ (8 generations). For $N_{clust} = 2$ it stays as the octagonal structure throughout never evolving into the lower energy cubic structure. The inadequacy of low values of N_{clust} as we increase N is further highlighted here.

Figure 5.18 shows the GM and the octagonal local minima cluster which $P_{mut} = 0\%$ settles into. The question of needing P_{mut} to help maintain diversity can be raised here with all other P_{mut} values allowing the cluster to evolve into the GM.

We see further evidence of the restrictive $T_x = 0.001\%$ parameter with $C_x = 5, 10$ needing the maximum number of generations and $C_x = 2$ needing 70 generations. Although, with these parameters resulting in many more generations and therefore being more computationally expensive it can serve as a check that the cluster does

not reduce its energy further in the scenarios with fewer generations.

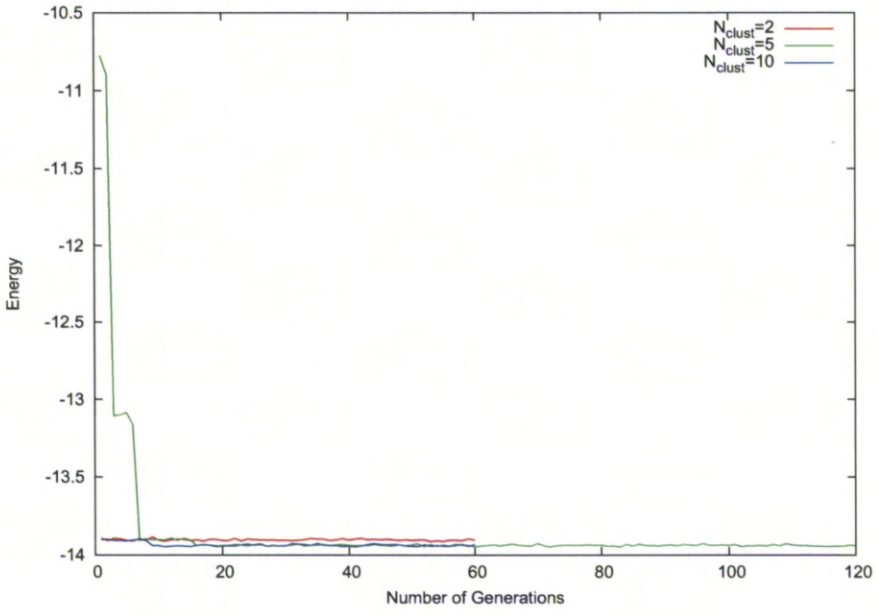

Figure 5.17: N=8 N_{clust} Energy comparison

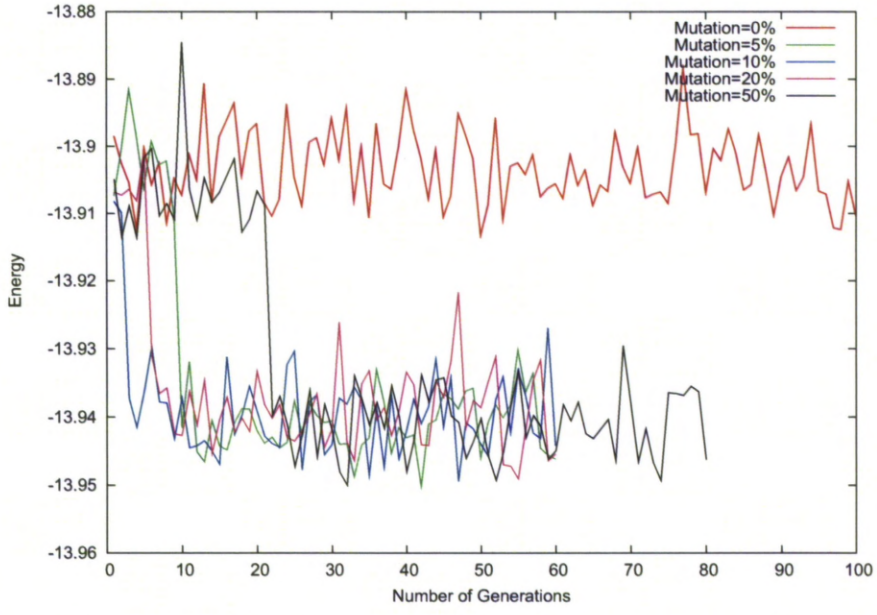

Figure 5.18: N=8 Mutation Parameter Energy comparison

5.3.6 N=9

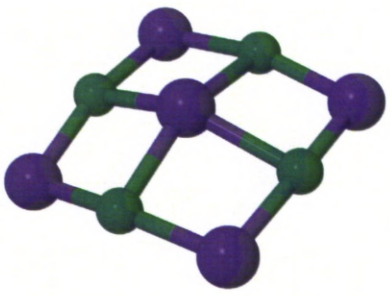

Figure 5.19: N=9 GM Cluster

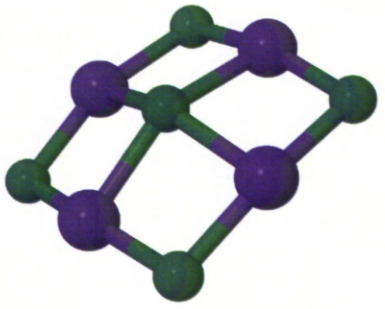

Figure 5.20: N=9 GM Cluster

As per other odd values of N we see two GM clusters which here are both curved sheets with figure 5.19 consisting of five Na ions and four Cl ions; and figure 5.20 consisting of four Na ions and five Cl ions. No local minima were produced here at the end of a GA run.

When evaluating the change of N_{clust} we see one intermediate local minimum (at approximately -14.68Ha) which exists briefly for all N_{clust} values calculated, before evolving to either GM state. The minimum number 60 generations are used for $N_{clust} = 5, 10$ with an extra 50 generations required for $N_{clust} = 2$.

We see an extra local minimum cluster around -14.65Ha when $P_{mut} = 0\%$. As above, the local minima clusters only exist briefly before evolving to the GM states with all calculated values of the P_{mut} parameter requiring the minimum number of generations for set variables.

For $T_x = 0.01\%$ and $C_x = 5$ and extra 20 generations is required from minimum to exit with the GM cluster. The maximum number of generations are required for $T_x = 0.001\%$ and $C_x = 5, 10$ with 550 generations needed for $C_x = 2$.

5.3.7 N=10

We see two structures formed from the GA for N=10. Both of these structures are energetically very similar, with the lowest energy for the structure in figure 5.21 being -17.51262Ha and -17.51153Ha for figure 5.22. Both structures contain equal numbers of Na and Cl ions with figure 5.21 being a distorted cubic with two ions

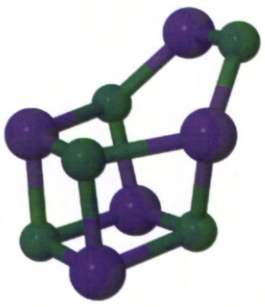

Figure 5.21: N=10 GM Cluster

Figure 5.22: N=10 Local Minimum Cluster

forming a 'handle' to the cube. Figure 5.22 shows a cluster ring. Upon comparison with the literature we see these two structures being prominent. Kabrede predicts the structure seen in 5.21. Michaelian also predicts this structure as the GM, but also found the cluster in 5.22 as a local minima. Whereas, Ayuela found the cluster in 5.22 to be the ground state geometry.

We can see how close the structures shown above are in energy with the ring cluster being found with $N_{clust} = 2$ in figure 5.23 and the 'cube and handle' structure being found $N_{clust} = 5, 10$. There are extra local minima states found for $N_{clust} = 2, 5$ for earlier generations.

With fewer local minima states present in earlier generations when investigating the P_{mut} parameter we are able to see the MD fluctuations close up. For $P_{mut} = 20\%$ the ring structure is returned as the optimal cluster. No energy difference is observed for this when compared to the other four values in figure 5.24, showing how energetically similar the two clusters are.

When setting $T_x = 0.01\%, 0.05\%, 0.1\%$ the minimum number of generations are needed to find the ground state energy; but for $T_x = 0.001\%$ we have 240 generations for $C_x = 2$, 770 generations for $C_x = 5$ and the maximum allowed (2000 in this case) for $C_x = 10$. Reducing the temperature in the MD algorithm as time increases may help us distinguish between structures.

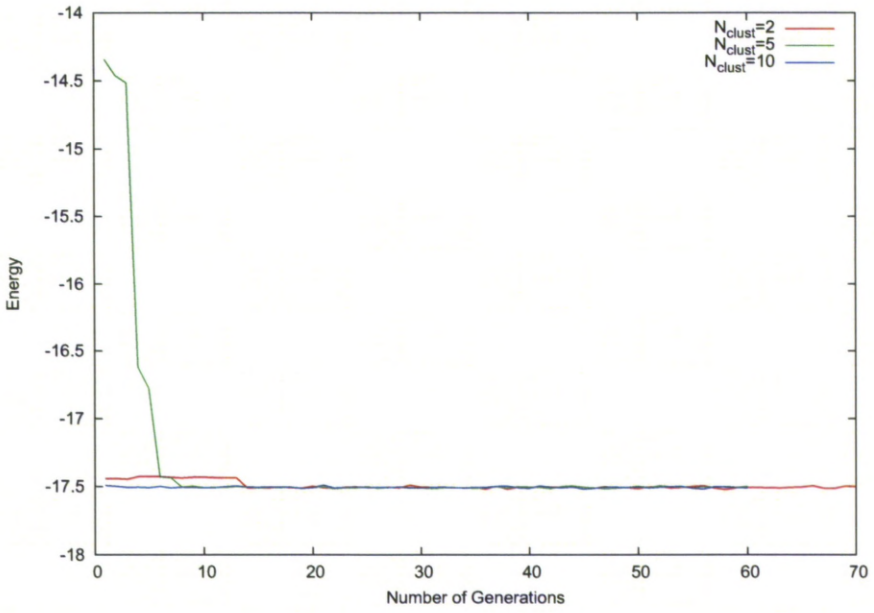

Figure 5.23: N=10 N_{clust} Energy comparison

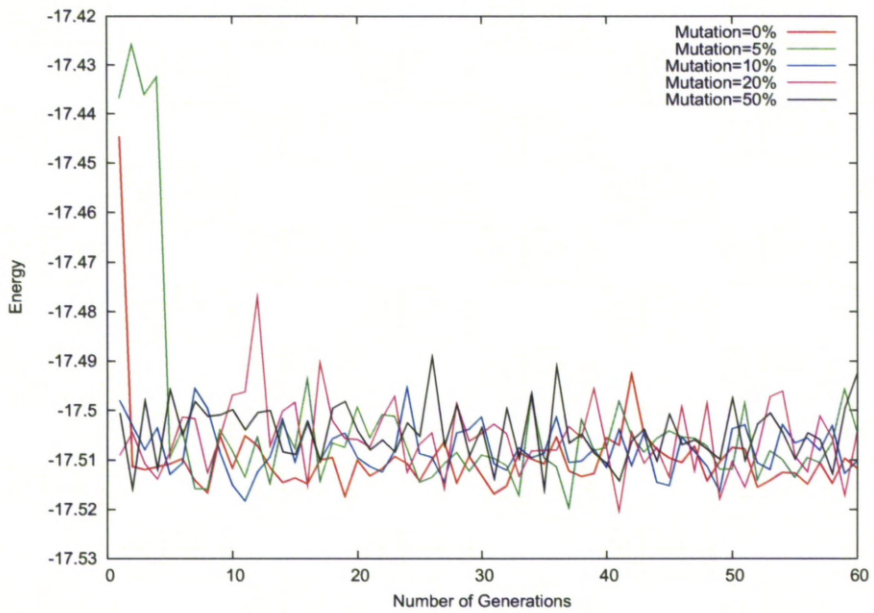

Figure 5.24: N=10 Mutation Parameter Energy comparison

5.3.8 N=11

Figure 5.25: N=11 GM Cluster

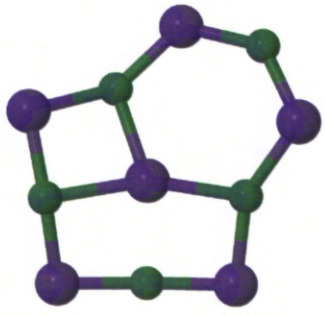

Figure 5.26: N=11 GM Cluster

Different stoichiometries are present for the two GM clusters as seen in figures 5.25 and 5.26 with both having the same geometry of three 'squares' connected to a hexagon. There are five Na ions and six Cl ions in 5.25; and six Na ions and five Cl ions in 5.26.

For the three values of N_{clust} calculated there are more generations than the minimum allowed with 130 generations for $N_{clust} = 2$ and 100 generations for $N_{clust} = 5, 10$. There are three local minimum clusters evolved in earlier generations as seen in figure 5.27 at approximately -14Ha, -17.5Ha and -18.2Ha. $N_{clust} = 2$ takes the longest number of generations to evolve to the GM taking 31 generations to do so.

With N_{clust} fixed at ten when investigating the variance of the P_{mut} parameter we achieve faster convergence to the GM, with only $P_{mut} = 20\%, 50\%$ not finding the GM within the first generation.

A higher than minimum number of generations is witnessed for $T_x = 0.01\%$ and $C_x = 10$ with 150 generations (40 more than the minimum allowed). As previously $T_x = 0.001\%$ gives larger number of generations with 90 when $C_x = 2$, 390 when $C_x = 5$ and the maximum 2000 when $C_x = 10$.

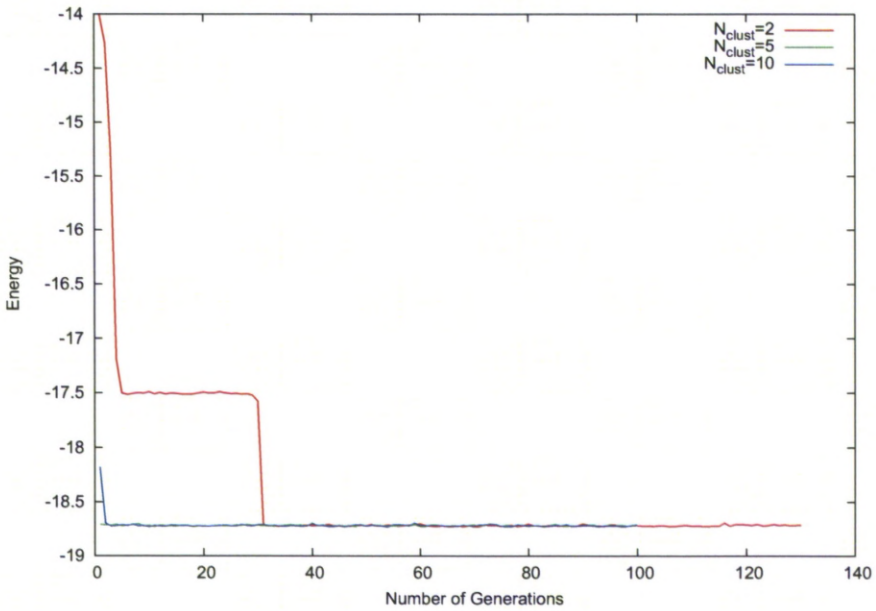

Figure 5.27: N=11 N_{clust} Energy comparison

5.3.9 N=12

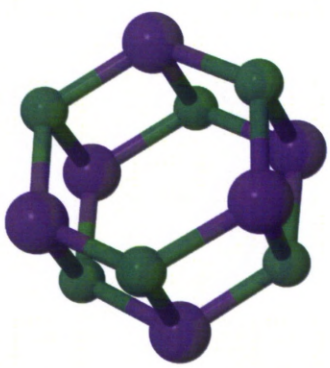

Figure 5.28: N=12 GM Cluster

As previously predicted by Ayuela, Michaelian and Kabrede the GM structure as seen in figure 5.28 consists two parallel hexagons each with equal numbers of each ion type.

Two local minima are present in the N_{clust} calculations at approximately -18.5Ha and -21.1Ha. Both $N_{clust} = 5$ and $N_{clust} = 10$ both evolve into the GM cluster by the tenth generation allowing the convergence criteria to be met by the 60th

generation. The GM cluster only became evident for $N_{clust} = 2$ in the 60th generation and therefore just about saving this parameter set from yielding a local minima as the GA's final cluster.

The large amount of mutation when $P_{mut} = 50\%$ gives an extra 30 generations for the convergence criteria to be met despite itself and all other P_{mut} values being in the ground state energy range before the tenth generation.

With a larger value of N, the number of local minima increase and therefore the convergence criteria is less likely to be met within it's minimum scale. $T_x = 0.1\%$ and $C_x = 5$ required ten extra generations before satisfied the GM cluster was found. Similarly with $T_x = 0.01\%$ and $C_x = 2, 5$. An extra 20 generations were required for $C_x = 2$ and $T_x = 0.001\%, 0.05\%$. The full 2000 generations were required for $T_x = 0.001\%$ and $C_x = 5, 10$.

5.3.10 N=13

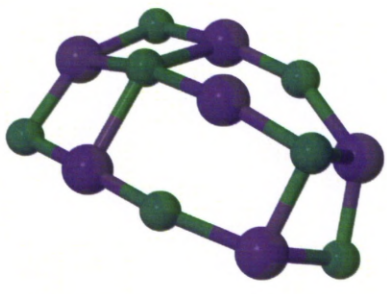

Figure 5.29: N=13 GM Cluster

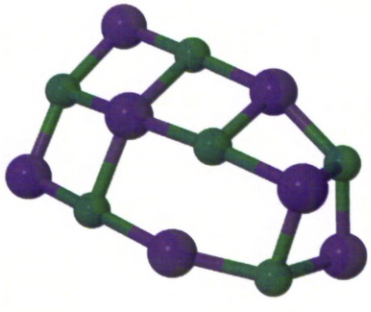

Figure 5.30: N=13 GM Cluster

The two GM clusters for N=13 can be described as a distorted cuboid with only three sides or that of a curved sheet. The two GM clusters have different stoichiometry with figure 5.29 six Na ions and seven Cl ions and figure 5.30 having seven Na ions and six Cl ions.

The effect of needing a larger value of N_{clust} as we increase N is more evident here with $N_{clust} = 10$ giving the GM state from the first generation and meeting the convergence criteria after 60 generations (figure 5.31). For $N_{clust} = 5$ the cluster evolves to the GM state after 11 generations and meets the convergence criteria

after 70 generations, whereas for $N_{clust} = 2$ the GM cluster is discovered after 45 generations with the convergence criteria being met after 100 generations.

When evaluating the P_{mut} parameter since $N_{clust} = 10$ we reach the GM quicker with less local minima shown in the whole process. All but $P_{mut} = 0\%$ and $P_{mut} = 5\%$ we see the convergence criteria being met at the earliest opportunity after 60 generations. With the GM structure being predicted even for the 'loosest' convergence criteria of $T_x = 0.1\%$ and $C_x = 2$ after only 40 generations then it is possible to run the GA for less generations as long as enough clusters in the population are present.

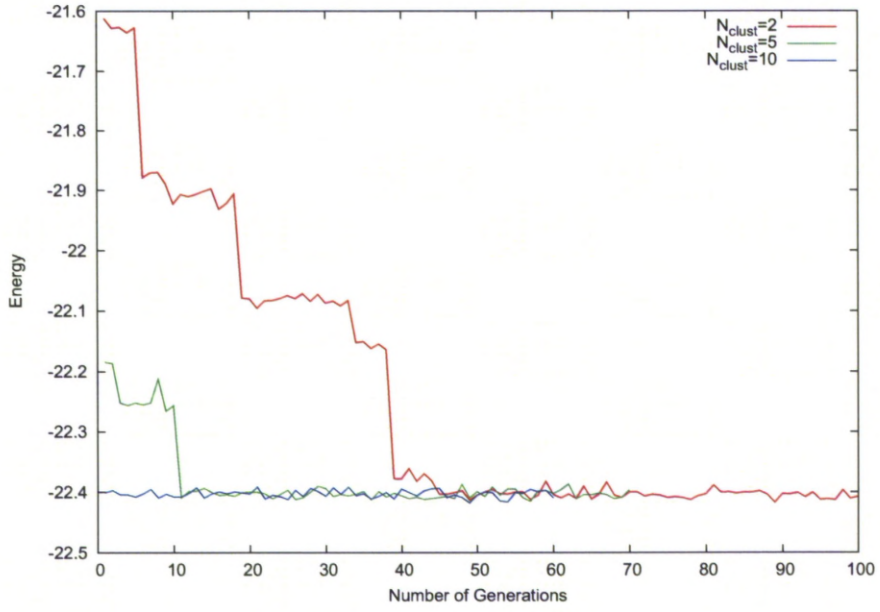

Figure 5.31: N=13 N_{clust} Energy comparison

5.3.11 N=14

When running the GA for N=14 we produce a GM cluster and two local minima upon output of final clusters. Figure 5.32 shows the GM cluster which shows two distorted hexagons which share one Na and one Cl ion with two of each ion type connected to these hexagons. This cluster matches the structure predicted by Kabrede, although the ground state cluster predicted by Ayuela is that of a cuboid shape. Michaelian only investigated clusters up until N=12. The highest energy cluster returned at the end of the GA was that in figure 5.33 which is

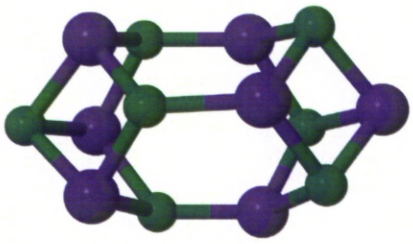

Figure 5.32: N=14 GM Cluster

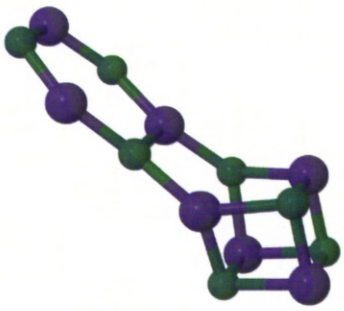

Figure 5.33: N=14 Local Minimum Cluster

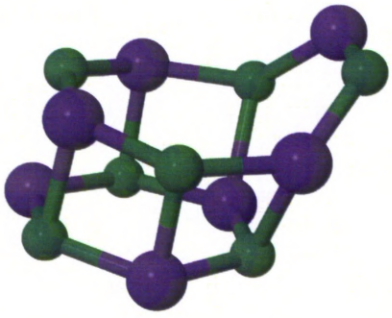

Figure 5.34: N=14 Local Minimum Cluster

a 'lawnmower' type shape with a cube and elongated 'handle'. In figure 5.34 a hexagon and a distorted octagon are produced parallel to each other.

The local minima shown in 5.33 is shown in figure 5.35 for $N_{clust} = 2$. The GM is predicted otherwise, although as can be seen the time taken to reach the GM takes longer than lower values of N_{clust} with 22 generations needed for $N_{clust} = 5$ and 41 generations for $N_{clust} = 10$.

This is reciprocated when evaluating the change in P_{mut} with no value of P_{mut} allowing for the minimum number of generations in the GA (60). The GM is predicted earliest when $P_{mut} = 10\%$ and latest for $P_{mut} = 50\%$.

Upon convergence check, $T_x = 0.001\%$ requires the maximum number of generations (2000) for $C_x = 5, 10$ and 180 generations for $C_x = 2$. 40 more generations than minimum is required for $T_x = 0.01\%$ and $C_x = 5$.

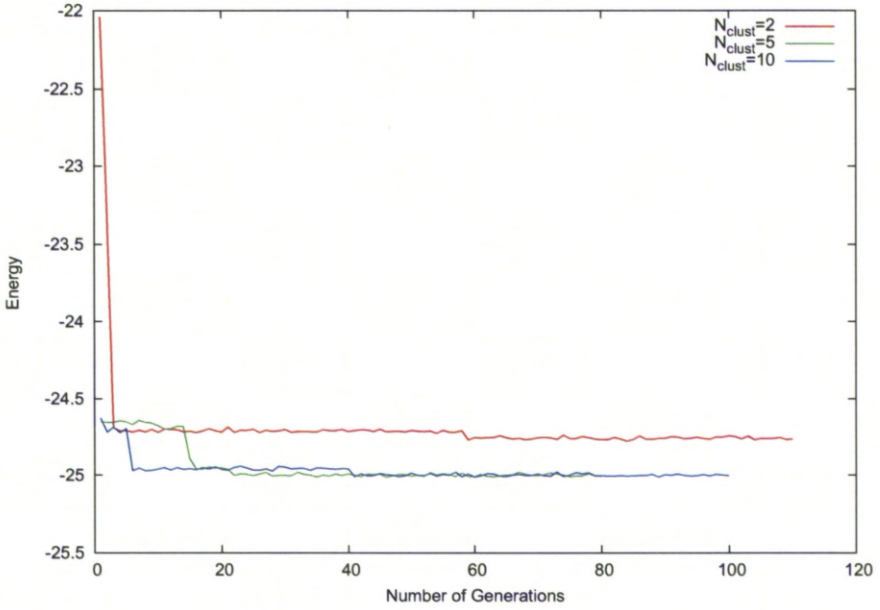

Figure 5.35: N=14 N_{clust} Energy comparison

5.3.12 N=15

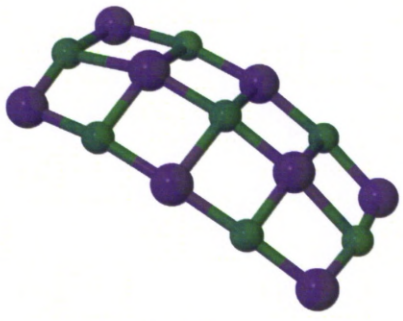

Figure 5.36: N=15 GM Cluster

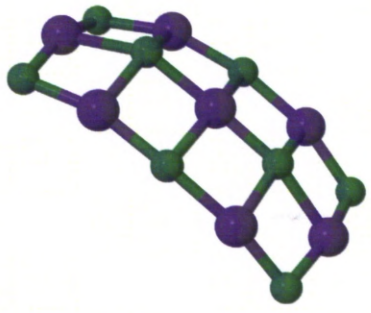

Figure 5.37: N=15 GM Cluster

Figures 5.36 and 5.37 show the two different stoichiometries providing us with a GM cluster. They both have similar geometries with a curved sheet being evident. In 5.36 we have eight Na ions and seven Cl ions; and in 5.37 we have seven Na ions and eight Cl ions. The local minimum found in 5.38 is only 0.05Ha different to the GM and exists as a cluster with three hexagonal faces surrounding a void.

The local minima in 5.38 and it's energetic proximity to the GM is highlighted in figure 5.39 with the local minima being predicted when $N_{clust} = 2$. $N_{clust} = 5, 10$ both predict the GM and meet the convergence criteria within the minimum number of generations possible.

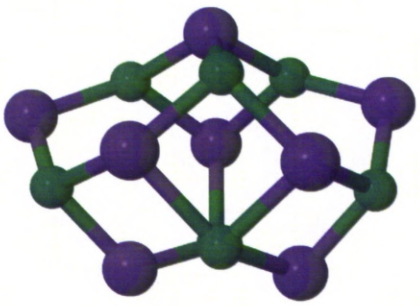

Figure 5.38: N=15 Local Minimum Cluster

In figure 5.40 the variance in the P_{mut} parameter and its effect on settling into the GM is shown with $P_{mut} = 0\%$ finding the GM earliest and $P_{mut} = 50\%$ showing more diversity by finding higher energy clusters. In previous work, P_{mut} is mentioned as something that is required to maintain diversity to help in the search for a ground state cluster. However, too large a P_{mut} parameter and it may create a longer time to find the GM structure. Although here for all P_{mut} values only 60 generations are required.

As previously, we require a higher number of generations for $T_x = 0.001\%$ with 300 required for $C_x = 2$ and the maximum number for $C_x = 5, 10$.

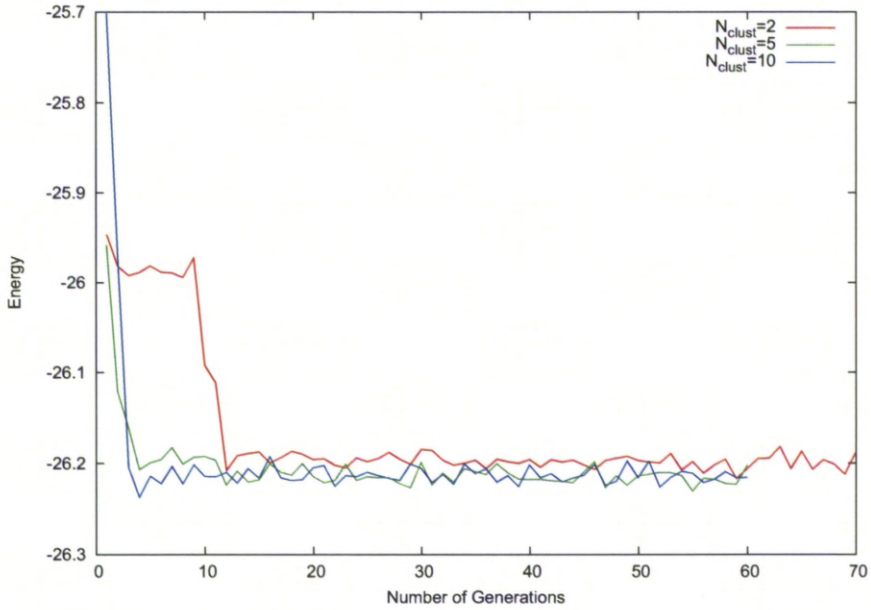

Figure 5.39: N=15 N_{clust} Energy comparison

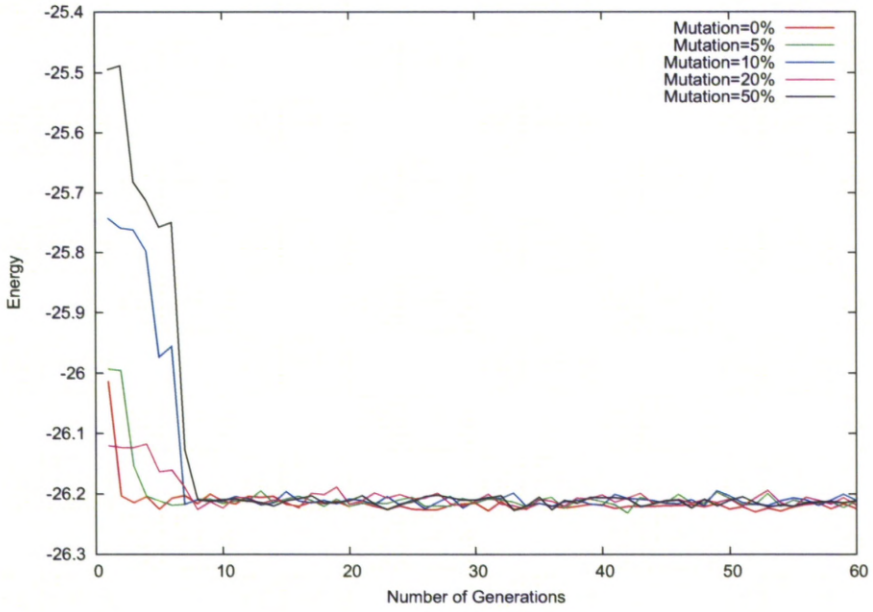

Figure 5.40: N=15 Mutation Parameter Energy comparison

5.3.13 N=16

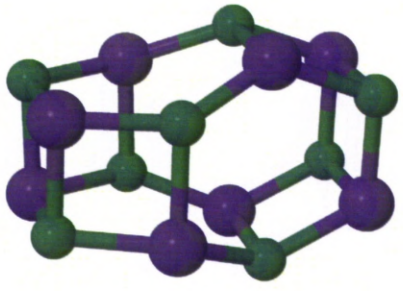

Figure 5.41: N=16 GM Cluster

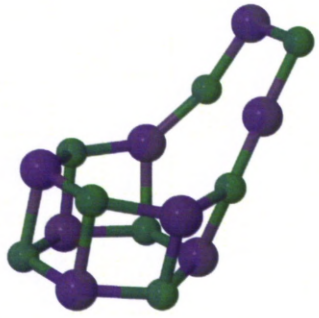

Figure 5.42: N=16 Local Minimum Cluster

For N=16 we see no agreement with Kabrede and Ayuela with them predicting a cuboid structure whereas we see a distorted cuboid structure in figure 5.41 with a hexagonal element to the cluster. There are also two local minima produced at the end of the GA with the parameters tested. One of which is shown in figure 5.42 which resembles the N=12 GM structure with an added four ions forming a 'handle'. The other local minima cluster was similar but with a more rectangular 'box' and a hexagonal handle.

Figure 5.43 shows the evolution of the clusters with respect to the number of clusters in the population. $N_{clust} = 10$ settles into the perceived GM cluster within a few generations. $N_{clust} = 5$ requires 33 generations and $N_{clust} = 2$ 38 generations. When investigating the P_{mut} parameter we see just $P_{mut} = 20\%$ requiring an extra ten generations above the minimum allowed.

More generations are required over and above the minimum allowed by convergence criteria for $T_x = 0.05\%$ and $C_x = 10$ and as expected for all values of C_x for $T_x = 0.001\%$.

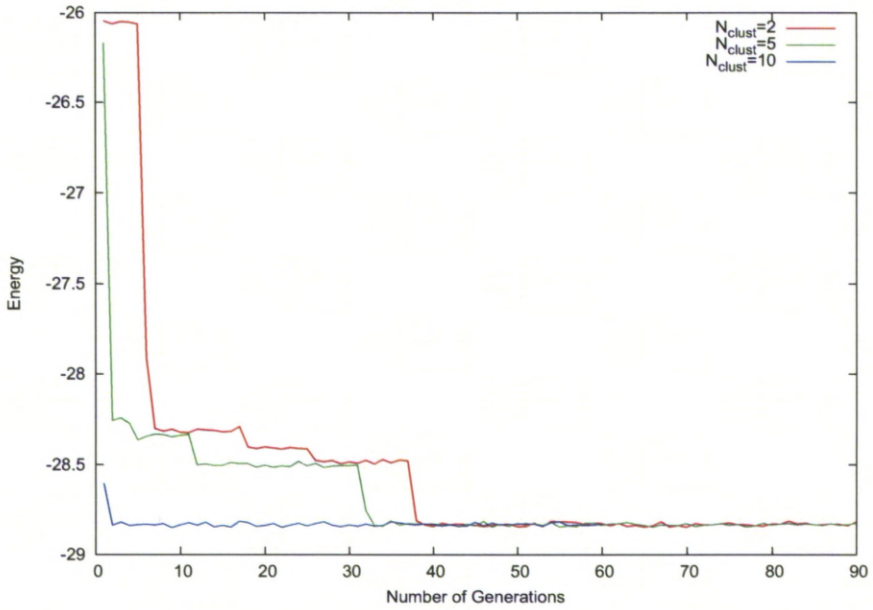

Figure 5.43: N=16 N_{clust} Energy comparison

5.3.14 N=17

For the GM clusters for N=17 we see two different stoichiometries containing a octagon above cubic arrangement of nine ions. In figure 5.44 the Na ion is at the centre of the nine atom cubic arrangement giving nine Na ions and eight Cl ions compared to the eight Na ions and nine Cl ions in figure 5.45.

When varying N_{clust} for N=17 we find two local minima states present before all values of N_{clust} reaching the GM. 30 generations are needed for $N_{clust} = 2$ to reach the GM, 21 generations for $N_{clust} = 5$ and 20 generations for $N_{clust} = 10$. Once

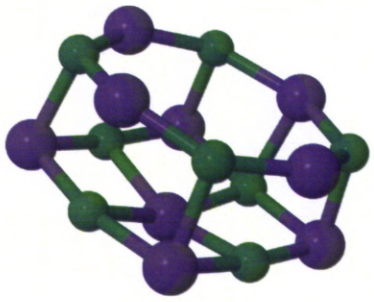

Figure 5.44: N=17 GM Cluster

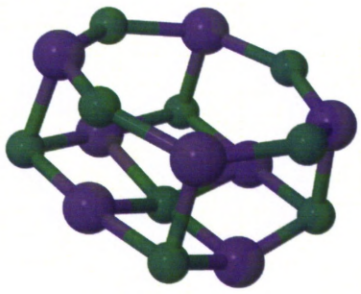

Figure 5.45: N=17 GM Cluster

again this highlights the dependence on N_{clust} of the ability and speed at which a cluster can evolve to the GM state.

When evaluating the effect of the P_{mut} parameter it shows $P_{mut} = 5\%, 50\%$ both requiring 60 generations with all other values requiring an extra 10 generations due to the speed at which each cluster evolved into either GM state. A local minima state exists at approximately -29.8Ha which was also the case when varying the value of N_{clust}.

130 generations, an extra 20 than minimum are required for the convergence criteria to be met for $T_x = 0.05\%$ and $C_x = 10$. The maximum amount of generations set are used for $T_x = 0.001\%$ and $C_x = 5, 10$ once again.

5.3.15 N=18

Only one structure is produced from the GA for N=18, that of the ground state energy. As represented in figure 5.46 it is a hexagonal based structure. This cluster geometry was also predicted by Ayuela and Kabrede.

Breaking the trend of smaller values of N we have $N_{clust} = 2$ evolving quickest into the GM state after just 14 generations. 54 generations and 46 generations are required before the GM cluster is seen in $N_{clust} = 5$ and $N_{clust} = 10$ respectively. There are six other local minimum present for these calculations represented by the plateaus in the plot of energy of the lowest energy cluster in the population against the number of generations.

The same local minima are observed on the whole with all values, except $P_{mut} =$

Figure 5.46: N=18 GM Cluster

5%, of the P_{mut} parameter existing for a time at a state of energy approximately -32.35Ha. $P_{mut} = 50\%$ finds another local minima state at approximately -32.6Ha which could highlight as previously seen that P_{mut} helps diversity in the population.

Despite the need for increased number of generations in the calculations when varying N_{clust} and P_{mut}, when investigating the effect of the convergence criteria there is only higher than minimum generations required for $T_x = 0.001\%$ with 280 generations for $C_x = 2$ and the maximum permitted for $N_{clust} = 5, 10$

5.3.16 N=19

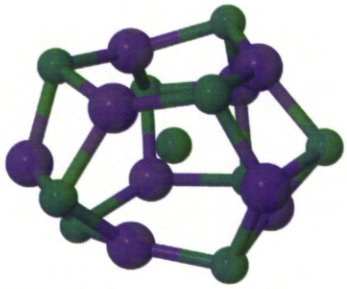

Figure 5.47: N=19 GM Cluster

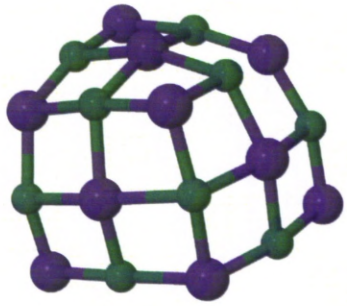

Figure 5.48: N=19 Local Minimum Cluster

The GM structure as shown in figure 5.47 is a cage with square and hexagon faces with a single Cl ion at the centre of the cage and consisting nine Na ions and

ten Cl ions. A local minimum that is also output from the GA is a curved sheet (figure 5.48). This cluster is that of the highest energy cluster produced at the end of the GA program studied within this chapter and consists of ten Na ions and nine Cl ions.

Two different energy states are witnessed for the final generation in figure 5.49 with the higher energy state existing when $N_{clust} = 5$. $N_{clust} = 10$ provides the quickest route to the lowest energy state, evolving into this state after 29 generations.

For all values of P_{mut} parameter investigated they all find the same energy state although they are approximately 0.02Ha above the lowest energy state found. The lowest energy state was found after the maximum number of generations allowed with convergence criteria of $T_x = 0.001\%$ and $C_x = 5$. The maximum number of generations was also required for $C_x = 10$ for the same T_x.

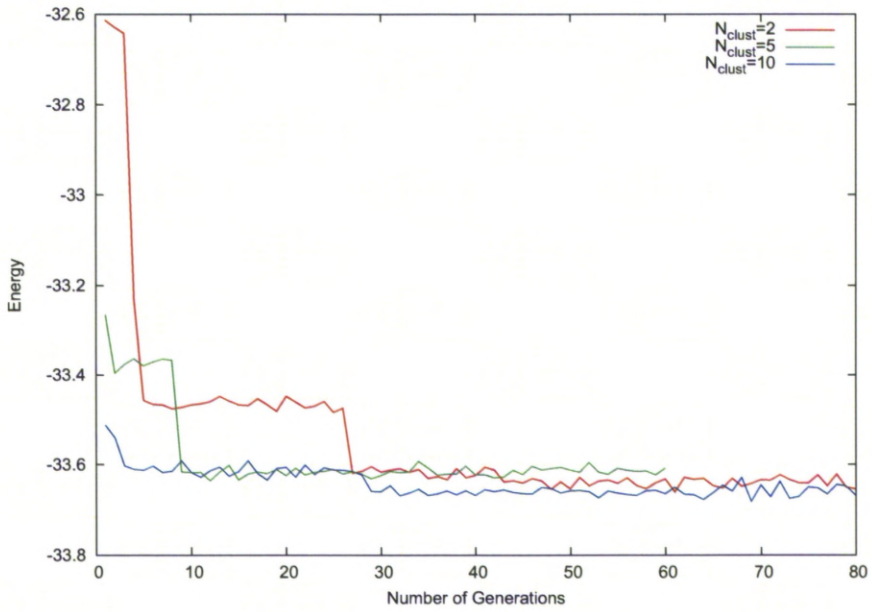

Figure 5.49: N=19 N_{clust} Energy comparison

5.3.17 N=20

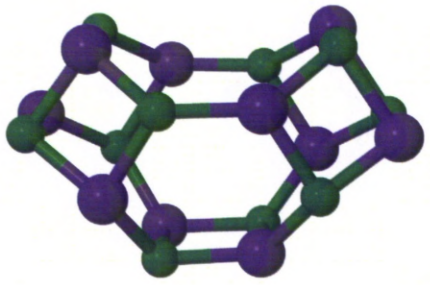

Figure 5.50: N=20 GM Cluster

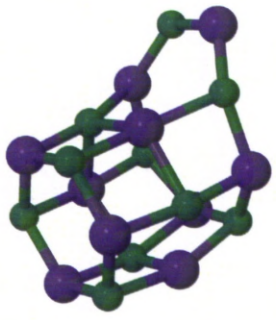

Figure 5.51: N=20 Local Minimum Cluster

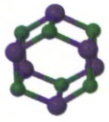

Figure 5.52: N=20 Local Minimum Cluster

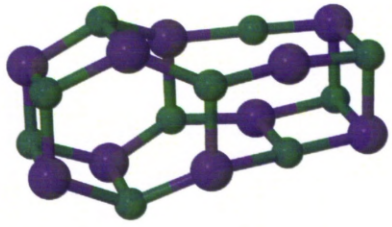

Figure 5.53: N=20 Local Minimum Cluster

Producing a single GM cluster and no local minima upon exiting the GA becomes more difficult as you increase N. For N=20 we see the majority of calculations yielding the GM cluster seen in figure 5.50 which does not match the cuboid structure observed by Ayuela and Kabrede. Three other local minima are witnessed in these calculations. Figure 5.51 shows a cubic structure with a hexgonal loop at one corner; figure 5.52 shows the structure splits into the N=12 GM cluster and a octagonal ring; and figure 5.53 exists as a four ion extension to the N=16 GM cluster.

Figure 5.53 is energetically similar to the GM cluster as shown in figure 5.54 where 5.53 is found for $N_{clust} = 5$ and the GM structure is found for $N_{clust} = 10$. $N_{clust} = 2$ produced the local minimum state illustrated in figure 5.52.

The local minimum state represented in figure 5.51 is illustrated energetically for

P_{mut} = 20% in figure 5.55. All other P_{mut} values result in the perceived GM cluster with P_{mut} = 50% the slowest of the P_{mut} values to settle into it's final state.

The least restrictive convergence criteria of $T_x = 0.05\%, 0.1\%$ exhibit no extra generations from minimum allowed. As previously though the maximum number of generations are required for $T_x = 0.001\%$ and $C_x = 5, 10$ with 70 generations needed for $C_x = 2$.

To be able to make a comparison to the work by Ayuela and Kabrede the cuboid structure found by them was input into the MD algorithm with the potential used in this thesis. This gave an energy of -36.205Ha which is less than the -36.218Ha found in the structure shown in figure 5.51 showing that the GA has found the most suitable GM with this potential.

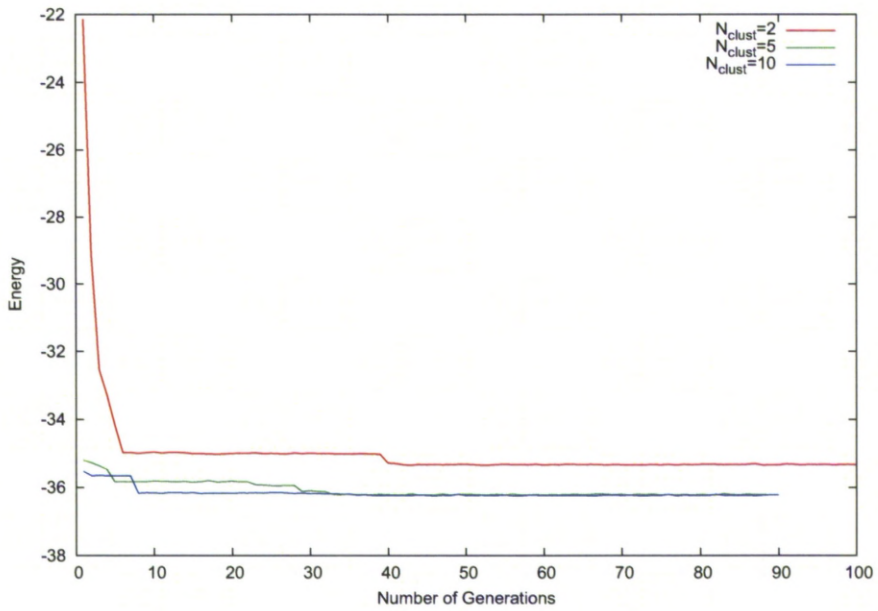

Figure 5.54: N=20 N_{clust} Energy comparison

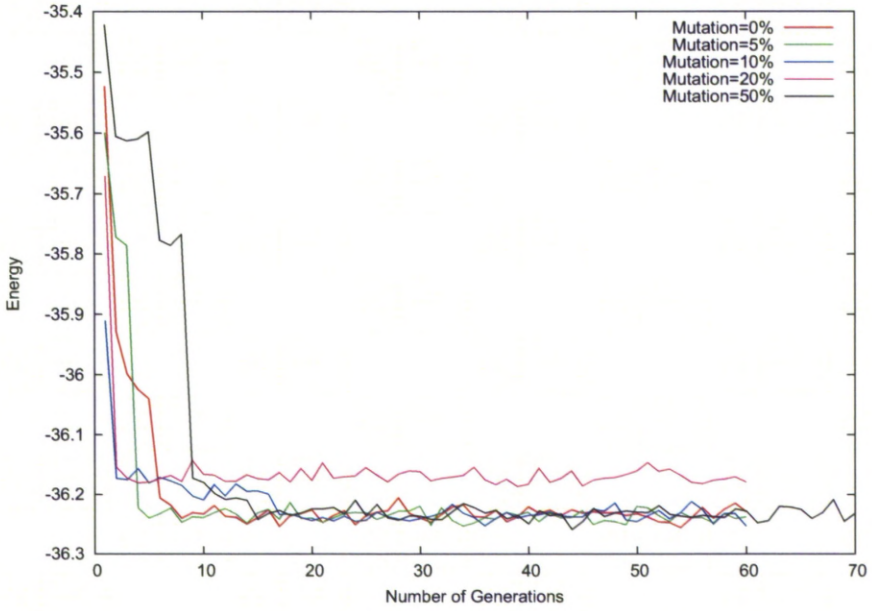

Figure 5.55: N=20 Mutation Parameter Energy comparison

5.3.18 N=30

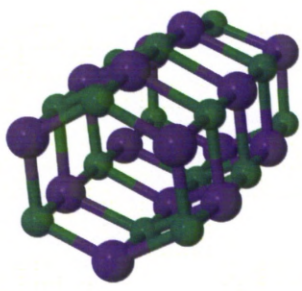

Figure 5.56: N=30 GM Cluster

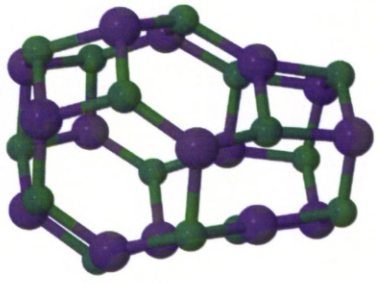

Figure 5.57: N=30 Local Minimum Cluster

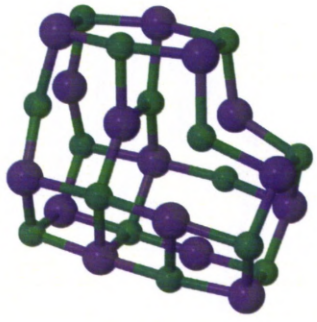

Figure 5.58: N=30 Local Minimum Cluster

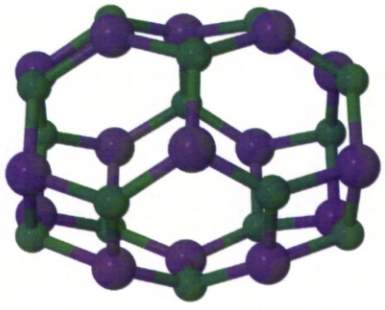

Figure 5.59: N=30 Local Minimum Cluster

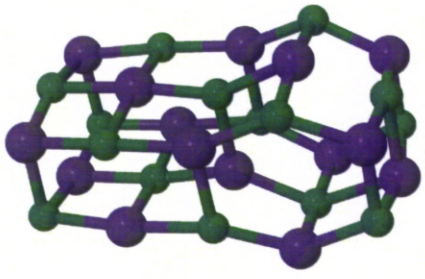

Figure 5.60: N=30 Local Minimum Cluster

For N=30 out of the twenty calculations investigating the different variables only four produced the GM cluster seen in figure 5.56. These were when investigating $P_{mut} = 0\%$; $N_{clust} = 10$; $T_x = 0.001\%$ and $C_x = 10$; and $T_x = 0.01\%$ and $C_x = 10$. This hexagonal based GM cluster was also predicted by Ayuela and Kabrede. The other local minima present upon final output of the GA program produced the clusters seen in figures 5.57, 5.58, 5.59 and 5.60 which contain hexagonal and cubic elements in the main and also elements of the clusters with a smaller value of N.

As represented with the variety of local minima clusters present this is confirmed in figures 5.61 and 5.62 which show the variation of N_{clust} and P_{mut} respectively. As mentioned above we see two GM clusters in these energy plots, but there are also plenty of local minima present with only $N_{clust} = 2$ and $P_{mut} = 50\%$ showing a small number of intermediary local minima energy steps.

The difficulty in the balance of selecting the correct convergence criteria is shown again with the most restrictive criteria i.e. T_x requiring the maximum number of generations allowed, whereas the least restrictive i.e. $T_x = 0.1\%$ only require the minimum number of generations.

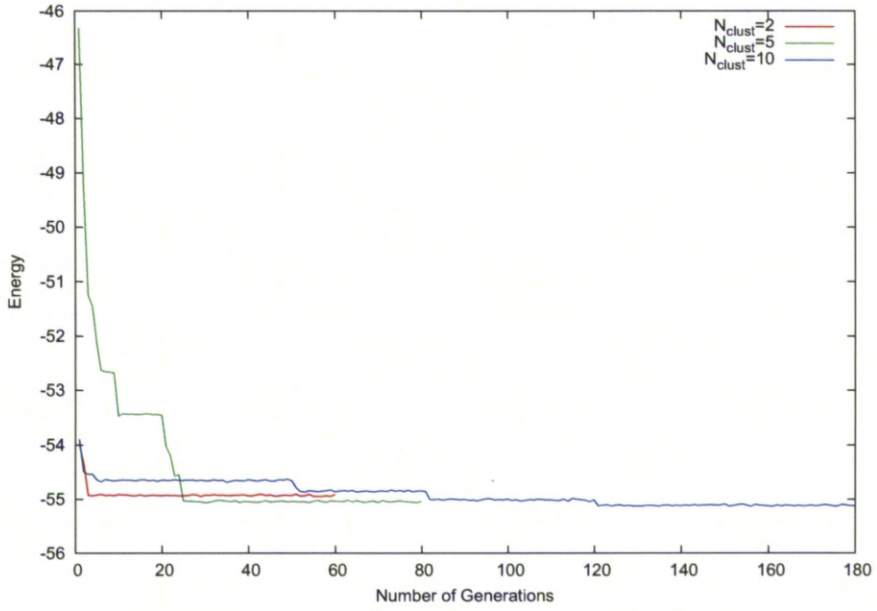

Figure 5.61: N=30 N_{clust} Energy comparison

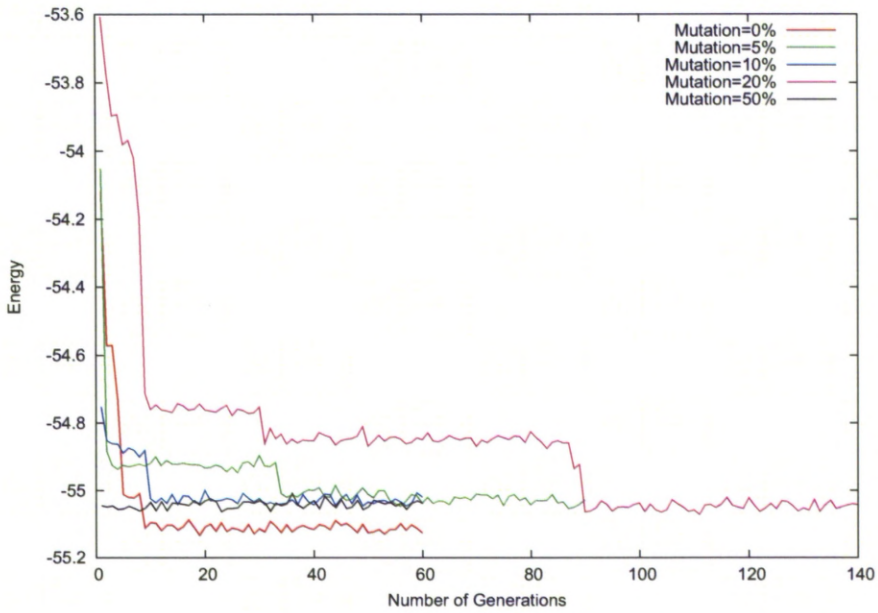

Figure 5.62: N=30 Mutation Parameter Energy comparison

5.3.19 N=40

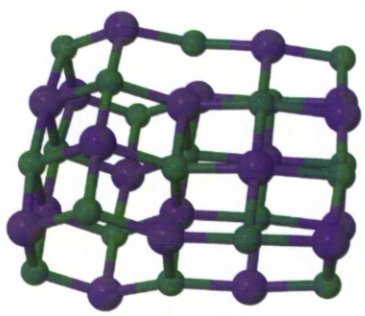

Figure 5.63: N=40 GM Cluster

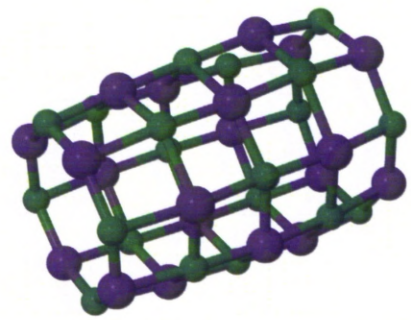

Figure 5.64: N=40 Local Minimum Cluster

With the increasing number of local minima present for N=40 only the two 'best' clusters are shown in figures 5.63 and 5.64. The GM cluster shows a hexagonal and cubic arrangement similar to that seen for N=16. Only Kabrede studied a cluster of size N=40 with a cubic structure predicted. This only differs to the GM here by the distorted hexagonal layer which if flattened to be cubic would match what Kabrede observed. The local minimum cluster shown is that of a hexagonal based structure. The GM cluster present here was only witnessed when investigating the effect of varying the P_{mut} parameter for $P_{mut} = 0\%$.

The presence of many local minima at intermediary steps and the final stage is once again illustrated in the energy plots in figures 5.65 and 5.66. $N_{clust} = 10$ settles down into the final energy state quickest although its final energy is higher to that of $N_{clust} = 2, 5$. $N_{clust} = 10$ represented the 'worst' cluster formed by GA over all the variables investigated. When varying the P_{mut} parameter we obtain four different local minima, with the fifth being the GM. This creates uncertainty about the reliability of the prediction of the GM for large N with the variance evident in the energy plots.

Aside from when $T_x = 0.001\%$ more generations than minimum are required only for $T_x = 0.01\%$ and $C_x = 10$.

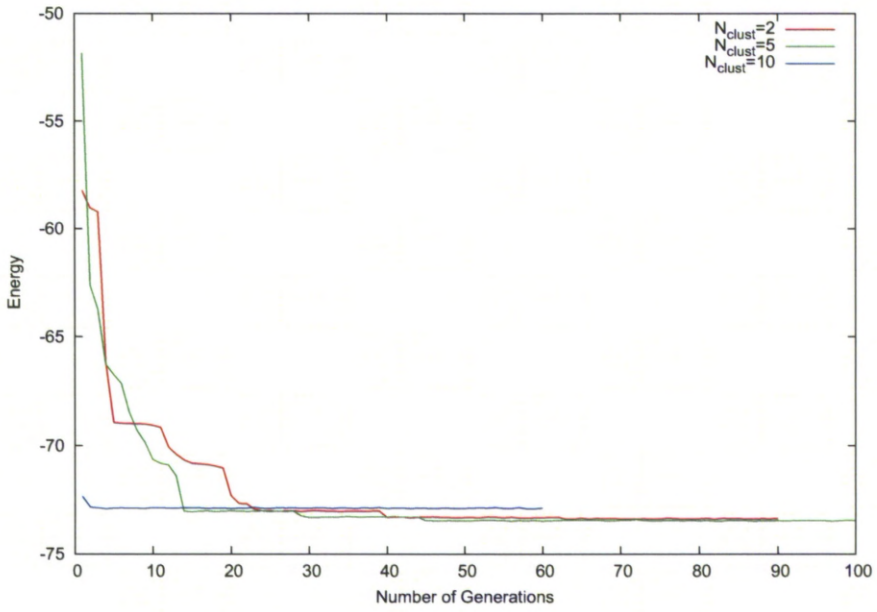

Figure 5.65: N=40 N_{clust} Energy comparison

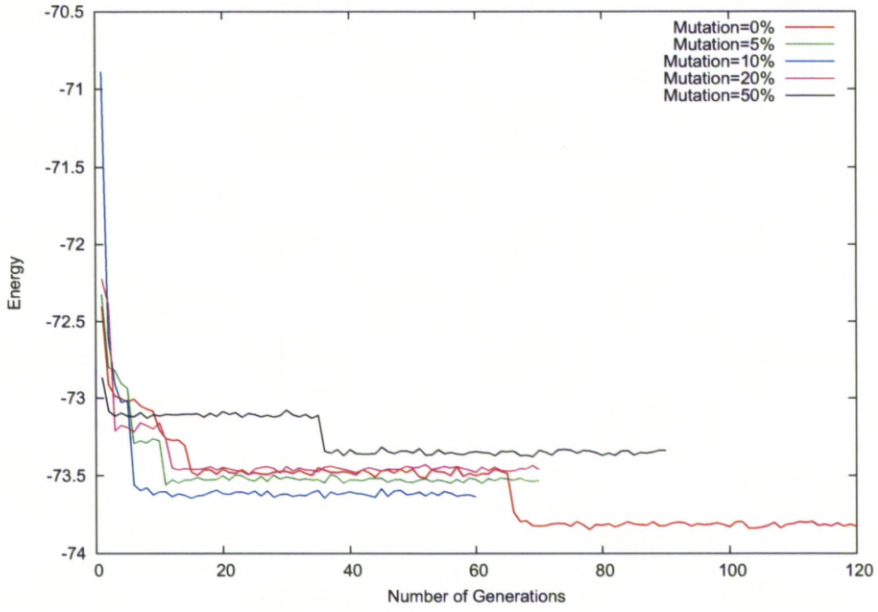

Figure 5.66: N=40 Mutation Parameter Energy comparison

5.3.20 N=50

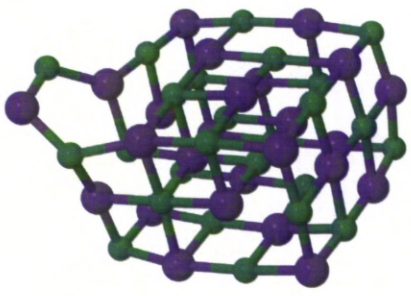

Figure 5.67: N=50 GM Cluster

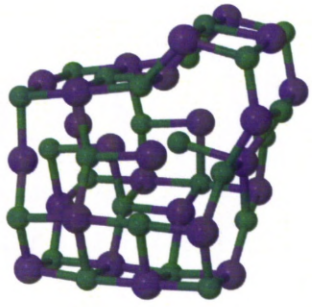

Figure 5.68: N=50 Local Minimum Cluster

As per N=40 only the two lowest energy structures are displayed in figures 5.67 and 5.68. Both of which are distorted from cubic form which is seen as the GM by Kabrede. We see the lowest energy and highest energy structures outputted differing by 0.7Ha. The intermediary and particularly the final stage local minima are evident in figures 5.69 and 5.70. The two lowest energy states found within this study existed when investigating the most restrictive convergence criteria with $T_x = 0.001\%$ and $C_x = 5, 10$ and is represented in figure 5.71. This shows that if

we we allow more generations then a lower energy state has more possibility to be found with changes in the cluster at much higher number of generations in other investigating other variables. Although, with an increased number of generations comes an increased computational expense.

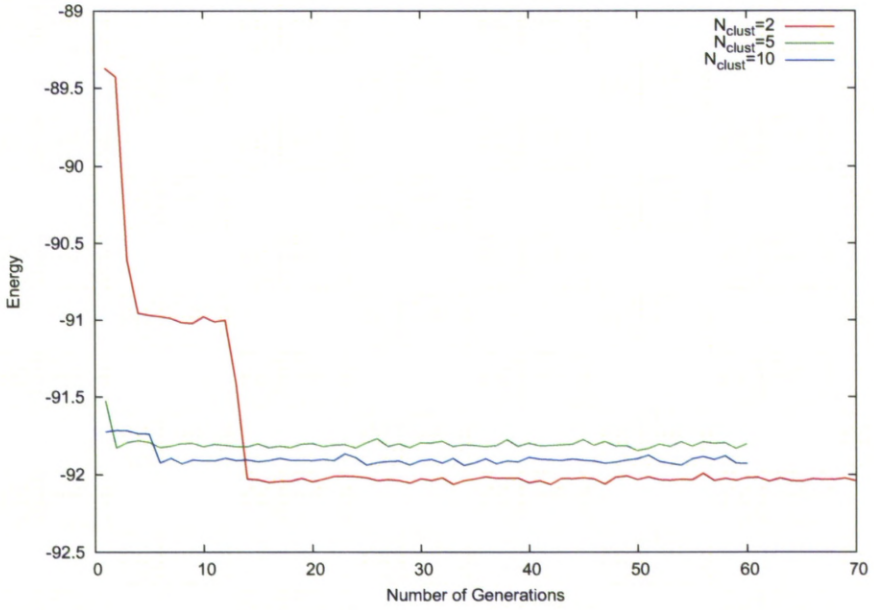

Figure 5.69: N=50 N_{clust} Energy comparison

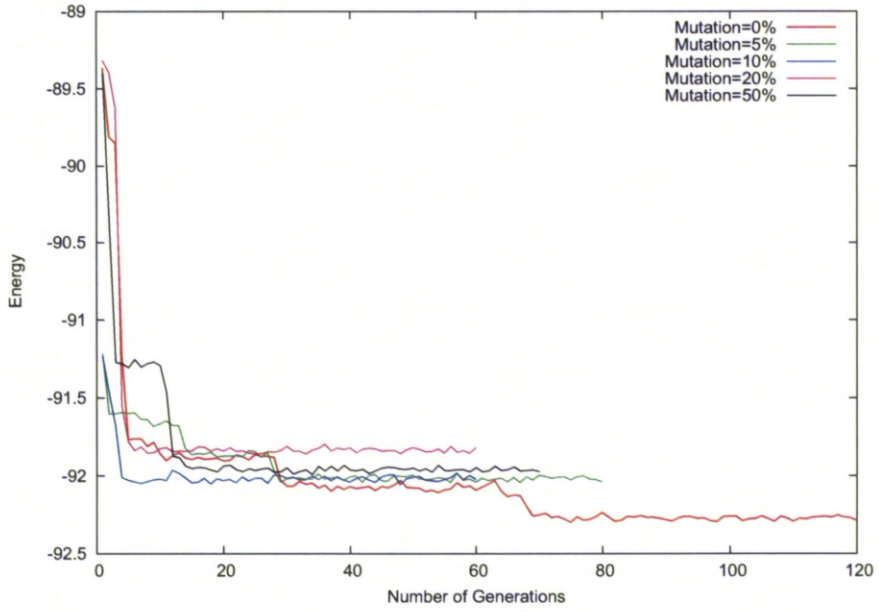

Figure 5.70: N=50 Mutation Parameter Energy comparison

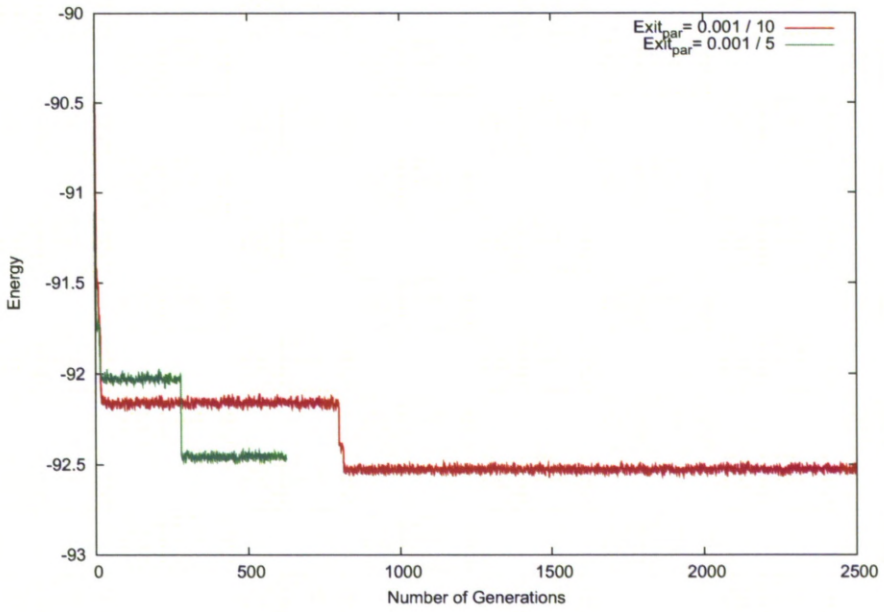

Figure 5.71: N=50 two lowest energy clusters

5.4 Conclusion

The investigations within this chapter show that a more primitive approach to the GA process can yield GM clusters as verified by the work of Ayuela, Michaelian and Kabrede. This primitive approach works best for a small number of ions i.e. N=4-30, but encounters more difficulties when we increase N beyond this point with the problematic increase of the number of local minima as we increase N.

However, when investigating the effects of the number of clusters in a population as we increased N_{clust} the suitability of $N_{clust} = 2$ despite being the computationally least expensive proved less successful in determining the ground state cluster. This could also be a factor, with $N_{clust} = 10$ being too small a number for higher N. Therefore as we increase N we need to increase the number of clusters in a population to help ascertain the GM cluster. This creates an exponential growth in the computational time required as we increase N further clarifying the need for a more primitive approach as highlighted within this chapter to maximise the output within current computational restrictions.

There was no evident preference of a set value for the P_{mut} parameter although in some values of N we saw a higher number of generations needed for $P_{mut} = 50\%$

with no evidence of it yielding any results differing from the other P_{mut} values. This also applied to $P_{mut} = 0\%$ showing that by having no mutation allowed it does not necessarily stop a cluster from evolving into its ground state. Although we do have an element of what P_{mut} provides by attempting to maintain diversity in the selection of the clusters with the probability of selecting the 'worst' two clusters for mating potentially more likely than selecting the first and third 'best' clusters.

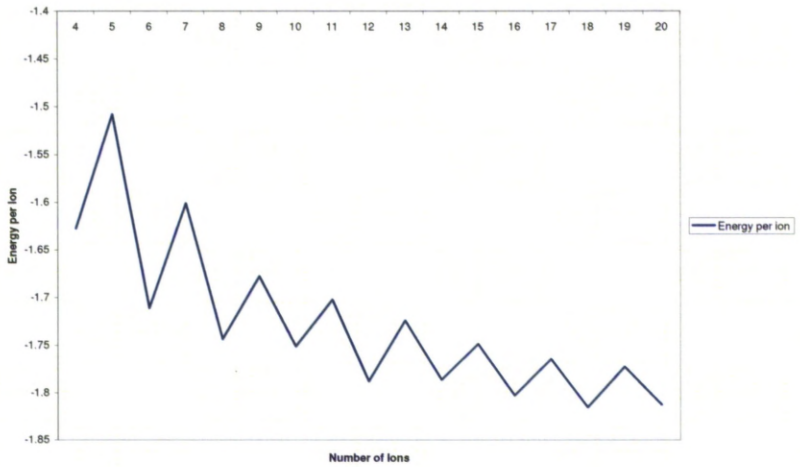

Figure 5.72: Energy per ion of the GM for N=4-20

Finally, we can compare the overall ground state energy of each value of N with respect to N. Figure 5.72 shows the Energy per Ion (Hartrees) for N=4-20. Here we see the odd numbers more energetically unstable with a higher ground state energy than their neighbouring values of N. The change in the ground state energy per ion as we increase N incrementally is larger for small values of N indicating that the clusters prefer to exist with a larger number of ions with this converging as we increase N with little energetic preference between N=18 and N=20 for example. This is because we are increasing the fraction of 'bulk' NaCl (which wants to be in the standard rock-salt structure) compared to 'surface' NaCl.

Chapter 6

Conclusion

"In applying calculations to these needs, a demonstration of success can rank, psychologically, with the example set by those who first climbed Everest." John Maddox [1]

Over the course of this thesis some approaches highlighted in the first chapter have been used to learn more about the materials involved, or in the case of chapter five, to develop a simplified Genetic Algorithm approach to materials design. We see successes in terms of achieving ground state structures, obtaining comparable results to experiment and using any data found to explain the nature of the structures. However, there are shortfalls that are highlighted along the way with some of these improved upon within this thesis. It is always important to be able to see the path for development and draw conclusions on any work. I will now provide a review of the results discovered in this thesis and identify some possible routes for future work on the topics that have been studied here.

6.1 Review of Results

Ruddlesden-Popper Layered Materials

The results illustrated in chapter three added further justification to back up the experimental observations of energetics and the development of the crystal structure as the number of layers is increased. As we increase n there is a reduction

in the value of c/n highlighting the contraction in the c axis as we increase n. The increase in octahedra and perovskite distortion as we increase n particularly for the 2×2×1 unit-cell for both GGA and GGA+U calculations further illustrates that the orthorhombic $CaMnO_3$ is the preferred structure for $CaMnO_3$, as previously known.

The distortion in perovskite layers can be reduced by doping the RP structure or by influencing the size of the lattice in the a and b directions with use of a substrate. This enables higher values of n to be formed.

Addressing the issue of the need for PLD for $n > 4$ the convergence of the binding energy per ion to the orthorhombic $CaMnO_3$ creates energetic similarities between $n > 4$. Therefore when using conventional synthesis methods to create higher n we could see multiple phases of the structures being present since the binding energies are similar. This occurred in experiment when $n = 3$ and the $n = \infty$ orthorhombic phases were formed when trying to form a $n = 4$ structure.

Chiral II-VI semiconductor nanostructure superlattices based on an amino acid ligand

Cd(L-cysteinate) (1) displays a local structure reminiscent of the rock salt phase of CdS, with an electronic structure and optical properties related to this CdS bulk phase. In Zn(L-cysteinate) (**2**), the local arrangement of the metal and sulphur atoms is a distorted 1D fragment of the bulk würtzite phase and the decrease of the ZnS system dimensions manifests itself by a blue shift of the absorption edge. The magnitude of the blue shifts observed in **1** and **2** is in agreement with the trends observed by decreasing dimensionality from bulk to 2D, then to 1D structures.

The density of states at the edge of the valence band in **1** is predominantly from p_S orbitals, while the DOS on the edge of the conduction band is essentially based on s_{Cd} orbitals. The contribution of atoms other than S on the edge of the valence band of **1** is extremely weak. This pattern is identical to that observed in both CdS bulk phases (würtzite and rock salt). A band edge optical transition (between p_S and s_{Cd} states) in **1** corresponds to a change in wavevector and thus needs to be phonon assisted, giving the indirect gap behaviour found for the high pressure

bulk CdS rock salt phase. This was different to the würtzite phase of CdS which displays a direct gap electronic structure. Note we get the correct contraction of the band widths due to less bonding in the molecular structure.

The density of states at the edge of the valence band in the optimised and unoptimised **2** is predominantly from p_S orbitals, while the DOS on the edge of the conduction band is essentially based on p_C and s_{Zn} orbitals. This is identical to that as observed in the ZnS bulk würtzite phase for Zn and S contributions. The 1D substructure remains constant from experiment in **2** with X-ray diffraction potentially not predicting the inter planar connections correctly.

As previously expected DFT underestimates the band gap, although it matches the key characteristics of gap type and atomic parentage shown by hybrid calculations albeit with more compact bulk states.

A simplified Genetic Algorithm approach to Materials Design

The GA method used within this thesis uses a more primitive approach and it is shown it can yield GM clusters as verified by the work of Ayuela, Michaelian and Kabrede. This approach works best for a small number of ions i.e. N=4-30, but encounters more difficulties when we increase N beyond this point with the problematic increase of the number of local minima as we increase N.

Using small numbers of clusters at each generation in the GA proved unsuitable with $N_{clust} = 2$ despite being the computationally least expensive proved less successful in determining the ground state cluster than higher values of $N_{clust} = 2$. This could also be a factor, with $N_{clust} = 10$ being too small a number for higher N. Therefore as we increase N we need to increase the number of clusters in a population to help ascertain the GM cluster. This creates an exponential growth in the computational time required as we increase N further clarifying the need for a more primitive approach as highlighted within this chapter to maximise the output within current computational restrictions.

There was no evident preference of a set mutation rate (P_{mut}) although with some values of N we saw a higher number of generations needed for $P_{mut} = 50\%$ with no evidence of it yielding any results differing from the other P_{mut} values. This also applied to $P_{mut} = 0\%$ showing that by having no mutation allowed it does

not necessarily stop a cluster from evolving into its ground state. Although we do have an element of what P_{mut} provides by attempting to maintain diversity in the selection of the clusters with the probability of selecting the 'worst' two clusters for mating potentially more likely than selecting the first and third 'best' clusters.

When comparing the overall ground state energy of each value of N with respect to N we see the odd numbers more energetically unstable with a higher ground state energy than their neighbouring even values of N. The change in the ground state energy per ion as we increase N incrementally is larger for small values of N indicating that the clusters prefer to exist with a larger number of ions with this converging as we increase N with little energetic preference between N=18 and N=20 for example. This is because we are increasing the fraction of 'bulk' NaCl (which wants to be in the standard rock-salt structure) compared to 'surface' NaCl.

6.2 Future Work

Ruddlesden Popper Layered Materials

The energetics and geometry of the $n = 1 - 6$ and $n = \infty$ cases were explored. There have been other studies into the magnetism of RP structures but only for low values of n. Future work would require analysis of the magnetism for larger n, namely in this case for $n = 4 - 6$. This would help provide us with a greater understanding of the nature and properties of the higher valued n which require PLD for formation. Particular consideration to adding in a STO substrate into calculations for $n > 4$ would be useful, but this would prove computationally expensive and would require many different calculations to investigate the substrate termination.

Chiral II-VI semiconductor nanostructure superlattices based on an amino acid ligand

A greater depth of work into the Zn(L-cysteinate) structure to potentially allow us to be able to identify the optimum structure and address whether the optimised structure seen here is a metastable state or simply achieved through inaccurate representation from experiment.

A simplified Genetic Algorithm approach to Materials Design

As expected this chapter provides us with the most open-ended problem. Further developments here would be to parallelise the GA enabling greater efficiency and enabling the successful study of higher N by being able to include more clusters in a population. An analysis of different types of mutations will allow a more detailed study into this simplified approach.

Ultimate Goal

In some aspects Maddox' challenge of predicting crystalline structures is starting to become more of a reality, but we are still yet to see a universal method that provides an *ab initio* approach. Although, if predicting crystalline structures from knowledge of chemical composition only is like climbing Everest, the ultimate goal, which would be a true *ex nihilo* approach, to predict structures according to their desired properties, would rank with walking on the moon.

Appendix A

Cd(L-cysteinate) bond lengths and angles

Table A.1: Comparison of selected Bond Lengths (Å) for experimental and theoretically optimised structure Cd(L-cysteinate)

Bond	Experimental	Optimised	% Change
Cd1a - S1a	2.95	3.06	3.73
Cd1a - S1b	2.60	2.63	1.15
Cd1a - S1c	2.71	2.72	0.37
Cd1a - O1	2.23	2.3	3.14
Cd1a - O2	2.46	2.47	0.41
Cd1a - N1	2.32	2.38	2.59
N1 - H1N	0.9	1.03	14.44
N1 - H2N	0.9	1.02	13.33
N1 - C2	1.45	1.47	1.38
O2 - C3	1.23	1.26	2.44
C3 - O1	1.27	1.28	0.79
C2 - C3	1.53	1.54	0.65
C2 - H2	0.98	1.1	12.24
C1 - C2	1.53	1.53	0.00
S1a - C1	1.82	1.84	1.10
C1 - H1B	0.97	1.1	13.40
C1 - H1A	0.97	1.1	13.40

Table A.2: Comparison of selected Angles (°) for experimental and theoretically optimised structure Cd(L-cysteinate)

Angle	Experimental	Optimised	% Change
S1a - Cd1a - O1	93.73	94.13	0.43
S1c - Cd1a - O1	89.64	90.88	1.38
S1b - Cd1a - O1	109.23	110.22	0.91
S1a - Cd1a - N1	72.63	71.16	-2.02
S1c - Cd1a - N1	100.12	100.53	0.41
S1c - Cd1a - O2	89.49	93.3	4.26
S1a - Cd1a - O2	79.8	77.84	-2.46
S1a - Cd1a - S1c	168.71	169.5	0.47
S1c - Cd1a - S1b	97.32	97.35	0.03
S1a - Cd1a - S1b	91.74	89.57	-2.37
O2 - Cd1a - O1	89.18	86.32	-3.21
N1 - Cd1a - O2	68.00	68.84	1.24
N1 - Cd1a - O1	154.87	153.04	-1.18
C1 - S1a - Cd1a	93.41	92.75	-0.71
C2 - N1 - Cd1a	107.98	107.52	-0.43
S1a - C1 - C2	114.31	114.37	0.05
C1 - C2 - C3	108.87	109.93	0.97
N1 - C2 - C3	110.19	111.05	0.78
N1 - C2 - C1	110.54	111.19	0.59
C2 - C3 - O1	113.87	114.34	0.41
C2 - C3 - O2	119.8	119.5	-0.25
O1 - C3 - O2	126.28	126.12	-0.13
C3 - O2 - Cd1a	110.79	112.49	1.53
Cd1a - S1c - Cd1c	168.71	169.5	0.47
Cd1a - S1c - Cd1b	87.88	90.03	2.45
Cd1a - S1b - Cd1b	83.06	83.05	-0.01

Appendix B

Zn(L-cysteinate) bond lengths and angles

Table B.1: Comparison of selected Bond Lengths (Å) for experimental and theoretically optimised structure Zn(L-cysteinate)

Bond	Experimental	Optimised	% Change
Zn1a - S1b	2.36	2.35	-0.42
Zn1a - S1a	2.37	2.37	0.00
Zn1a - O1	2.00	2.02	1.00
Zn1a - N1	2.06	2.08	0.97
N1 - H1A	0.92	1.03	11.96
N1 - H1B	0.92	1.03	11.96
S1a - C1	1.85	1.84	-0.54
C1 - H1	0.99	1.1	11.11
C1 - H3	0.99	1.09	10.10
C1 - C2	1.46	1.54	5.48
C2 - H2	1.00	1.10	10.00
C2 - C3	1.55	1.54	-0.65
N1 - C2	1.50	1.48	-1.33
C3 - O1	1.3	1.29	-0.77
C3 - O2	1.21	1.25	3.31

Table B.2: Comparison of selected Angles (°) for experimental and theoretically optimised structure Zn(L-cysteinate)

Angle	Experimental	Optimised	% Change
S1a - Zn1a - S1b	124.61	125.37 0.61	
S1a - Zn1a - O1	111.5	109.66	-1.65
S1a - Zn1a - N1	87.11	88.4	1.48
O1 - Zn1a - S1b	105.71	110.68	4.70
O1 - Zn1a - N1	125.02	117.16	-6.29
S1b - Zn1a - N1	103.63	104.04	0.40
Zn1a - S1a - C1	94.76	93.8	-1.01
Zn1a - N1 - C2	113.37	113.15	-0.19
S1a - C1 - C2	115.52	111.59	-3.40
C1 - C2 - C3	115.79	114.18	-1.39
C1 - C2 - N1	110.23	112.13	1.72
N1 - C2 - C3	102.08	108.08	5.88
C2 - C3 - O1	112.56	117.11	4.04
C2 - C3 - O2	121.5	117.81	-3.04
O1 - C3 - O2	125.81	125.01	-0.64
Zn1a - S1b - Zn1b	92.47	100.73	8.93
Zn1a - S1c - Zn1b	61.51	59.08	-3.95

Appendix C

Point of Contact

For the source code for the Genetic Algorithm and the geometries of the structures discovered contact Dr. George Darling at darling@liv.ac.uk.

Bibliography

[1] Maddox, J. *Nature* **1988**, *335*, 201.

[2] Kirkpatrick, S.; Gelatt, C.; Vecchi, M. *Science* **1983**, *220*, 671–680.

[3] Metropolis, N.; Rosenbluth, A. W.; Rosenbluth, M. N.; Teller, A. H.; Teller, E. *J. Chem. Phys.* **1953**, *21*, 1087–1092.

[4] Wales, D. J.; Doye, Jonathan, P. *J. Phys. Chem. A* **1997**, *101*, 5111–5116.

[5] Laio, A.; Parrinello, M. *Proc. Natl. Acad. Sci.* **2002**, *99*, 12562.

[6] Goedecker, S. *J. Chem. Phys.* **2004**, *120*, 9911.

[7] Schönborn, S. E.; Goedecker, S.; Roy, S.; Oganov, A. R. *J. Chem. Phys.* **2009**, *130*, 144108.

[8] Pickard, C. J.; Needs, R. *Phys. Rev. Lett.* **2006**, *97*, 045504.

[9] Woodley, S. M.; Catlow, R. *Nature Materials* **2008**, *7*, 937–946.

[10] Phys489 lecture notes, university of liverpool. Hofer, W. **2007**.

[11] Hudson, A. D. *The interaction between small molecules and thermal surfaces* PhD thesis, University of Liverpool, **2007**.

[12] In the many body problem and density functional theory. http://www.newton.ex.ac.uk/research/qsystems/people/jenkins/mbody/mbody3.html. Jenkins, S.

[13] Hohenberg, P.; Kohn, W. *Phys. Rev.* **1964**, *136*.

[14] Kohn, W.; Sham, L. J. *Phys. Rev.* **1965**, *A140*.

[15] Electronic structure of matter - wave functions and density functionals. Kohn, W. **1999**.

[16] Martin, R. M. *Electronic Structure. Basic Theory and Practical Methods;* Cambridge University Press, first ed., 2004.

[17] Segall, M. D.; et al. *J. Phys. Condens. Matter* **2002**, *14*.

[18] Ceperley, D. M.; Alder, B. J. *Phys. Rev. Lett.* **1980**, *45*.

[19] Perdew, J. P.; Zunger, A. *Phys. Rev. B* **1981**, *23*.

[20] Perdew, J. P. *Phys. Rev. B* **1986**, *33*.

[21] Becke, A. D. *Phys. Rev. Lett.* **1988**, *38*.

[22] Perdew, J. P.; Chevary, J. A.; Vosko, S. H.; Jackson, K. A.; Pederson, M. R.; Singh, D. J.; Fiolhais, C. *Phys. Review B* **1992**, *46*, 6671.

[23] Perdew, J. P.; Burke, K.; Ernzerhof, M. *Phys. Rev. B* **1992**, *46*.

[24] Anisimov, V. I.; Aryasetiawan, F.; Lichtenstein, A. I. *J. Phys.: Condens. Matter* **1997**, *9*, 767–808.

[25] Anisimov, V. I.; Zaanen, J.; Andersen, O. K. *Phys. Rev. B* **1991**, *44*(3), 943–954.

[26] Sholl, D. S.; Steckel, J. A. *Density Functional Theory. A Practical Introduction;* John Wiley and Sons Inc., first ed., 2009.

[27] Marsman, M.; Paier, J.; Stroppa, A.; Kresse, G. J. *J. Phys.: Condens. Matter* **2008**, *20*, 064201.

[28] Paier, J.; Marsman, M.; Hummer, K.; Kresse, G.; Gerber, C.; Ángyán, J. G. *J. Chem. Phys.* **2006**, *124*, 154709.

[29] Muscat, J.; Wander, A.; Harrison, N. M. *Chem. Phys. Lett.* **2001**, *342*, 397.

[30] Paier, J.; Hirschl, R.; Marsman, M.; Kresse, G. *J. Chem. Phys.* **2005**, *122*, 234102.

[31] Heyd, J.; Scuseria, G. E.; Ernzerhof, M. *J. Chem. Phys.* **2003**, *118*, 8207.

[32] Heyd, J.; Scuseria, G. E.; Ernzerhof, M. *J. Chem. Phys.* **2006**, *124*, 219906.

[33] Kresse, G.; Hafner, J. *Phys. Rev. B* **1993**, *47*, 558.

[34] Kresse, G.; Hafner, J. *Phys. Rev. B* **1994**, *49*, 14251.

[35] Kresse, G.; FurthmÜller. *Comput. Mat. Sci.* **1996**, *6*, 15.

[36] Kresse, G.; FurthmÜller. *Phys. Rev. B.* **1996**, *54*, 11169.

[37] Monkhorst, H. J.; Pack, J. D. *Phys. Rev. B* **1976**, *13*.

[38] Allen, M.; Tildesley, D. *Computer simulation of liquids;* Oxford University Press, 1989.

[39] Cerius2 program notes, accelrys. **2003**.

[40] Hanson, R. M. Oct **2010**, *43*(5 Part 2), 1250–1260.

[41] Cardoso, C.; Borges, R.; Gasche, T.; Godinho, M. *J. Phys.: Condens Matter* **2008**, *20*, 035202.

[42] Matar, S.; Eyert, V.; Villesuzanne, A.; Whangbo, M.-H. *Physical Review B* **2007**, *76*, 054403.

[43] Lago, J.; Battle, P.; Rosseinsky, M. *J. Phys.: Condens Matter* **2000**, *12*, 2505–2524.

[44] Lago, J.; Battle, P.; Rosseinsky, M.; Coldea, A. I.; Singleton, J. *J. Phys.: Condens Matter* **2003**, *15*, 6817–6833.

[45] Mihut, A.; Spring, L.; Bewley, R.; Blundell, S.; Hayes, W.; Jestädt, T.; Lovett, B.; McDonald, R.; Pratt, F.L. Singleton, J.; Battle, P.; Lago, J.; Rosseinsky, M.; Vente, J. *J. Phys.: Condens Matter* **1998**, *10*, L727–L735.

[46] Battle, P.; Kasmir, J.; Millburn, J.; Rosseinsky, M. J.; Patel, R.; Spring, L.; Vente, J.; Blundell, S.; Hayes, W.; Klehe, A. K.; Mihut, A.; Singleton, J. *Journal of Applied Physics* **1998**, *83 (11)*, 6379.

[47] Battle, P. D.; et al. *J. Appl. Phys.* **1998**, *83(11)*.

[48] Yan, L.; et al. *Angew Chem Int Ed Engl* **2007**, *46(24)*.

[49] Freyria Fava, F.; D'Arco, P.; Orlando, R.; Dovesi, R. *J. Phys.: Condens. Matter* **1997**, *9*, 489–498.

[50] Husmann, A.; Blundell, S.; Jestädt, T.; Lovett, B.; Marshall, I.; Pratt, F.; Spring, L.; Battle, P.; Rosseinsky, M. *Physica B* **2000**, *289-290*, 69–72.

[51] Fawcett, I. D.; Sunstrom IV, J. E.; Greenblatt, M. *Chem. Mater.* **1998**, *10*, 3643–3651.

[52] Vanderbilt, D. *Physical Review B 41 (11)*, 7892.

[53] Yang, Z.; Ye, L. *J. Phys.: Condens. Matter* **2005**, *17*, 2035–2044.

[54] Matar, S. *Progress in Solid State Chemistry* **2003**, *31*, 239–299.

[55] Sze, S. M. *Semiconductor Devices: Physics and Technology;* Wiley: New York, second ed., 2001.

[56] Trindade, T.; O'Brien, P.; Pickett, N. L. *N. L. Chem. Mater.* **2001**, *13*, 3843–3858.

[57] van Poppel, L. H.; Groy, T. L.; Caudle, M. T. *Inorg.Chem.* **2004**, *43*, 3180.

[58] Sousa-Pedrares, A.; Romero, J.; Garcia-Vazquez, J. A.; Duran, M. L.; Casanova, I.; Sousa, A. *Dalton Trans.* **2003**, page 1379.

[59] Fleischer, H.; Dienes, Y.; Mathiasch, B.; Schmitt, V.; Schollmeyer, D. *Inorg. Chem.* **2005**, *44*, 8087.

[60] Eichhofer, A.; Buth, G. *Eur.J.Inorg.Chem.* **2005**, page 4160.

[61] Fu, A.-Y.; Wang, D.-Q.; Xing, J.-X. *Acta Crystallogr.,Sect.E:Struct.Rep.Online* **2005**, *61*, m2115.

[62] Cai, Z. X.; Yang, H.; Zhang, Y.; Yan, X. P. *Anal. Chim. Acta* **2006**, *559*, 234–239.

[63] Bharara, M. S.; Kim, C. H.; Parkin, S.; Atwood, D. A. *Polyhedron* **2005**, *24*, 865.

[64] Amo-Ochoa, P.; Rodriguez-Tapiador, M. I.; Castillo, O.; Olea, D.; Guijarro, A.; Alexandre, S. S.; Gomez-Herrero, J.; Zamora, F. *Inorg. Chem.* **2006**, *45*, 7642.

[65] Zhang, Q.; Bu, X.; Zhang, J.; Wu, T.; Feng, P. *J.Am.Chem.Soc.* **2007**, *129*, 8412.

[66] Dance, I. G. *J. Am. Chem. Soc.* **1980**, *102*, 3445.

[67] Muller, B.; Schneider, A.; Tesmer, M.; Vahrenkamp, H. *Inorg. Chem.* **1999**, *38*, 1900.

[68] Ingleson, M. J.; Bacsa, J.; Rosseinsky, M. J. *Chem. Commun.* **2007**, pages 3036–3038.

[69] Vaidhyanathan, R.; Bradshaw, D.; Rebilly, J. N.; Barrio, J. P.; Gould, J. A.; Berry, N. G.; Rosseinsky, M. J. *Angew. Chem., Int. Ed.* **2006**, *45*, 6495–6499.

[70] Anokhina, E. V.; Jacobson, A. J. *J. Am. Chem. Soc.* **2004**, *126*, 3044–3045.

[71] Anokhina, E. V.; Go, Y. B.; Lee, Y.; Vogt, T.; Jacobson, A. J. *J. Am. Chem. Soc.* **2006**, *128*, 9957–9962.

[72] Ingleson, M. J.; Perez Barrio, J.; Bacsa, J.; Dickinson, C.; Park, H.; Rosseinsky, M. J. *Chem. Commun.* **2008**, pages 1287–1289.

[73] Zhang, Y.; Saha, M. K.; Bernal, I. *Cryst. Eng. Commun.* **2003**, *5*, 34.

[74] Xie, Y.; Wu, H.-H.; Yong, G.-P.; Wang, Z.-Y.; Fan, R.; Li, R.-P.; Pan, G.-Q.; Tian, Y.-C.; Sheng, L.-S.; Pan, L.; Li, J. *J.Mol.Struct.* **2007**, *88*, 833.

[75] Kresse, G.; Furthmüller, J. Oct **1996**, *54*(16), 11169–11186.

[76] Housecroft, C. E.; Constable, E. C.

[77] Hursthouse, M. B.; Khan, O. F. Z.; Mazid, M.; Motevalli, M.; O'Brien, P. *Polyhedron* **1990**, *9*, 541–544.

[78] Lopez-Torres, E.; Mendiola, M. A. *Polyhedron* **2005**, *24*, 1435–1444.

[79] Müller, W.J.; Löffler, G. *Angew. Chem.* **1933**, *46*, 538–539.

[80] Stevenson, A. W.; Milanko, M. B. Z. *Acta Cystallogr., Sec. B: Struct. Sci.* **1984**, *40*, 521–530.

[81] James, S. L. *Chem. Soc. Rev* . **2003**, *32*, 276–288.

[82] Batlogg, B.; Jayaraman, A.; Van Cleve, J. E.; Maines, R. G. *Phys. Rev. B: Condens. Matter* **1983**, *27*, 3920–3923.

[83] Kazume, N.; Takuya, S.; Yuta, M.; Mamoru, B.; Masayuki, H.; Taizo, S. *Phys. Rev. B: Condens. Matter* **2006**, *74*, 035210.

[84] Owen, N. B.; Smith, P. L.; Martin, J. E.; Wright, A. J. *J. Phys. Chem. Solids* **1963**, *24*, 1519–1524.

[85] Huang, X.; Li, J. J. *J. Am. Chem. Soc.* **2007**, *129*, 3157–3162.

[86] Johnston, R. L. *Dalton Trans.* **2003**, pages 4193–4207.

[87] Roberts, C.; Johnston, R. L. *Phys. Chem. Chem. Phys.* **2001**, *3*, 5024–5034.

[88] Holland, J. H. *Adaptation in natural and artificial systems;* The University of Michigan Press, 1975.

[89] Hartke, B. *J. Phys. Chem.* **1993**, *97*, 9973–9976.

[90] Xiao, Y.; Williams, Donald, E. *Chemical Physics Letters* **1993**, *215*, 17.

[91] Bush, T.; Catlow, C.; Battle, P. *J. Mater. Chem.* **1995**, *5*, 1269–1272.

[92] Hartke, B. *Chemical Physics Letters* **1995**, *240*, 560–565.

[93] Zeiri, Y. *Physical Review E* **1995**, *51*, R2769.

[94] Deaven, D.; Ho, K. *Physical Review Letters* **1995**, *75*, 288.

[95] Michaelian, K. *Am. J. Phys.* **1998**, *66*, 231.

[96] Kabrede, H.; Hentschke, R. *J. Phys. Chem. B* **2002**, *106*, 10089–1095.

[97] Woodley, S. M.; Battle, P. D.; Gale, J. D.; Catlow, C. R. A. *Phys. Chem. Chem. Phys.* **1999**, *1*, 2535–2542.

[98] Abraham, N.; Probert, M. *Physical Review B* **2006**, *73*, 224104.

[99] Press, W. H.; Teukolsky, S. A.; Vetterling, W. T.; Flannery, B. P. *Numerical Recipes in Fortran - The Art of Scientific Computing*, Vol. Second Edition; Cambridge University Press, 1992.

[100] Ayuela, A.; López, J.; Alonso, J.; Luaña, V. *Z. Phys. D* **1993**, *26*, S 213–215.